On the Brownian dynamics of a particle in a bistable optical trap

Gabriel Schnoering

UNIVERSITÉ DE STRASBOURG

ÉCOLE DOCTORALE DE CHIMIE

UMR 7006

THÈSE présentée par :

[Gabriel SCHNOERING]

soutenue le : **22 Septembre 2016**

pour obtenir le grade de : **Docteur de l'université de Strasbourg**

Discipline/ Spécialité : Physique

On the Brownian dynamics of a particle in a bistable optical trap

Étude de la dynamique brownienne d'une particule dans un piège optique bistable

THÈSE dirigée par :

M. EBBESEN Thomas	Prof., ISIS, Université de Strasbourg

RAPPORTEURS :

M. KÄLL Mikael	Prof., Chalmers University of Technology
M. QUIDANT Romain	Prof., The Institute of Photonic Sciences (ICFO)

PRÉSIDENT DU JURY :

M. HERVIEUX Paul-Antoine	Prof., IPCMS, Université de Strasbourg

INVITÉ :

M. GENET Cyriaque	Dr., ISIS, CNRS

1) Introduction

Depuis leur développement il y a 30 ans, les pinces optiques et les pièges optiques sont devenus des outils incontournables pour manipuler de manière non-invasive des objets à l'échelle nanométrique. Ces outils ont donc essaimé dans un grand nombre de disciplines, allant de la physique fondamentale à la biologie en passant par la chimie. En biologie en particulier, les pinces optiques ont été cruciales pour mesurer les forces moléculaires, les propriétés mécaniques de l'ADN, caractériser les dynamiques de moteurs moléculaires spécifiques, etc [1].

De nombreuses configurations expérimentales de pièges optiques ont été développées. La grande variété de systèmes a permis d'atteindre un contrôle extrêmement efficacement de l'objet piégé et les systèmes de détection en position associés ont atteint des niveaux de résolution exceptionnels. A l'heure actuelle, un nouveau domaine d'étude a émergé, exploitant au maximum la maîtrise que ces outils optiques uniques permettent d'atteindre. Ce domaine consiste à utiliser les objets micro- ou nanométriques piégés optiquement comme sondes locales de processus stochastiques spécifiques pour tester un certain nombre de prédictions dans le domaine de la thermodynamique physique statistique hors-équilibre [2]. De nombreuses expériences ont ainsi été réalisées avec des résultats très importants rendus possibles par la capacité de mesurer la position instantanée et microscopique de l'objet piégé. Avec ces outils, un grand nombres de théorèmes de la thermodynamique ont été vérifiés et un grand nombres d'inégalités (telles de Crookes, Jarzynski, etc) ont pu être étudiées avec une résolution jamais atteinte. Un point en particulier qui a retenu l'attention de la communauté récemment est la possibilité offerte dans une configuration de piège optique de mesurer exactement les échanges de chaleur et de travail réalisés par l'objet piégé dans un grand ensemble de potentiels dynamiques. Un cas particulier de tels potentiels est le cas des potentiels dits bistables qui comprennent de potentiels attractifs séparés par une barrière. La bille partage donc son temps entre deux positions spatiales métastables [3].

2) Résultats et discussion

Les travaux présentés dans cette thèse explorent différentes propriétés dynamiques de l'objet piégé dans de tels potentiels. Ces potentiels sont réalisés à l'aide d'un piston optique.

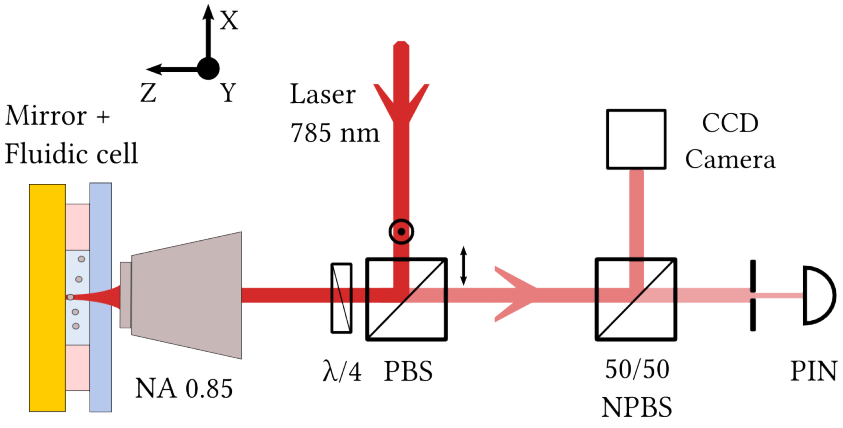

Fig. 1 Schéma du montage expérimental. Le laser à 785 nm est focalisé sur un miroir au travers d'une cellule fluidique, piégeant en son col une bille diélectrique de diamètre typique 1 micron. La diffusion vers l'avant du laser sur la bille, réfléchie sur le miroir, est renvoyée sur une

photodiode rapide (PIN) ou une caméra CCD pour reconstruction de la trajectoire de la bille piégée.

Un tel piston consiste en une pince optique proche d'une surface réfléchissante dont l'onde incidente et réfléchie vont interférer permettant de sélectionner le type de potentiel dans lequel un objet va évoluer – Fig. 1. Un changement dans la position du miroir va permettre d'altérer continûment les propriétés du potentiel d'interaction. Il sera montré comment le type de régime dynamique de l'objet évolue à travers le contrôle précis de cette variable externe. Une transformation continue du potentiel d'interaction est également associée à des transitions dynamiques dont les propriétés thermodynamiques sont déterminées et mesurée avec une grande précision relative à l'énergie de la fluctuation thermique. Finalement le contrôle du potentiel optique offre par l'ajout d'un faisceau supplémentaire la possibilité d'étudier les différents régimes dynamiques de l'objet dans un potentiel bistable en régime de forçage.

Dans une première partie du travail, les systèmes hors équilibre stationnaires sont présentés dans leur généralité puis le cas de la bistabilité est discuté plus en détail ainsi que le problème directement lié dit de Kramers [4]. Une introduction sera également donnée sur différents potentiels optiques non linéaire et la dynamique de particule brownienne piégée qui y est associée, en tenant compte en particulier du fait que la particule piégée agit comme une sonde locale cartographiant dans l'espace et le temps au cours de sa diffusion le potentiel de piégeage. Un rapide résumé de protocoles thermodynamiques intéressants ayant été réalisé ces dernières années est présenté et le régime mécanique dans lequel les expériences sont réalisées dans cette thèse est spécifié en détail. Nous insistons en particulier sur le caractère sur-amorti du régime dynamique de nos expériences.

Le deuxième chapitre présente le piston optique en tant que tel. Ce piston optique est réalisé à partir d'une onde stationnaire formée par un faisceau incident et sa réflexion sur un miroir – voir Fig. 2. Les spécificités de cette configuration par rapport aux pinces optiques conventionnelles sont discutées en détail et illustrées par quelques exemples. Après avoir décrit le montage expérimental lui-même, la structure du champ et de l'onde stationnaire sont définis afin de pouvoir mesurer la dynamique, à une dimension, de l'objet piégé suivant l'axe optique. Le potentiel dans lequel la bille évolue est formé par l'interaction entre le champ optique et la réponse diélectrique de la nano sphère. La modulation de la position du miroir permet la construction d'interférences constructives ou destructives par rapport au col (waist) du faisceau gaussien focalisé et offre un piège stable pour la bille à cet endroit (interférence constructive) ou instable (interférence destructive). Dans ce dernier cas, la bille sera piégée devant ou derrière le col et pour une intensité de laser bien choisie elle partagera dynamiquement son temps entre ces positions moyennes. Sur une telle séparation des temps, il est possible d'observer une dynamique de la bille réellement bistable. Par la mesure des temps de résidence dans ce potentiel bistable ainsi que les propriétés locales de confinement de la bille, le problème de Kramers est alors parfaitement spécifié et permet de décrire quantitativement la dynamique associée à de tels processus bistables stationnaires. Il nous permet de déterminer entièrement le potentiel d'interaction de la bille. La figure 3 montre l'enregistrement typique du signal de saut de la bille entre les 2 minima locaux de piégeage.

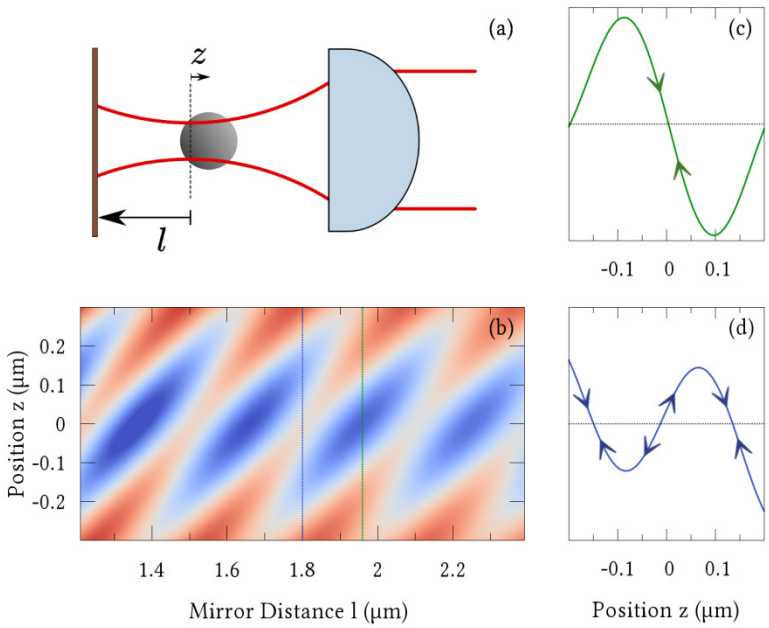

Fig. 2 : (a) Schéma du piston optique. La bille (rayon R=500 nm) est piégée par un faisceau Gaussien focalisé au travers de l'objectif de microscope. Le miroir positionné au voisinage du col du faisceau détermine l'évolution cohérente du potentiel optique (b). En fonction de la distance entre le miroir et l'objectif, le potentiel optique correspond à un piège harmonique (c) ou un piège bistable (d).

Le troisième chapitre utilise ce contrôle sur les différents potentiels optiques afin d'étudier la transition dynamique de la bille d'un potentiel stable, quasi harmonique vers un potentiel bistable. Pour ce faire, la position du miroir du piston est changée pas à pas, laissant la bille relaxer dans sa position d'équilibre dans chacune de ces nouvelles configurations. Exploitant la méthode de résolution de potentiel du chapitre précédent, il est alors possible de déterminer la trajectoire de configuration lorsque l'objet piégé traverse une région de bistabilité. La mesure de cette transition réversible permet la détermination des quantités thermodynamiques qui y sont associées, à savoir le travail et la chaleur.

Le quatrième chapitre exploite la capacité à placer la bille dans une dynamique bistable pour appliquer sur le système bistable une force extérieure de fréquence et amplitude donnée afin d'étudier le degré de synchronisation, c'est a dire la capacité mécanique de la bille à suivre la perturbation extérieure [5]. Dans l'étude usuelle de la dynamique de systèmes mécaniques en régime de forçage, la force extérieure prend une forme sinusoïdale, ce qui implique d'appliquer une force parfois positive ou négative sur le système. Expérimentalement une telle dynamique est délicate à réaliser vu la configuration de montage utilisée, c'est pourquoi le système est placé dans une configuration telle que le potentiel de piégeage, sur lequel est superposée une force extérieure constante de pression de radiation, induit une dynamique bistable symétrique. Comme le potentiel formé par le laser de piégeage est dans une enveloppe quasi harmonique, une diminution de la pression de radiation par le second faisceau est équivalente à l'application d'une force négative sur le système. Après obtention d'une dynamique bistable avec les deux faisceaux, le second laser de poussée est modulé autour de sa valeur constante de pression de radiation et la dynamique de synchronisation induite est étudiée. Une telle configuration permet d'étudier les régimes de faible perturbation extérieur (une trop forte perturbation pousse la bille hors du piège et la force de pression

constante ne doit pas être trop grande pour rester "linéaire" dans le potentiel de piège). Les forces appliquées sur la bille piégée sont mesurées en plaçant la bille dans un potentiel quasi harmonique puis déterminés via le déplacement de la bille. La seconde partie du chapitre explore également les régimes de synchronisation, mais cette fois à travers la modulation dynamique de la position du miroir. Ce régime permet de changer continûment le potentiel d'interaction de la bille et donc de passer d'un potentiel bistable symétrique a un potentiel très fortement asymétrique. Une telle approche permet d'atteindre des régimes de forçage fort, c'est à dire des régimes ou l'amplitude de la force externe est grande. En effet une très grande perturbation du potentiel, donc de la position du miroir, pousse la bille dans le potentiel stable le plus proche. Dans une telle configuration la dynamique de la bille est mesurée à travers la diffusion vers l'avant d'un faisceau sonde de faible intensité envoyée sur la bille et dont la transmission est collectée sur une photodiode à quadrants.

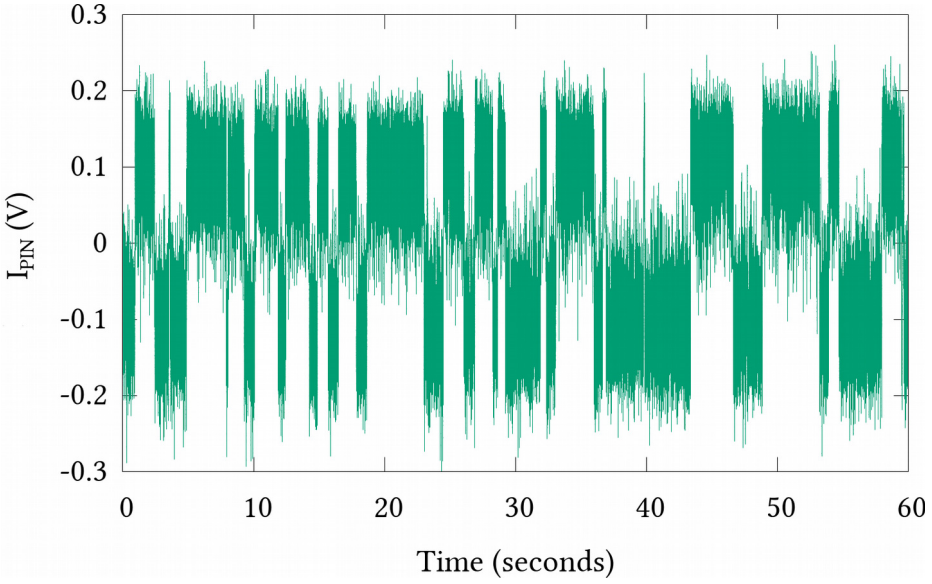

Fig. 3 : Trace temporelle associée à la dynamique bistable de la bille piégée, telle qu'elle est acquise par la photodiode rapide de la figure 1. Le temps d'acquisition est de 60s, à une fréquence d'échantillonnage de 262 kHz.

Dans le cinquième et dernier chapitre, les futurs développements du montage optique actuel sont présentés ainsi qu'un ensemble de perspectives de recherche. Tout d'abord la résolution minimale pour la détection d'une force externe par pression de radiation est discutée [6]. Afin de réaliser ces mesures, une nano-sphère d'or de diamètre 150 nm est piégée. Le piégeage d'une nanoparticule métallique de petit diamètre présente des difficultés pour garantir la présence d'un objet unique dans le piège et non un agrégat où de multiples particules. Pour discriminer ces différentes possibilités un système d'imagerie interférométrique à été ajouté sur le montage. Via l'imagerie, l'approche des objets avant d'entrer dans le piège peut être suivi en temps réel. En suivant également l'intensité de contraste du motif d'interférence de l'objet piégée, sa nature peut être résolue en déterminant la présence d'agrégats où de multiples particules. Pour une nanoparticule unique piégée, une force la pression de radiation est appliqué sur l'objet par un second laser et cette force est mesurée à travers le déplacement de la bille dans le piège. L'objectif de cette mesure est de déterminer la plus petite force mesurable à une fréquence donnée à travers le déplacement de l'objet piégée. Pour ce faire un système d'amplification par verrouillage de phase est utilisé pour extraire la modulation périodique de déplacement de la bille piégée

du mouvement de diffusion brownien. Cette configuration expérimentale présente une très bonne résolution dans la mesure de forces faibles sur l'objet piégé. Ce montage optique et ce système de détection de forces faibles sont ensuite exploités dans le cadre de la mesure de forces optiques chirales. L'expérience ici consiste à piéger un objet chiral devant un miroir dichroïque, d'injecter dans le piève un deuxième faisceau de longueur d'onde résonante avec le dichroïsme circulaire de l'objet chiral piégé. La polarisation de ce second faisceau est ensuite périodiquement modulée. Une étude théorique faite au laboratoire montre que la chiralité de l'objet se couple avec la chiralité du champ optique pour faire émerger une composante de force ne dépendant que du couplage chiral entre l'objet et la particule chirale. Suivant la chiralité du champ le signe de la force s'inverse. Finalement des perspectives plus techniques d'amélioration du montage expérimental sont présentés, en particulier l'amélioration de la détection par imagerie interférométrique ainsi que la méthode de modulation utilisée pour la mesure des forces chirales, en particulier par l'introduction d'un modulateur photoélectrique.

3) Conclusion

Cette thèse présente une nouvelle configuration de piégeage optique qui permet la mise en œuvre d'un grand nombre de protocoles physiques. Le haut degré de contrôle du piston optique décrit dans ce travail permet en effet de couvrir expérimentalement des situations relevant aussi bien des systèmes hors-équilibres stationnaires (chapitres sur la bistabilité opto-mécanique et sur la synchronisation) que des problématiques des machines de force à haute résolution (chapitre 5). Ce travail fait la démonstration de l'intérêt de la configuration, en démontrant notamment une résolution de mesures de forces de pression de radiation optiques sans précédent. Si les résultats sur les forces chirales optiques ne sont pas encore au niveau du contrôle nécessaire pour détecter les forces au niveau de nanoparticules chirales uniques, les données obtenues à ce jour permettent à l'issue de ce travail d'identifier clairement les marges de progression disponibles. C'est dans ce contexte de la chiralité optique que ce travail se conclut et qu'il ouvre des perspectives uniques qui seront évidemment au centre des expériences futures qui seront menées au laboratoire sur ce système de piston optique.

4) Références

[1] D. Grier, Nature **424**, 810 (2003)
[2] U. Seifert, Rep. Prog. Phys. **75**, 126001 (2012)
[3] A. Berut, A. Arakelyan, A. Petrosyan, S. Ciliberto, R. Dillenschneider, and E. Lutz, Nature **483**, 187 (2012)
[4] L.I. McCann, M. Dykman, and B. Golding, Nature **402**, 785 (1999)
[5] A. Simon and A. Libchaber, Phys. Rev. Lett**. 68**, 3375 (1992)
[6] L. Liu, S. Kheifets, V. Ginis, and F. Capasso, Phys. Rev. Lett. **116**, 228001 (2016)

Liste des présentation et des conférences :

Les Houches, Août 2013 – Ecole d'été : Optique quantique et nanophotonique + Poster : Optical Tweezing Above a Mirror, Gabriel Schnoering, Cyriaque Genet and Thomas Ebbesen

Nanoplasmonics: Faraday Discussion 178, 16 - 18 February 2015, London, United Kingdom + Poster : Inducing dynamical bistability by reversible compression of an optical piston, Gabriel Schnoering, Cyriaque Genet and Thomas Ebbesen

Nanolight 2016, Mar 06 -- Mar 12, Benasque + Poster : Inducing dynamical bistability by reversible compression of an optical piston, Gabriel Schnoering, Cyriaque Genet and Thomas Ebbesen

Liste des publications :

Gabriel Schnoering and Cyriaque Genet, "Inducing dynamical bistability by reversible compression of an optical piston", Phys. Rev. E **91**, 042135

R. O. Behunin, D. A. R. Dalvit, R. S. Decca, C. Genet, I. W. Jung, A. Lambrecht, A. Liscio, D. López, S. Reynaud, G. Schnoering, G. Voisin, and Y. Zeng, "Kelvin probe force microscopy of metallic surfaces used in Casimir force measurements", Phys. Rev. A **90**, 062115

G. Schnoering, H. Wendehenne, A. Canaguier-Durand, C. Genet "Measuring weak radiation pressure forces below the brownian diffusion noise level" – **en prépartion**

CONTENTS

INTRODUCTION

Since its first developments [1, 2], optical trapping has impacted many different fields of research, with new applications covering a broad range of topics. For instance, optical traps have become invaluable tools for measuring biophysical and biochemical processes with unprecedented resolution [3] or DNA manipulation [4]. The demonstration of genuine molecular motors has been achieved in optical trapping configurations [5].

Optically trapped Brownian particles constitute ideal test systems for non-equilibrium statistical physics with a great variety of stochastic protocols under external force fields that can be implemented [6]. A particular attention has been devoted to measuring thermal fluctuation-induced escape over an optical potential barrier and exploring Kramers rate theory, including the observation of stochastic synchronization [7–10]. More recently, quantitative tests of so-called fluctuation theorems have involved optically trapped nanoparticles, both in the over- and under-damped regimes [11–14]. Bistable optical potentials are currently exploited for developing Szilard-types engines and studying the connections between information theory and thermodynamics [15–17].

These results rely on the capacity of optical traps to work as reliable and precise force transducers. Central to this is the possibility to reduce the trap stiffness (simply by decreasing the trapping laser intensity) to low values, gaining a versatility that cannot be be reached with atomic force microscopes where the cantilever stiffness is fixed for a given configuration. In this context, a whole body of work have emphasized the unique capacity of optical tweezers to perform high-resolution force spectroscopy, in particular in the context of colloidal physics [18–20] and more recently in the context of Casimir physics [21].

In this thesis, we have studied the Brownian dynamics of a particle, optically trapped in a bistable potential. The bistability, induced optically and therefore precisely controllable, is the source of various dynamical properties that we have explored in details. The work has been structured in 5 different chapters.

- The first chapter aims at summarizing, very briefly, some important elements that are central to optical trapping, from the basic description of forces involved, to the important tool of power spectral density analysis. Such a spectral-based approach emphasizes the fluctuating essence of the dynamics of the particle, and solving the Langevin equation associated with the optical interaction potential yields all the relevant experimental quantities to measure. Trapping micro- and nano-particles has rapidly nourished a broad range of research topics. This first chapter tries to illustrate as efficiently as possible one aspect of the landscape of recent studies that are unveiling the rich thermodynamics that emerges from manipulating single Brownian objects in tailored optical environments.

- The second chapter describes the realization of one-dimensional bistable potentials by means of an optical piston. Our piston consists in an optical tweezer placed in front of a reflecting movable mirror, inducing a standing wave pattern. Shifting the position of the mirror allows shaping different dynamical regimes, from stable to metastable regimes continuously. A one micrometer dielectric bead is trapped within such a standing wave field. The knowledge of the optical profile of the trapping beam permits, for bistable dynamics, to fully resolve the interaction potential thermally explored by the bead. In such regimes, the dynamics of the bead is well described by Kramers rate equation which we fully solve. The stationarity of our potential configurations is experimentally verified and we close this chapter by drawing phase space-like representations of the metastable dynamics, that can be drawn despite the fact the diffusive character of the motion of the bead.

- In the third chapter, the piston length is now incrementally compressed, causing a progressive deformation of the interaction potential. The bead is let to relax in each different potential configurations. A reversible cross-over is performed from two stable trapping regions separated by a whole region of bistability. Potentials are entirely determined throughout the compression by exploiting the method of the second chapter. Over the course of a complete cross-over, the bead comes back to its initial spatial position but its potential energy has

changed. This leads us to study the thermodynamic distribution of the work injected by the piston. We show how this work is mainly consumed as a potential energy change, with some production of heat generated by the optical deformation of the potential while the bead is relaxing to new configurations along the compression.

- The fourth chapter studies the continuous compression and decompression of the piston around a bistable configuration. A periodic modulation of the position of the mirror corresponds to an external harmonic forcing of the bistable dynamics of the trapped bead. This leads to stochastic resonance-like phenomena that we study by characterizing the stochastic resonance via the synchronization of the bead stochastic trajectory with the external modulation. This is done experimentally but also through numerical realizations of the bead dynamics (using a discrete Langevin equation formulation). We introduce Mandel factors in order to interpret the evolution of the distribution of residency times in each of the bistable states. With an external sinusoidal drive, three main types of dynamical responses are identified in simulations and experiments. A regime of rectified bistability at low frequency, while at high frequencies the drive becomes transparent to the motion of the bead. For frequencies matching the non-driven thermal activation frequency, the regime of synchronization is observed. We deepen our analysis with a time delay approach, which provides the evolution of the probability distributions associated with the hopping events with respect to the drive and yields remarkable signatures.

- As examples of the versatility of the optical piston, the fifth chapter presents (i) the trapping of gold nano-spheres, including a description of a real time interferometric imaging scheme, (ii) an experiment measuring weak optical forces with a sub-fN level of resolution based on a lock-in detection method, and (iii) the trapping and polarization-based recognition of single chiral nano-enantiomers, demonstrating that the optical piston offers interesting possibilities when dealing with more exotic optically trapped nano-objects, such as chiral nanopyramids.

1

IMPLEMENTING DYNAMIC PROCESSES WITH OPTICALLY TRAPPED BROWNIAN PARTICLES

While optical tweezing was growing as a powerful noninvasive tool in particular in the fields of biology and physics, it was realized that optical tweezers also leads to the possibility to shape the optical trapping landscapes in such ways as to implement specific interaction potentials within which the trapped Brownian particle will evolve. One of the early demonstration of the relevance of this approach was done in the context of Kramers dynamics [7].

Recently, a whole field of research has emerged where optical tweezers give the possibility to implement experimentally a great number of dynamic processes with tailored optical potentials, usually of the double-well types (as in [7, 8, 22]).

Obviously, monitoring in real time the motional trajectories of Brownian particles coupled to a thermal bath has given new experimental opportunities in the context of stochastic thermodynamics. Here, microscopic nanoparticles which motion and position noise can be controlled optically, and at the level of which random forces (external vs. internal) can be carefully tuned, constitute new probes for studying fundamental issues, among which the connection between statistical physics and information theory has attracted much attention [16].

Following these trends, we propose in this thesis a new configuration for controlling the optical interaction potential of an overdamped Brownian particle: the optical piston (Ch.2). This thesis has focused on the concept of dynamic bistability, in close relation with the so-called Kramers' problem [23, 24]. A central point of the thesis is to discuss the situation where some work is injected on the particle by an external drive, and to analyze different processes depending on whether they are performed quasi-statically (stable vs. bistable crossover -Ch.3) or in a time-dependent way (stochastic resonance -Ch.4).

Naturally in the context of optically trapped systems, optical forces are simple actuators that can easily play the role of the external source of driving. This is precisely where the thesis makes the connection with the topic of optical force spectroscopy and gives us the opportunity to focus more precisely on the problem of detecting weak external optical forces and measuring them with the highest resolution level available (Ch.5), given the limits imposed by the over-damped motion of the bead in the fluid.

1.1 OPTICAL FORCES

The basis of optical trapping can be simply understood by looking at the nature of the optical forces exerted on an electric dipole (Rayleigh regime) by an electromagnetic field [25]. We consider an electric dipole $\mathcal{P}$ (Rayleigh particle) in a homogenous medium of refractive index $n(\omega)$, assuming monochromatic electromagnetic fields $\mathcal{E}$ and $\mathcal{H}$ of angular frequency ω. The force excerted on the object by the general real electric field $\mathcal{E}$ and the magnetic field $\mathcal{H}$ field is given by the Lorentz law,

$$\mathbf{F} = (\mathcal{P} \cdot \nabla)\,\mathcal{E} + \mu_0 \dot{\mathcal{P}} \times \mathcal{H}. \tag{1.1}$$

The electric dipole $\mathcal{P}$ is related to the electric field through its complexe polarizability $\alpha(\omega)$.

Applying eq. (1.1) to our dipole leads to the time averaged force excerted on the object. This force is decomposed in two components, the reactive force $\mathbf{F}_{\text{reactive}}$ associated with the intensity gradient of the field,

$$\mathbf{F}_{\text{reactive}} = \frac{n^2}{4}\,\text{Re}[\alpha]\nabla\left(\|\mathcal{E}\|^2\right), \tag{1.2}$$

The second costribution is the dissipative force $\mathbf{F}_{\text{dissipative}}$ which provides the radiation pressure component of the force,

$$\mathbf{F}_{\text{dissipative}} = n^2\omega\mu_0\,\text{Im}[\alpha]\left(\Pi - \frac{\nabla \times \Phi_E^2}{2\omega\mu_0}\right), \tag{1.3}$$

with $\Pi = \langle \mathcal{E} \times \mathcal{H} \rangle_T$ the time-averaged Poynting vector, $\Phi_E = \mathcal{E} \times \dot{\mathcal{E}}/\omega$ the time-independent electric polarization ellipticity and μ_0 the vacuum permeability.

While the dipole is pushed by a radiation pressure term, the presence of a field gradient leads to localize the dipole in regions where the field is high. In this regime, trapping is achieved when the gradient is strong enough as to win over the destabilizing radiation pressure, in particular along the optical axis.

1.2 OPTICAL TRAPPING IN THE MIE REGIME

This simple picture drawn in the Rayleigh regime remains valid in the Mie regime, although the physical interpretation is not as straightforward. Ashkin, when proposing the idea of optical trapping, developed an elegant and very efficient approach to the physics of optical tweezers, based on a refraction-based momentum exchange argument [2].

In his description, Ashkin calculated the resulting force from an optical ray construction done at the level of a spherical object of refractive index *larger* than the surrounding medium exposed to an incident Gaussian TEM_{00} intensity profile. In such conditions, the force is decomposed in orthogonal gradient and scattering contributions. This decomposition is shown on Fig. 1.1 with the gradient force F_{grad} perpendicular to the beam propagation and the scattering force F_{scat} acting along the optical axis. In the case of a highly focused Gaussian beam, i.e. through a high NA objective, the resulting forces point towards an equilibrium position nearby the waist of the beam.

When the forces applied on the object are stronger than the thermal fluctuation and the scattering contribution points towards the waist because of the tight focusing of the beam the object is held by a single focused laser beam.

1.3 STANDING WAVE OPTICAL TRAPS

One way to favor gradient forces over scattering contributions is simply to compensate the latter as much as possible. This can be done using counter propagating beams, as proposed by Ashkin [26]. In such a configuration, the dielectric bead is trapped at the position where the two scattering force contribution balance. Stable trapping is then achieved if, as always, the gradient force is strong enough to win over thermal fluctuations. This scheme is also applicable to trap large dielectric objects, although remaining challenging to align and exploit [27–29].

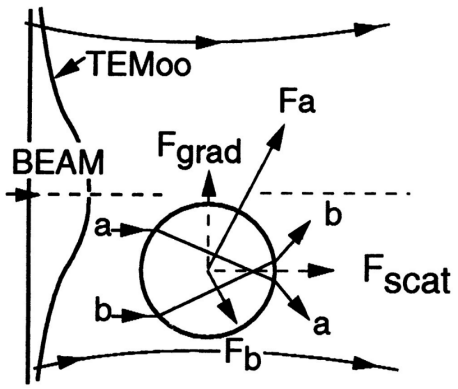

Figure 1.1: Diagram showing the ray optics interpretation of the optical trapping of a transparent spherical particle. The high index sphere is immersed in a lower index medium. The gradient F_{grad} and scattering F_{scat} forces emerge form differences in refraction angles when illuminated by a TEM_{00} Gaussian beam. This illustration is directly taken from [26].

An alternative idea, proposed and extensively studied by Zemanek in 1998 is to form this counter propagating configuration by a mere reflection of the Gaussian laser beam incident on a mirror [30, 31]. The incident laser beam is focused in the vicinity of the reflective surface and even when not exactly focused on the mirror, the axial contributions of the scattering force are partially compensated, but sufficiently well to enable the trapping of a single particle. In such a configuration, optical trapping becomes much easier and achievable with lower numerical apertures.

This configuration is exploited throughout this thesis. The principal reason for its use is its versatility. It can be adapted to trapping objects with various numerical apertures, objects of different sizes and even of different materials. The presence of the mirror renders the precise alignment easy to achieve via the beam reflection (autocollimation procedure of the incident beam). This trapping scheme also allows working with different types of mirror (as illustrated in this thesis) and at different distances from them. It allows measuring forces induced by the presence of the mirror: either from drag contributions [32, 33] or when complex field landscape are created [34]. The standing wave nature of the trap can yield various stable trapping positions around the beam waist. With trapped object that can be larger than the distance between two interference

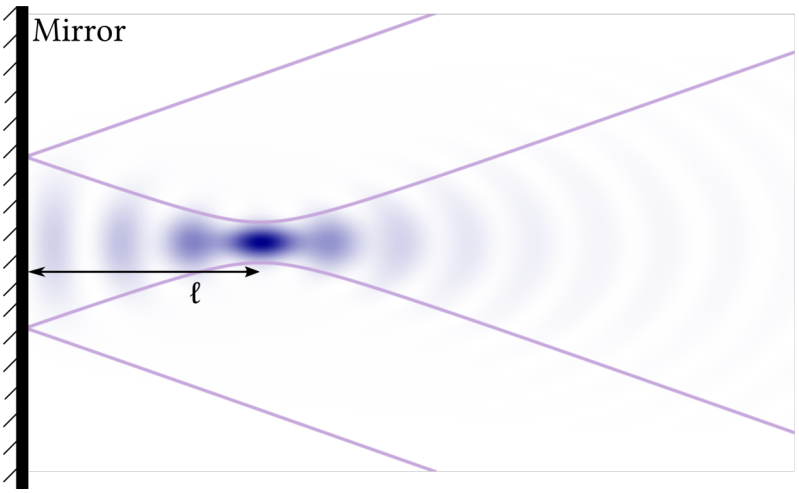

Figure 1.2: Diagram showing the field intensity (in blue) of a Gaussian beam focused at a distance ℓ behind the mirror (a few µm). The beam has a numerical aperture of 0.85 and a wavelength of 785 nm. Continuous purple lines illustrated the beam envelope.

fringes, specific averaging effects occur on the trapping volume, with possible modifications of the stable position, depending on the object size [35].

The node vs. anti-node structure of the intensity profile along the optical axis also gives the ability to trap metallic nano-spheres. Recently, extensive work has been devoted to the trapping gold nano-objects [36]. It was experimentally demonstrated that trapping gold nano-objects poses no issues in the Rayleigh regime (object sizes below 60 nm), the object size being an order of magnitude smaller than the trapping wavelength [37, 38].

Trapping of larger Au spheres is more difficult. Stable trapping of Au sphere of sizes up to 250 nm using a single beam tweezer has been demonstrated [39–41]. These results have however been debated with recent theoretical claims stressing that trapping such large spheres is not feasible using conventional single beam optical tweezer [42, 43] and that the source of stable trapping must stem from the asymmetric (polyhedral, e.g.) shapes of real particles, just as Au nano-rods align in the optical trapping field [44].

In this context of trapping metallic objets, other interesting approaches have been proposed, for instance trapping metallic particles against a plane, leaving in-plane motions

free for large objects (radius of 200 nm) [45, 46] and with the possibility to trap objects of different shapes [47].

A capacity to trap Au nanoparticles will turn central in the thesis. We will therefore exploit this appealing feature of the standing wave trap configuration. In such a configuration, we have been able to trap Au nanospheres of sizes up to 150 nm. Interestingly, we have never been able to trap the same Au nanospheres in a conventional optical trap (single beam), even using high NA immersion objective. he trapping of the same objects with high NA objectives proved impossible in a conventional optical configuration (by removing the mirror).

Trapping Au nanosphere is only possible in the standing wave configuration because the sphere is not trapped at a maximum of intensity but rather at a minimum, i.e. on a node of the standing wave pattern. The two anti-nodes surrounding the node in the intensity distribution will thus form a kind of cage for the nanosphere. The lateral confinement, from which the stability of the trap will derive, stems from the attractive gradient contribution in the force. Both forces combined provide a force field around the waist that offers a single stable position between the two intensity maxima surrounding the waist.

1.4 LANGEVIN DYNAMICS

The dynamics of a single objects trapped in an attractive potential $U(z)$ created by the focusing of a laser beam in a thermalized medium is well described by the equation of motion of the center-of-mass of the object. This was first proposed by Langevin [48] and provided one of the first "intuitive" understanding of the seemingly erratic motion of small object in hot bath. In his work, Langevin modeled the bath contribution to the motion as an uncorrelated (and scaled) Gaussian distributed noise.

In this view, the complete equation of motion writes as:

$$m_B \frac{d^2z}{dt^2} + \gamma \frac{dz}{dt} - \nabla U(z) = F(T, z, t), \tag{1.4}$$

with m_B the mass of the bead in kg, γ the drag coefficient in $Ns/m = kg\,s^{-1}$, $-\nabla U(z)$ the force deriving from the potential gradient in N. Assuming that the motion of the bead remains localized on the optical axis of the focused Gaussian beam, the interaction potential is linearized to a harmonic shape and the

force becomes a linear restoring force $-\nabla U(z) = \kappa_T \cdot z$ of stiffness κ_T expressed in N/m.

The noise contribution, given by the fluctuation-dissipation theorem [49] is in the case of a 1D motion of the object $F(T,z,t) \simeq \sqrt{2k_bT\gamma} \cdot \eta(t)$. We assume the bath as homogeneous (with a constant drag coefficient) and the observed dynamical range long with respect to molecular collision characteristic times. On average, these collisional contributions on the larger trapped object cancel and the bath contribution is considered uncorrelated in time with $\langle \eta(t)\eta(t') \rangle_{time} = \delta(t-t')$.

Considering the sizes and masses of our trapped objects, the timescale associated with inertial motion dynamics $\frac{m_B}{\gamma}$ is around 10^{-7}s, way faster than what our acquisition setup can monitor. For simplicity in the notations, the inertial term is then neglected, the dynamical regime used throughout all of the presented experiments stays over-damped and simply writes

The inertial term can be kept when solving the equation of motion both temporally and in frequency but their contribution becomes negligible with respect to others.

$$\gamma \frac{dz}{dt} + \kappa_T z = F(T,z,t). \tag{1.5}$$

1.4.1 *Spectral analysis*

Spectral analysis of such dynamics offers the advantage that the dynamical parameters of the trapped bead are determined similarly to doing a direct time correlation analysis but without the computational burden associated. The important requirement though is to have a recorded signal stationary and we note that this property is often met in most cases.

Computing the correlation function of a few millions sample acquisitions counts in hours. The spectral counterpart is seconds.

With this assumption valid, we use the usual Fourier transform definitions, with

$$g[f] = \int_{-\infty}^{+\infty} g(t)\, e^{-2i\pi ft}\, dt \tag{1.6}$$

and its inverse transform as

$$g(t) = \int_{-\infty}^{+\infty} g[f]\, e^{2i\pi ft}\, df. \tag{1.7}$$

Fourier transformed, the over-damped equation of motion $z[f]$ -Eq. (1.5)- writes as the mechanical susceptibility of the system times the drive source $F[f]$,

$$z[f] = F[f]\, \frac{1}{(\kappa_T + 2i\pi\gamma f)}. \tag{1.8}$$

The bath force term $F[f] = \sqrt{2\gamma k_b T} \cdot \eta[f]$ which is uncorrelated in time has a flat spectral signature because $|\hat{\eta}(f)\overline{\eta[f]}|^2 = 1$. This family of noise sources is called *white* because all frequencies excite the system with the same intensity.

The power spectrum is obtained by taking the modulus squared of the Fourier transform $S_z[f] = |z[f]\overline{z[f]}|^2$ and writes as a Lorentzian with:

We consider here the twosided spectral density.

$$S_z[f] = \frac{D}{2\pi^2} \frac{1}{(f_T^2 + f^2)}, \tag{1.9}$$

with $D = \frac{k_b T}{\gamma}$ the diffusion coefficient in $m^2\ s^{-1}$ and $f_T = \frac{\kappa_T}{2\pi\gamma}$ the roll-off frequency of the trap in Hz. In the context of spherical objects, the Stokes drag expression is used for spherical beads of radius R, $\gamma = 6\pi\rho\nu R$ in $kg\,s^{-1}$ with ρ the density of the fluid (in kg/m^3) and ν the kinematic viscosity (in $m^2\,s^{-1}$).

Numerically the power spectral density is normalized to be independent of both the length of the signal (number of samples) and the sampling rate.

The Lorentzian spectral signature of the trapped object is decomposed in two parts, below the roll-off frequency, the bead is confined and held by the laser beam, all frequencies have equal strength. Above the roll-off frequency, the spectral signature is $1/f^2$, the one of a freely diffusing (non-trapped) Brownian object.

1.5 SOME EXAMPLES OF PROCESSES

The point of view of considering the optically trapped particle as a Brownian probe for a wide range of processes perfectly fits within the framework of the Langevin equation. As we will discuss later in the manuscript, a whole field of research, namely stochastic energetics [50] has recognized in the Langevin formulation an extremely rich methodological approach towards stochastic thermodynamics.

Through the Langevin dynamics therefore, one understand how optically trapped Brownian particles have become privileged systems to probe thermodynamic processes. A clear picture of the current trends can be drawn from a few specific experimental work. Our purpose is obviously not to provide an exhaustive review of the domain which gathers a large number of work, both from theoretical and experimental sides. We rather aim to highlight how recent experiments have demonstrated the relevance of this approach.

1.5.1 *Thermodynamic laws*

A new generation of experiments has indeed emerged recently, capable of probing the laws of thermodynamics for such small systems as optically trapped particle and on such short time scales as to reach a resolution at the level of the fluctuations themselves.

A striking illustration is provided by the work of Wang *et al.* [51] demonstrating a fluctuation theorem predicting a violation of the Second Law, by studying carefully on the short time scale, the fluctuations of a trapped 6.3 µm latex bead in water. The piezo stage holding the sample is displaced at low frequency, moving the fluid around the trapped object while the trajectory of the bead is recorded. For long time scales (seconds) no production of entropy was measured when analyzing the bead trajectories. This is in accordance with the Second Law of (macroscopic) thermodynamics. It was however observed that for short timescales some trajectories produce entropy while some others are entropy consuming trajectories. This violates for short periods usual thermodynamics concepts. On average however, the number of consuming and producing trajectory is such that when considering time or ensemble averages the second law is recovered [52].

These fluctuating thermodynamic quantities are further studied in order to understand irreversibility in out-of-equilibrium systems. Giesler *et al.* [14] have explored these regimes with a small silica nano-particle trapped in high vacuum, studying in great details the relaxation of this under-damped nano-particle from a non-equilibrium steady sate to an thermal equilibrium state. Using a feedback cooling mechanism, the nano-particle is brought out of equilibrium, prepared in a localized position in space before it is released in the (non-cooled) trap potential, relaxing to its equilibrium distribution. The whole evolution of the process towards the equilibrium state is monitored and the associated thermodynamical quantities are determined. This experiment is also performed for the nano-particle spatially far from its equilibrium position by applying an external drive on the object before the beginning of the relaxation process.

A closely related experiment was performed by Lee *et al.* [53] with a 2 µm dielectric bead (PMMA) in dodecane. In this experiment, the trap stiffness is periodically modulated, driving

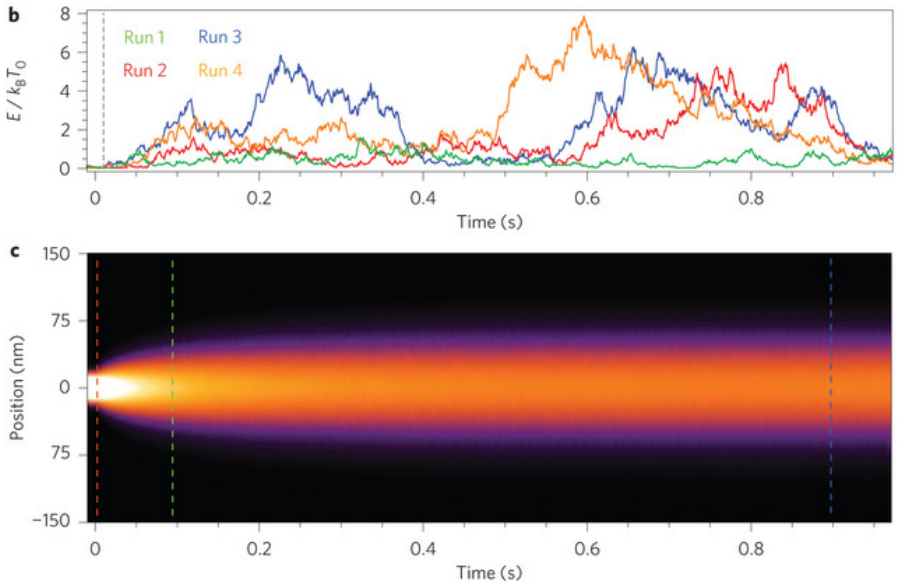

Figure 1.3: A bead is prepared in an out-of-equilibrium position via feedback-cooling. At time t=0 it is let to relax in the trapping potential. The upper graph shows a few bead trajectories, it takes some time for individual objects to reach their equilibrium energy $k_B T$. The lower graph represents trajectory positions as a density plot. This illustration is directly taken from [14].

the system out of equilibrium, the work production is measured and associated microscopic fluctuation theorems is verified [52].

These recent advances in the field of optical tweezers have allowed to measure a large variety of processes, and to test many of the recent theoretical predictions derived from stochastic thermodynamics, among which the so-called fluctuation theorems have a central importance [12].

Recently, new experimental techniques have been proposed that enable to inducing and controlling an effective kinetic temperature of the bath via the control of an external source of noise density. Such techniques have allowed the implementation of so-called adiabatic processes. Such processes are important to understand: they are central in the context of molecular and biological micro- and nano-engines. They are remarkable in the mean sense, where no heat flow is involved through a given non-isothermal sequence (one of the sequence composing the Carnot cycle) by virtue of an averaging procedure over many trajectories. Optical tweezers offer a unique way to repeat, on a single particle, similar

dynamic sequences, while fixing initial state conditions. Such an approach provides full control on trajectories and the means to perform controlled averaging procedures [54].

1.5.2 *Brownian heat engines*

Working in fluids gives a simple way for modifying the temperature of the thermal bath within which the Brownian dynamics evolves. Combining this with a control of the stiffness of the optical trap has led to the realization of a Stirling engine where an optically trapped particle diffuses in different thermal baths, coupled periodically through a time-dependent optical potential [55]. The approach has been extended, where a charged microsphere, optically trapped, is subjected to a noisy electrostatic force [56]. This additional noise source defines an effective kinetics temperature that can be precisely controlled and through which adiabatic processes can be implemented [57]. With such adiabatic paths in the cycle (absent in a Stirling cycle), the energetics of a genuine single-particle Carnot engine have been given.

In their work, Blickle and Bechinger have realized an (external) heat engine of a system consisting of a 2.94 µm Melamine bead trapped by a near IR (1064 nm) laser beam in a fluidic cell of 4 µm. A periodic work is injected in the system through a full thermodynamic cycle which is presented on Fig. 1.4. It consists of first, an increase in the trap stiffness, a compression done by the increase of the trap laser intensity. The sudden heating of the surrounding medium by a strong laser irradiation of water (exciting absorption bands) provides an isochoric transition. After that an isothermal expansion is once again performed by decreasing the trap laser intensity and finally room temperature is recovered, completing the Stirling cycle. The study of a cycle with duration provides the determination of the maximum power the extracted out of the system.

Martinez *et al.* performed a similar experiment but with the different steps of the cycle, in particular with the introduction of isentropic transitions in place of the isochoric of the Stirling cycle. The temperature of the fluid is effectively heated by injecting an electrostatic noise source on the bead. This external force will add itself with to thermal fluctuations providing an effective kinetic temperature higher than the one of the bath. Simultaneously, the trap stiffness is controlled in

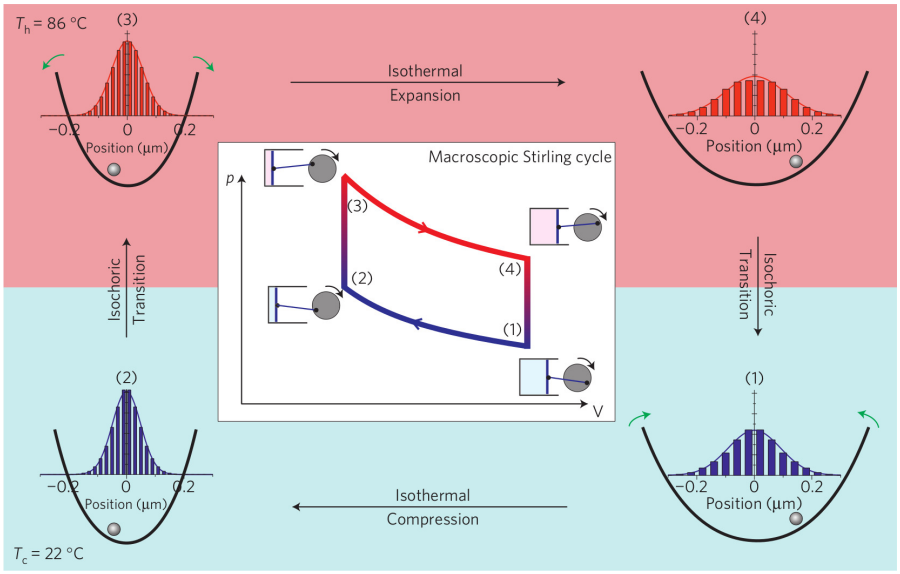

Figure 1.4: Schematic representation of a Stirling cycle and its microscopic realization with a trapped dielectric colloid. This illustration is directly taken from [55].

such a way as to lead adiabatic transitions [54]. Performing a large number of cycles at low frequencies, these authors recover the behavior of a genuine Carnot engine. They also notice that on short times, the Carnot bound can be surpassed, a typical thermodynamical behavior of small systems fluctuating in environment of high bath noise amplitude [52].

1.5.3 *Statistical physics and Information theory*

Another fascinating aspect that can be explored with optical tweezers is the relation between stochastic thermodynamics and information. It was stressed indeed long ago by R. Landauer [58] that an overdamped particle in a double-well potential can be seen as a model for a one-bit memory. This picture has been central in recent tests of the Landauer's principle. The exact form of the double-well potential created by standard dual beam optical tweezers is controlled by the laser intensity and by the distance between the optical axis associated with each beams. Under such control, erasure protocols have been implemented with stochastic trajectories of the trapped particle recorded at each step of the erasure cycle. Utilizing the experimental setup of Jop *et al.*, Bérut *et al.* [15] were able to implement a sequence of preparation, erasing and writing protocols. Such a sequence was performed

by considering each of the bistable potential wells as one bit of the binary system. Under such frame work, a bead is placed in one of the bistable potential well under a strong beam intensity, is thus confined to a well defined state/bit. The intensity is then reduced and the potential tilted, erasing the previous state memory and forcing the bead to change well (state/bit), finally the intensity is increased again, the bead has changed state and the system has experienced a *bit flip*. Thermodynamics of this irreversible process provides the quantity of heat given to the bath and the quantity of entropy produced. Here too, a careful analysis of the thermodynamics associated with the experimental trajectories of the bead, that can be monitored in real time, has led to determine an average dissipated heat in agreement with the so-called fundamental Landauer bound putting a minimal amount of heat dissipation per bit at $k_B T \ln(2)$.

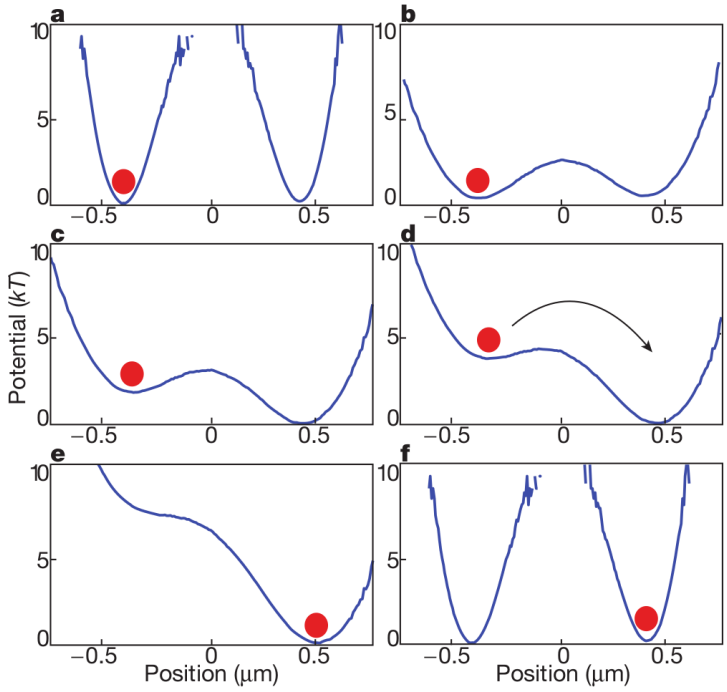

Figure 1.5: Schematic representation of the experimental Landauer erasure protocol. A bead is prepared in a state by being confined in a high intensity field. Intensity is lowered and the potential is tilted, forcing the bead to change well. After the state change, the intensity is increased again. This illustration is directly taken from [15].

Recent experiments on the notion of symmetry breaking in the context of double-well potential (i.e. the abrupt choice

taken by the trapped bead to chose one of the metastable state with respect to the other) have also been proposed. By displacing progressively the laser beams with respect to one another, it is possible to induce a continuous transition from a single to a double-well optical potential. Monitoring the trajectory of the bead at the onset of the double-well potential, and cyclically repeating the protocol, it is possible to acquire an ensemble of trajectories displaying the statistics associated with the fall of the bead in one of the metastable state. Taking this as a symmetry breaking event, it becomes possible to measure the ensemble entropy production associated with the symmetry breaking. For their experiments, Roldan *et al.* [16] considered averaged trajectories of 1 µm polystyrene beads in an optical trap composed of two beams with one of them being mobile. Here too, the thermodynamic limits to information erasure, so-called Landauer's bound, was measured, with interesting connection made in relation with the original picture of Maxwell's demon.

1.5.4 *Kramers-type dynamics*

Optical traps can also work as model systems for testing Kramers' theory on thermally activated escape from a potential well. This thesis will largely focus on the Kramers process, developing an approach based on a standing wave optical trap. This approach contrasts with the previous experimental work performed in this context, where the double-well potential is realized via two spatially separated attractors.

Such double-well optical potentials have been induced either by using two laser beams [8] or by the rapid displacement of the optical trap beam [22]. Using the two-beam technique, the predictions of Kramers' theory have been verified by monitoring the Brownian dynamics of the trapped particle, recorded in 3 dimensions. McCann *et al.* [8] setup is a dual beam trap formed by focusing two beams through a single 100x high 1.4 NA objective. Silica beads of 0.6 µm in size are dispersed in water and trapped, exhibiting a dynamical activation from one focal position to the other. One bead trajectory is imaged by a CCD camera and assuming a linear calibration in all three spatial directions the potential is determined through Boltzmann distribution at equilibrium. Considering the plane of bistable dynamics, the potential is fit with a 4th order polynomial (Duffing-type potential) and the extracted coefficients provide

a measurement of Kramers activation rate. Measured values match with rates measured from residency times.

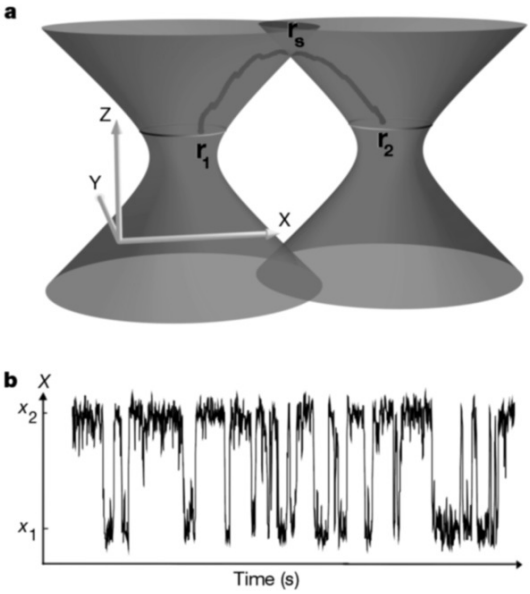

Figure 1.6: Schematic representation of the two Gaussian beam forming a 3D bistable landscape to trap a dielectric bead. The transverse displacement of the bead exhibits a interwell activation of the bead. The associated time trace for the lateral displacement shows a typical bistable dynamics. Illustration directly taken from [8].

The double-well potential has also been studied in relation with the problem of stochastic synchronization or stochastic resonance. With a small amplitude modulation of the power of the divided laser beams, it is possible to modulate the depths of the well. Synchronization of the escape rates has been observed and measured. Simon and Libchaber [7] use an experimental setup similar to the one of McCann *et al.*, trapping 1 µm silica beads with the addition that beam intensities are controlled by the use of rotating optical densities. Periodic changes in the beams intensities tilts the potential. This simulates the addition of an external sinusoidal force applied on the bead. It is observed that when the drive period matches half Kramers natural residency times, the probability of changing state increases compared to slower or faster potential modulations.

Recently, the work and dissipation fluctuations associated with such a synchronization process have been measured precisely. A time shared dual trap was setup by Jop *et al.* [22]

where a single NIR laser (1064 nm) is dispatched over two positions by an acousto-optic deflector (AOD) at 5 kHz. A 2 µm bead sees, and explores effectively, a two well potential separated by a barrier. A Duffing-like potential is fit and Kramers rate coefficients are extracted. The depth of the potential is changed with an unequal ratio of light exposition on the two trap positions (by biasing the AOD intensity distribution). This asymmetry is periodically modulated and is equivalent to the application of a periodic force on top of the unperturbed potential. The probability for the bead to change state by following the drive at different frequencies is determined and the associated consumption of the injected work is computed. At frequencies approximately half the natural Kramers state change rate the maximum of work consumption is reached. Comparing the distribution of work and dissipated heat through the resonance, these authors have been able to test the validity of the steady-sate fluctuation theorem for a non-linear potential.

1.6 SUMMARY

The impressive experimental versatility and power of optical tweezing in defining a large variety of highly controllable configurations has led to build genuine experimental platforms where key concepts of fundamental physics can be easily probed and verified. These work have clearly shown the potential and promises of optically trapped particles as test-systems for fundamental statistical physics.

In this thesis, we will be particularly interested in the description of the stochastic motion of a nano-particle trapped in a bistable interaction potential. We will try to make the best use of some specific tools available in the context of optical trapping in order to study with precision the interplay between thermal fluctuations and dynamical non-linearities.

We note that recent experiments have clearly stressed the relevance of the phenomenon of stochastic resonance in precision measurements, in particular when measuring weak forces at the level of mechanical systems. For instance, a stochastic resonance effect has been studied in non-linear bistable nanomechanical resonators (doubly-clamped) with the fundamental mode of the vibrating beams of the resonator excited by an external periodic optical force [59]. The system was described with a Duffing-type forced dynamics and the signatures of

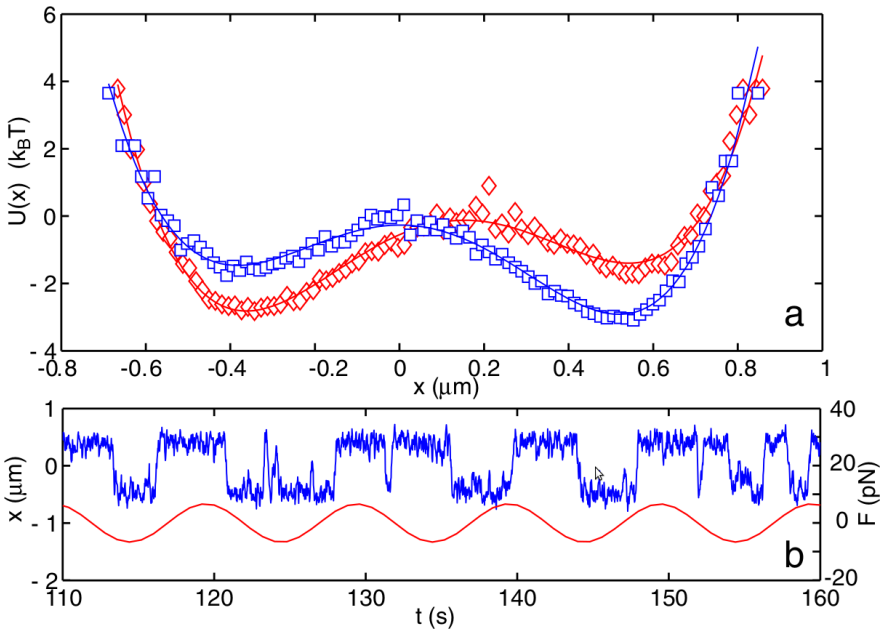

Figure 1.7: Schematic representation of the effective potential obtained from variations of the effective potential intensity by biasing the time ratio the trap beam is exposed. The potential is mapped for the two extreme potential configurations (separated by half a period). The experimental time trace for one realization with a drive amplitude matching the natural transition frequency. Illustration directly taken from [22].

the stochastic resonance were measured both in the time and frequency domains. Another work has exploited the phenomenon on a torsional oscillator leading to an increase of the signal-over-noise ratio (SNR) at the synchronization threshold [60]. The torsional oscillator was coupled to a cavity to have its rotational dynamics evolve in a bistable potential. The deflection of a weak probe laser beam provides a measurement of the angle of the torsion bar. Applying periodical electrostatic forces on the metallic oscillator exhibit a non linear response in the SNR with a maximum increase for drive frequencies half the natural rotation state change frequency (i.e. Kramers rotational frequency).

Considering that optical trapping combines two important ingredients:

- the possibility to induce well-controlled bistable potentials -as we discuss in our Ch. 2, 3 and 4

- and the fact that an optically trapped nano-particle can turn into a highly sensitive force transducer -as described in our Ch. 5,

it becomes clear that such perspectives on stochastic non-linear systems are important to study in the context of optical trapping. They justify, at our level, the precise study on bistable interaction potentials and metastable dynamics in the framework of optical tweezing.

2

THE OPTICAL PISTON

In this chapter, we determine the interaction potential of a thermalized over-damped Brownian particle, at room temperature, optically trapped in front of a mirror in both stable and bistable potentials. For specific positions of the mirror, the coherent superposition of the incident trapping beam and the reflected beam induces dynamical bistability where the particle is thermally activated between two distinct positions along the optical axis. We demonstrate that the whole interaction potential can be solved by interpreting the two positions as distinguishable metastable states. Diffusion limited escape rates and associated activation energies are extracted, together with the actual distance separating the metastable states. Remarkably, this is performed without any preliminary spatial calibration of our optical setup.

2.1 EXPERIMENTAL SETUP

In this section, the optical setup is presented together with the acquisition scheme that we have developed in order to measure most accurately the fluctuating axial displacement of the bead inside the optical trap.

2.1.1 *Optical setup*

The optical setup used for the experiments that will be presented in the following chapters is sketched in Fig. 2.1. A linearly polarized TEM_{00} beam from a CW diode-laser (Excelsior Spectra-Physics, wavelength $\lambda = 785$ nm, power 45 mW) is sent into a dry objective (Nikon CFI Plan Fluor 60X, 0.85 NA) and focused in a water cell (deionized water, 80 µm thick) enclosing mono-dispersed dielectric polystyrene beads (Thermoscientific Fluoro-Max Red Dyed, refractive index 1.58) of radius 500 nm.

The cell is topped by a 170 μm thick cover slip. Spherical aberrations are compensated by the objective (correction ring set to 0.2 mm).

The laser beam traps a single bead in the vicinity of a movable mirror (300 nm thick evaporated gold film on a glass substrate). The beam is reflected by the mirror and recollected by the objective. It is sent to a non-polarizing cube beam splitter where it is equally divided. Along one arm, the intensity signal is vignetted by a pin-hole and recorded by a PIN photodiode (Thorlabs Det10A). This port provides intensity time-traces that measure the instantaneous axial displacement $z(t)$ of the bead inside the optical trap. The second port is sent to a CCD camera (Allied Guppy Pro F-031) that images the recollected beam spot or to a quadrant photodiode detector when 3-dimensional (x,y,z) position measurements are needed.

The CW diode-laser is optically isolated using a free-space Faraday isolator (Thorlabs IO-5-NIR-LP). The isolation is further improved by injecting the laser beam into the objective using a polarizing cube beam splitter coupled to a quarter-wave plate (QWP). This prevents as much as possible the recollected signal to be send back to the injection port. Working with an input beam that is reflected requires the capacity to reduce by 6 orders of magnitude with respect to the laser emission intensity any light stray traveling in the backward direction towards the diode.

In this beam splitter-QWP configuration, the optical landscape created between the objective lens and the mirror is the coherent superposition of a forward right-handed circularly polarized beam and a backward left-handed circularly polarized beam.

2.1.2 *Photodiode-based detection*

In general, position tracking is performed either by video tracking of the Brownian object or using a PIN photodiode-based detection scheme. Video tracking allows the simultaneous tracking of many particles and a direct and easy spatial calibration for translational motion of the object with respect to the optical axis. But the acquired video must then be treated using pattern recognition and specific tracking software that are often heavy to handle. For single beam optical trapping, a photodiode detector offers a few important advantages over video tracking. First, it enables to follow easily the PIN signal

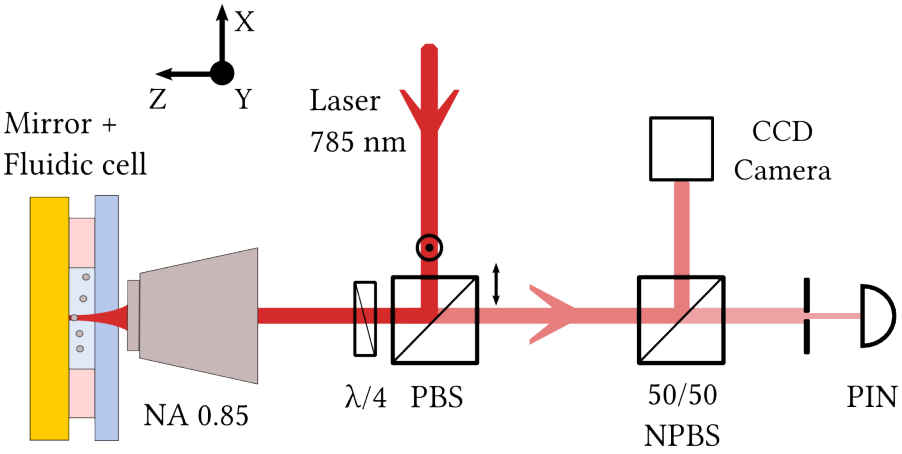

Figure 2.1: Schematics of the experimental setup, indicating in particular the second isolation stage at the level of the polarizing beam splitter (PBS) and the added quarter-wave plate (λ/4). The two ports from the non-polarizing beam splitter (NPBS) used for recording the recollected beam are also represented. In the chosen frame, a right-handed circularly polarized field propagating along the $z > 0$ direction is described with $\boldsymbol{\sigma}_+ = (\hat{\mathbf{x}} - i\hat{\mathbf{y}})/\sqrt{2}$.

in real time using an oscilloscope. Then, a PIN detector yields better sensitivities at higher acquisition rates. This is of importance for measuring Brownian motions over a wide spectral range, when high frequency contributions of the motion to the signal are small and quickly fall down to the noise floor. We however have to keep in mind that in order to have field intensity variations properly measured by the photodiode cell on a few micro-second timescale, high optical field intensities are needed. This simply comes from the mere fact that it is easier to look for small variations in a strong signal than to look for the useful signal on top of a dark background. This constraint added to the bandwidth requirement justifies to exploit the strong signal of the forward scattered light of the trap.

2.1.3 *Amplification and acquisition*

The recollected intensity (which contains the forward scattered light signal reflected on the mirror of the SWOT) is measured by both the QPD and the PIN photodiode. The associated output tensions are then sent to low noise preampli-

fiers (SR560). The PIN signal that records axial displacements through the measured recollected intensity is recorded in AC mode and filtered through a 0.3 Hz high-pass filter at 6 dB/oct in order to remove the continuous DC component of the signal. A low-pass filter at 100 kHz at 6 dB/oct is also used to avoid aliasing for all detectors. This is an important step to take, as emphasized in [61].

High-pass filtering poses no issue since the signal of interest is the dynamical fluctuations and not the continuous component of the intensity. This filtering stage actually permits to span the acquisition card input range with high resolution over the whole dynamics. The exponential decrease of slow varying signals is later taken care of numerically to reconstruct the whole signal (to within a constant), as we will discuss further down.

In order to acquire the signal, the analog tension is digitally converted using an NI PCI-6251 analog-to-digital conversion acquisition card. The tension issued from the amplification stage corresponding to the light intensity on the photodiode is maximized to all the 16 bits available on the acquisition card in order to record the signal as accurately as possible.

2.1.4 *Modeling the acquisition chain*

We can justify our data acquisition scheme with a simple modeling of the whole physical chain, going from the light beam incident on the photodiode to the acquired tension.

Let $x(t)$ be the physical displacement of the bead at a time t.The intensity $I(t)$ incident on the photodetector is the intensity laser which confines the bead after being reflected on the mirror and sent to the photodetector. This intensity can be classically expressed as $I(t) = I_0 + \delta I(t)$ where the small intensity fluctuations $\delta I(t)$ comes from the forward scattering fluctuating signal coming from the Brownian displacement of the bead in the fluid (we neglect any optical noise sources as they are smaller than the thermal noise). This implies that $\delta I(t)$ a functional of the bead displacement. For small objects, like metallic nanoparticles, the measured intensity stems from the interference between the laser beam and the spherical wave scattered in the forward direction by the object and then reflected by the mirror towards the detector.

Intensity variations $\delta I(t)$ on the detector are in fact built on two contributions that interfere: the forward scattered

light and the reflected trapping light. A precise relationship between the measured intensity and the displacement z_B of the bead along the optical axis has been derived in the Rayleigh approximation for a Gaussiam beam in ref. [62]. The measured intensity on the detector turns out to be equal to

$$I_z(z_B) \propto \frac{\sin\left(\arctan\left(\frac{z_B}{z_R}^2\right)\right)}{\sqrt{\left(1+\frac{z_B}{z_R}\right)}}. \tag{2.1}$$

The relation shows that the signal is linear in z_B around the waist for displacements much smaller than the Rayleigh range z_R. As the numerical aperture increases the Rayleigh range dicreases, in our case, using a NA = 0.85 this range is

$$\begin{aligned} z_R &= \frac{\lambda}{\pi\, NA^2} && (2.2)\\ &= \frac{589}{\pi\, 0.85^2} && (2.3)\\ &= 260 \text{ nm}. && (2.4) \end{aligned}$$

The Rayleigh range is of the same order of magnitude as inter-well displacements measured in the bistable configuration. This analysis, even though in the Rayleigh regime justifies the precautions employed when measuring distances along the optical axis. Some methods have been proposed to calibrate the intensity response with respect to the bead position[63] for direct position measurement.

In the case of larger dielectric objects, the beam waist is smaller than the diameter of the bead which acts as a lens for the gaussian trapping beam. At different bead positions the transmitted beam at the objective entrance is more or less expanded . The collected intensity is then vignetted by the objective, leaving only the center of the beam to be transmitted. This phenomenon is clearly illustrated on Fig. 2.6. Regardless of the bead size and material used, the measured intensity is a complex function of the bead displacement. In our case a direct measurement of the bead position is not attempted over the full space of explored positions. Nevertheless linearity between the measured intensity and the bead position is assumed at the bottom of the wells.

Over a given time interval, the photodetector converts the laser intensity $I(t)$ into an electron flux, eventually measured as a potential in Volts. The detector response is assumed to

be linear, i.e. the light intensity reaches levels corresponding to a regime where voltage and intensity are related by a simple affine function $V(t) = DI(t)+V_0$ with V_0 some voltage offset and D the coefficient converting Joules to Volts. This linearity also assumes that the measured signal is slower than the detector bandwidth.

Since $V(t)$ is very weak in our experiments, it is necessary to amplified it with an additional small offset coming from the amplification chain. This small offset can become significant after amplification with respect to the amplitude of the signal intensity itself. We define $S(t) = BV(t) + S_0$ as our new linearly amplified signal with B the amplification gain (dimensionless) and S_0 a constant offset induced by the amplification stage. Replacing $V(t)$ into $S(t)$ yields

$$S(t) = B(D(\delta I(t) + I_0) + V_0) + S_0 \tag{2.5}$$
$$= BD\delta I(t) + C, \tag{2.6}$$

with $C = BDI_0 + BV_0 + S_0$ a constant signal independent of time. While the signal of interest is contained within $\delta I(t)$, the constant term C turns out to be large.

There are two common approaches to deal with this large DC component. A first approach is to split the whole signal $S(t)$ by differential measurements in two then subtracted to each other such that the constant term is nullified. The second approach is to use a high pass filter which in practice cuts the constant term C by exponentially decaying low frequency signals to zero. This approach is more constraining since any low frequency contribution that could be relevant on $\delta I(t)$ will get cut and therefore harder to notice. In practice, and regardless of the method chosen, this "zero" has always a residual finite value F_0 in Volts. Furthermore, the acquisition card does not have the exact same 0 V reference as the preamplifier but is assumed to have its own constant voltage offset G_0.

The resulting signal after applying one of the two method becomes $S(t) = BD\delta I(t)+K_0$, with $K_0 = F_0+G_0$. If the amplifiers and acquisition card are properly calibrated, the offset K_0 should be bellow 0.1 % of the acquisition range. In practice again, one grounds the preamplifier after having all other parameters properly set (amplification and filters frequencies) and then performs an acquisition through the acquisition card to determine K_0. This K_0 offset is then subtracted from all time traces measured afterwards.

2.1.5 *Calibration*

In our experiments, the study of the dynamics of the bead in space is performed by measuring its positions and forces, implying therefore the acquired voltage to be converted back in meters. This is the central issue of calibration that demands specific care in any optical trapping experiment.

Going ahead with our initial analysis, we assume that $\delta I(t) = A\delta x(t)$, with A in $J \cdot m^{-1}$, holds for small bead displacements, i.e. at the bottom of the trapping potential where the detection response is linear.

We then want to determine the linear term β converting the measured Volts into spatial displacements of the bead in meters: $A(t) = \beta\delta x(t)$ with $\beta = BDA$. There are several methods available for determining this coefficient which are described in the literature [64, 65].

One common approach is to assume that the intensity is linear with the bead displacement over the whole acquisition range and apply one of various possible calibration schemes, either by comparing the bead confinement with the equipartition and a theoretically known drag coefficient [64] or by a more sophisticated method which proposes to circumvent the necessity of an a priori knowledge of the drag by applying a completely known external drive on the trapped object in order to determine its position and force calibration [65].

The different calibration methods are compared in [66].

The whole point of our acquisition chain is to construct a signal linear with the bead displacement (and with decent resolution) in order to calibrate our system most easily. This is directly done for lateral displacements using the QPD. The beam, centered on the 4 quadrants will have all constant and continuous components compensated when computing the differences between the quadrants, with therefore the constant C equals 0 for all frequencies without need for a high-pass filter. The axial displacement (movements along the optical axis) is obtained by removing, through high-pass filtering, any slow variations of the large constant background. This procedure leads to a signal that only contains the dynamical information because all contributions unrelated to the bead displacement like the direct transmission from the laser are almost entirely cut after 3 times constant of the high-pass filter (i.e. 3s when the high-pass filter has a cut-off frequency of 1s). This way C is effectively considered to be 0 in our experiments. Because the 3 signals each associated with a spatial dimension are similar (the

dynamics is for all centered around 0), they are analyzed in the same way.

Obviously all of this makes sense only if the computed Power Spectrum has the proper normalization so that we can link its amplitude with the physical displacement $\delta x(t)$.

To summarize, the approach is to construct a signal that is as linear as possible (around its origin) with the variations of the bead displacement. Such a construction is obtained 1) by the use of balanced photodetection (in our single beam tweezer configuration, a quadrant photodiode) for transverse displacements and 2) by high-pass filtering the light intensity for axial displacements. Our method turns out to be interesting because all three axial displacement signals have the same shape, only the bead dynamics is recorded and centered on 0V. This way the exact same treatment is applied on all of them.

2.1.6 *Numerical reconstruction of the dynamics*

This section discusses in more details the procedure through which the acquisition signal is high-pass filtered, its implications and the numerical treatment performed after acquisition to reconstruct the recollected signal intensity on the photodiode.

High-pass filtering is mandatory to acquire intensity fluctuations coming from the bead displacement with good resolution. Such fluctuations correspond to meaningful values only if they span the whole acquisition card dynamical range. But our experiments are confronted to another difficulty: dealing with bistable signals implies to be able to monitor changes in the mean intensity values while keeping track of the fluctuations at a high resolution level. It is precisely this mean intensity value that changes each times the particle jumps from one potential well to the other and it is that same mean that changes in time as the dynamical configuration progressively evolves under the external action of the displacement of the mirror.

Since such a mean intensity value is cut-off by the high-pass filtering stage, we need to find a trade-off where configuration changes can be properly filtered while dynamical changes are recorded despite the fact that the signal is distorted. In fact, we are able to correct for this distortion numerically, after the acquisition sequence, by using the scheme now described.

A first order high-pass filter is described by an RC electric circuit with the following temporal expressions

$$\begin{cases} V_{out}(t) = I(t)R \\ Q_c(t) = C(V_{in}(t) - V_{out}(t)) \\ I(t) = D_t(Q_c(t)) \end{cases} \tag{2.7}$$

This yields to

$$V_{out}(t) = D_t(Q_c(t))R = D_t(C(V_{in}(t) - V_{out}(t)))R \tag{2.8}$$

$$= \frac{D_t(V_{in}(t) - V_{out}(t))}{\tau}, \tag{2.9}$$

with $\tau = RC$ the characteristic time of the filter. The temporal

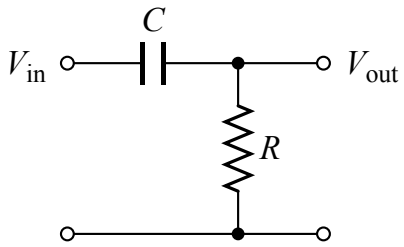

Figure 2.2: Schematic of a typical first order RC high pass filter. (source: wikimedia)

response of the filter is a first-order differential equation. We define $K(t) = V_{in}(t) - V_{out}(t)$ and solve the equation for $K(t)$. We then transform it back to have the response written as:

$$V_{out}(t) = V_{in}(t) - e^{-t/\tau}\left(\int_{t_0}^{t} \frac{V_{in}(t')}{\tau} e^{t'/\tau} dt' + (V_{in}(t = t_0) - V_{out}(t = t_0))\right), \tag{2.10}$$

taking $t_0 = 0$ and $V_{out}(t = t_0) = 0$ so that the integration constant equals to $V_{in}(t = t_0)$. To illustrate this expression, one can take $V_{in}(t) = V_{i_0}$ a constant and obtain that $V_{out}(t) = e^{-t/\tau}V_{i_0}$ which tends to zero after some time with decay constant τ. The filter will tend to subtract $V_{in}(t)$ to its integrated history (ignoring the initial condition) thus removing after some time any slow or constant amplitude in the signal. The expression for

the input signal as a function of the output is also analytically obtained for a characteristic time of the filter.

$$V_{in}(t) = V_{out}(t) + \int_{t_0}^{t} \frac{V_{out}(t')}{\tau} dt' + (V_{in}(t = t_0) - V_{out}(t = t_0)) \tag{2.11}$$

Expression (2.9) is the operation performed by the high pass filter in the pre-amplifier looked from a "local" perspective, by infinitesimal steps. From the measured signal $V_{out}(t)$, the "true" signal $V_{in}(t)$ at the output of the photodiode is recovered by solving the equation

$$D_t(V_{in}(t)) = \frac{V_{out}(t) + \tau\, D_t(V_{out}(t))}{\tau}. \tag{2.12}$$

Whenever the filtered signal is well recorded with an acquisition time step smaller than the high-pass filter time constant, the exponential decrease of the acquired signal can be easily corrected. Although this procedure does not allow recovering the constant amplitude of the original signal which was already cut before the acquisition started, as discussed above, our analysis does not require this constant value. The correction procedure is illustrated on Fig. 2.3. The orange curve is the signal directly recorded after filtering. It is striking to observe the expected decay (see Eq. (2.10) of the acquired signal after the bead has jumped to another well along the optical axis. The blue curve is the same signal after the correction of the filter (2.12) is performed. This correction leads to the expected separation of the instantaneous positional signal of the trapped bead trajectory into two mean positions.

Of course, this correction is implemented numerically. To perform it, the following scheme is applied to the filtered signal. We first change variables $X(t) = V_{in}(t)$ and $Y(t) = V_{out}(t)$ and by discretisation of the differential operator $D_t()$ as the τ is big with respect to the acquisition rate ($\tau \gg \Delta t$) we will solve eq (2.12) by iteration. Variables are then transformed to their discrete equivalent, $X(t) = x_i$, $Y(t) = y_i$, $D_t(X(t)) = \frac{x_i - x_{i-1}}{\Delta t}$ and $D_t(Y(t)) = \frac{y_i - y_{i-1}}{\Delta t}$, the y_i being the acquired point of our signal and the x_i points represent the unfiltered signal. The discrete equation becomes,

$$x_i = \Gamma y_i - y_{i-1} + x_{i-1}, \tag{2.13}$$

with $\Gamma = \frac{\Delta t+\tau}{\tau}$. The actual results are presented in Figure (2.3) where the acquired signal that is high-pass filtered (time constant of one second) is displayed in orange and in blue the result after removing numerically the contribution coming from the filter.

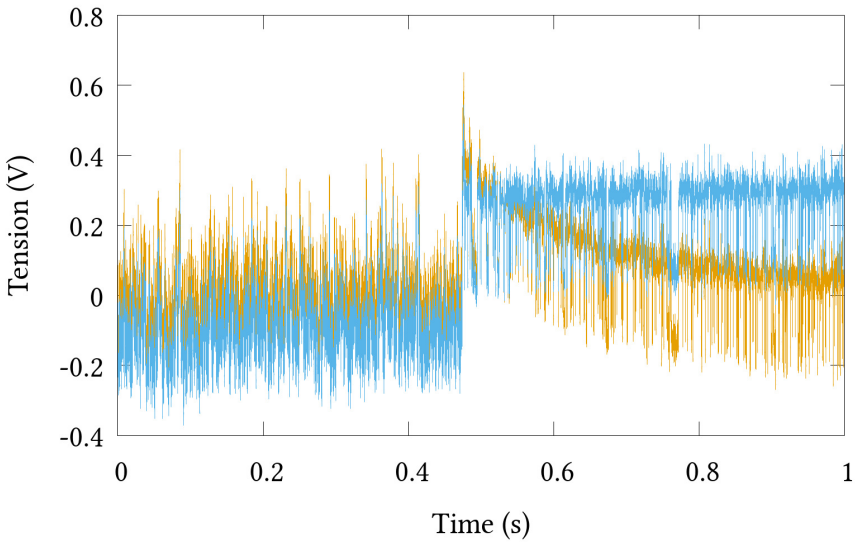

Figure 2.3: The orange curve corresponds to the direct time-trace of the recorded signal. We can clearly observe the exponential decay of the signal after the bead has "jumped" to another metastable position of the bistable potential due to the high-pass analog filter with characteristic time τ of 1 second. The blue curve displays the same time-trace signal after the filtering effect is removed numerically by applying Eq. (2.13) to the orange time-trace.

2.2 THE OPTICAL PISTON: CONTROLLING OPTICAL POTENTIALS WITH AN EXTERNAL PARAMETER

In our experiment, a single polystyrene bead is optically trapped by a focused Gaussian beam in a water cell at a typical 2 μm distance from a metallic mirror. The trapping beam, characterized by a fixed waist w_0 located at $z = 0$, propagates in the fluid along the $z > 0$ optical axis with a wave vector $+k$ -see Fig. 2.4 (a). It is $M\times$ magnified through the transparent bead acting as a lens and reflected with a reflection amplitude $r[\lambda]$ by the mirror placed at a distance ℓ from w_0. This creates

a coherent optical landscape at the position of the bead z measured from the waist

$$I_M^{opt}(z,\ell) \propto |\mathbf{E}^{+k}(z) + r[\lambda] \cdot \mathbf{E}_M^{-k}(z-2\ell)|^2, \tag{2.14}$$

displayed in Fig. 2.4 (b) as a function of z and ℓ for a fixed value of M. As expected from its interfering nature, the optical landscape profile changes with the waist-mirror distance ℓ.

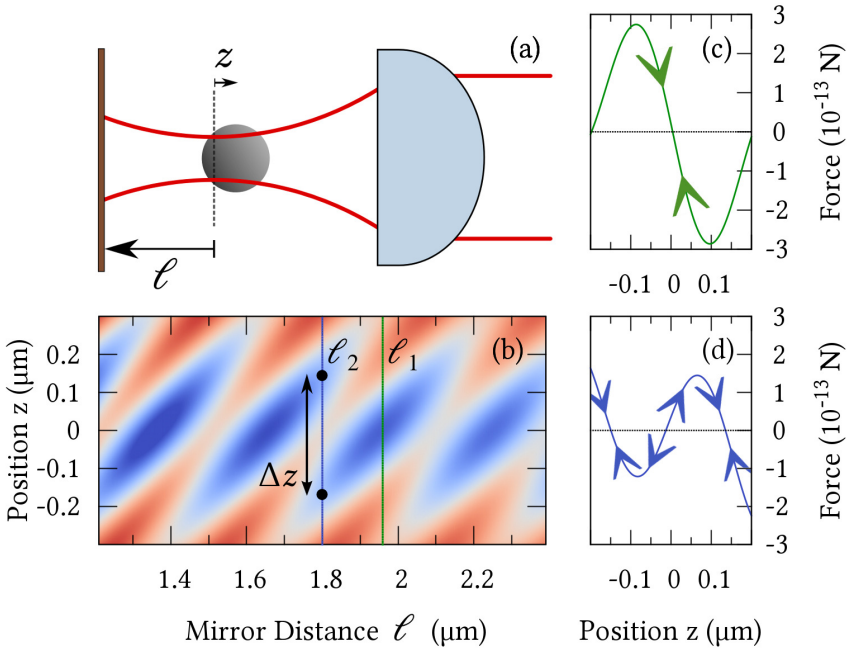

Figure 2.4: (a) Sketch of the trapping configuration. A micron-size bead (radius R = 500 nm) is trapped by a Gaussian beam ($\lambda = 785$ nm) focused through a microscope objective. The position of the bead z is defined with respect to the beam waist w_0. The end-mirror is positioned at a distance ℓ from the waist. (b) Evolution of the optical landscape in the vicinity of the waist ($z = 0$) and as a function of ℓ. Blue colors correspond to regions of higher intensity, i.e. deeper potential energy and thus to stable positions. The case of a stable landscape corresponds to the distance ℓ_1 (green line) and a bistable landscape is crossed at ℓ_2 (blue line). Plots of the force diagrams associated with ℓ_1-stability (c) and ℓ_2-bistability (d).

2.2.1 *Experimental scheme and stationary wave structure: towards bistability*

The corresponding evolution has direct consequences on the dynamics of the trapped bead in the vicinity of the waist. Although the approach we develop below is fully general, these consequences are most easily described in a dipolar approach. Here, the non-absorbing bead is modeled by a real dipolar polarizability α and the optical interaction potential is $U_M(z,\ell) = -A \cdot \alpha \cdot I_M^{opt}(z,\ell)/(2\varepsilon_0 n_2 c)$, with n_2 the refractive index of the fluid. The coupling constant A allows accounting for bead size effects, with $A \ll 1$ beyond the dipolar limit [67]. Within such an approach, the time-averaged conservative optical forces acting on the bead directly derive from the potential energies $\mathbf{F}_{opt}(z,\ell) = -\partial_z U_M(z,\ell)$. The dipolar approach therefore reveals in a straightforward way the crucial property that the optical force field is directly determined from the optical landscape, for every choice of ℓ.

Because of the coherent nature of Eq. (2.14), one dynamical configuration can be selected from the distribution of the successive resonant phase conditions in the (z,ℓ) space. For instance, picking at ℓ_1 a resonant phase condition precisely on the waist as shown in Fig. 2.4 (b) leads to restoring forces that will maintain the bead in a stable trapped position at $z = 0$ as displayed in Fig. 2.4 (c). But a mere decrease of the waist-mirror distance to ℓ_2 brings a bistable configuration where the resonant phase evolution induces regions of local stability from both sides of the waist separated by an unstable point at $z = 0$, as seen in the bistable force diagram Fig. 2.4 (d). This roots the analogy with a piston-like action exerted by the mirror on the Brownian bead, where the walls confining the bead are of an optical nature.

2.2.1.1 *Axial 1D displacement*

The stochastic trajectory $z(t)$ of the bead evolves in every such ℓ-configuration, modulating, by forward scattering of the trapping beam, the intensity recollected by the objective. The time-traces of these modulations allow us to retrieve the essential features of the potentials explored by the bead. The bistable behavior of the bead can be monitored on the CCD camera because the motion of the bead along the optical axis and across the bistability barrier changes the Gaussian envelope of the reflected beam and thus the diffraction pattern of the

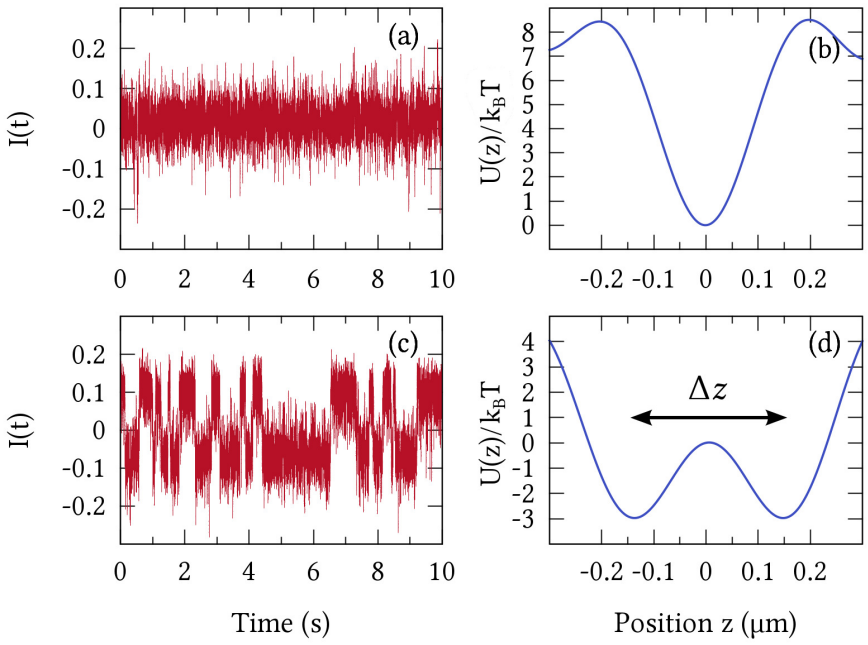

Figure 2.5: Experimental intensity time traces respectively associated with a Brownian motion in a quasi-harmonic well (a) and in a bistable potential between two distant spatial positions (c). The plots (in units of k_BT) in (b) and (d) are the potentials associated with the time traces (a) and (c), respectively.

recollected beam imaged on the camera, as shown in Fig (2.6). Thus, by the sole measurement of the recollected intensity, one can access part of the bead dynamics. Nevertheless, the low acquisition rate of the CCD camera is a strong limitation for analyzing precisely the stochastic motion of the bead.

Other experiments have reported bistable dynamics along the optical axis [68].

In this experiment, the recollected beam is spatially filtered before the PIN photodiode through a pinhole (typical aperture of about 1 mm^2). This spatial filtering is useful since it actually enhances the separation between the two average intensities in the bistable configurations. Note that this is a mere enhancement effect since even without any spatial filtering, we still detect clearly a difference in intensity values that is therefore solely related to the positional dynamics of the bead. The same difference is observed simply using a lens to focus the beam on the PIN. This lens-based scheme however distorts even more the relationship between intensity and distance over the full measurement range.

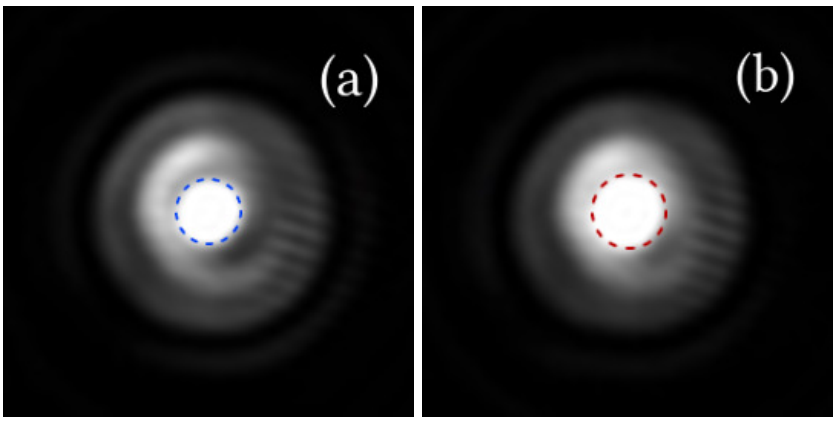

Figure 2.6: Recollected spots imaged on the CCD camera in the case of a bead trapped in a bistable configuration. with same exposition time. Panel (a) shows the bead in its most distant position from the mirror, i.e. the position behind the waist ($z < 0$). Panel (b) shows the bead in front of the waist, thus closer to the mirror. The recollected intensity is higher near the mirror (image (b)) than away from it. The central area of the recollected spot is indicated by the superimposed circles, with a 44 pixel-diameter for (a) and 50 for (b).

2.2.1.2 *Temporal timetraces*

For the stable ℓ_1-configuration of Fig. 2.4 (c), the time-trace is displayed in Fig. 2.5 (a) and corresponds to a Brownian motion performed in an quasi-harmonic potential probed by the bead at the bottom of the whole optical potential shown in Fig. 2.5 (b). The time-trace displayed in Fig. 2.5 (c) corresponds to the bistable ℓ_2-configuration of Fig. 2.4 (d). The intermittency of the intensity signal between the two distinguishable mean values is the signature of the activation of the bead between two metastable positions along the optical axis. There are indeed clearly two different time scales: a short one associated with Brownian fluctuations, and a much longer one on which take place activating events from one to the other of these two positions. In each metastable states, similar time-traces as those of Fig. 2.5 (a) reveal a quasi-harmonic motion, expected for local equilibrium. Therefore, while the bead performs its Brownian motion within a local well, it diffuses across the potential barrier through rare events thermally assisted [69].

2.3 SOLVING THE INTERACTION POTENTIAL

This section details the methodology that we developed in order to determine the actual experimental potentials presented in Fig. 2.5. The optical fields and potential expressions are first given and the method of resolution using Kramer's rate equation then formulated. Finally, important properties of the dynamics are explored with *(i)* a study of aging and stationarity features of the bistable configuration, *(ii)* a description of the power spectral signatures of bistability, and *(iii)* a discussion of the possibility to visualize the phase portrait of the bistable Brownian dynamics based on a Hilbert transform approach.

2.3.1 *Optical fields and bistable potential*

The optical field $\mathbf{E}_{\text{tot}}$ created inside the optical piston (i.e. between the objective lens and the mirror) is given by the coherent superposition of an incident and a reflected Gaussian beams. The incident beam is, as explained above, right-handed $\boldsymbol{\sigma}_+$ circularly polarized and described by its Rayleigh range z_R and its waist w_0 position fixed at $z = 0$

$$\mathbf{E}^{+k}(z) = E_{00}\frac{w_0}{w(z;z_R)}\exp\left(ikz - i\xi(z;z_R)\right)\boldsymbol{\sigma}_+ \tag{2.15}$$

with

$$w(z;z_R) = w_0\sqrt{1+\left(\frac{z}{z_R}\right)^2} \tag{2.16}$$

$$\xi(z;z_R) = \arctan\left(\frac{z}{z_R}\right) \tag{2.17}$$

and $z_R = \pi w_0^2/\lambda$, $n_2\lambda = \lambda_0$, the optical wavelength in water (refractive index n_2) and $\pi w_0 = \lambda/\text{NA}$.

The reflected field, counter-propagating $k \to -k$ with respect to the incident beam, is multiplied by a reflectivity coefficient $r[\lambda]$. Its waist position is the mirror-image of the incident waist position. But before being reflected, the incident beam is intercepted by the bead because the bead diameter is larger than the incident waist w_0. Considering that the refractive index of the bead (polystyrene) is different from that of the fluid (water), the incident beam transmitted through the bead is magnified, the bead considered to act as a lens-doublet. We account of this effect by introducing an effective magnification parameter

M on the reflected beam itself. This leads to changing the Rayleigh range $z_R \to M^2 z_R$ and waist $w_0 \to M w_0$ of the reflected beam with respect to the incident beam. The reflected beam, left-handed $\boldsymbol{\sigma}_-$ circularly polarized, is then expressed as:

$$\begin{aligned}\mathbf{E}_M^{-k}(z-2\ell) =& E_{00}\frac{Mw_0}{w(z;M^2z_R)}\times \\ & \exp\left(-ik(z-2\ell)+i\xi(z-2\ell;M^2z_R)\right)\boldsymbol{\sigma}_-.\end{aligned} \tag{2.18}$$

The coherent superposition of the incident and the magnified reflected Gaussian beams determines the optical landscape of the problem. The corresponding optical intensity writes as

$$\begin{aligned}I_M^{opt}(z,\ell)/\alpha_p &= |\mathbf{E}^{+k}(z)+r[\lambda]\cdot\mathbf{E}_M^{-k}(z-2\ell)|^2 \\ &= E_{00}^2\frac{w_0^2}{w^2(z;z_R)}+\rho^2E_{00}^2\frac{w_0^2}{w^2(z-2\ell;M^2z_R)} \\ &+\frac{2\rho E_{00}^2Mw_0^2}{w(z;z_R)w(z-2\ell;M^2z_R)}\times \\ &\qquad \cos\left(2k(z-\ell)-\xi(z;z_R)-\right. \\ &\qquad\qquad \left.\xi(z-2\ell;M^2z_R)+\psi\right).\end{aligned} \tag{2.19}$$

with an interference term between the two beams and α_p the particle polarizability. In the vicinity of the waist, it shows that the modulations of the optical landscape (that will eventually correspond to the local potential barriers, as discussed below) are determined from a harmonic cos term. This immediately stresses that a standard 4^{th} order polynomial description of the barrier is not appropriate for our optical piston configuration. Such a 4^{th} order polynomial description is however the one adopted in a majority of work that resort to a simple Duffing potential $U(x) = 1/4\alpha x^4 - 1/2\beta x^2$ ($\alpha, \beta > 0$) because in this case, Kramers rate equations are analytically solvable.

In the published paper α_p was forgotten in expression (2.19), nevertheless the resulting potential has the correct expression.

But as we checked using the scheme described in the next section below, the interaction potential that can be determined when considering a Duffing potential for our experimental data simply yields unrealistic values. When injecting our experimental values into the Duffing-based rate equations, inconsistencies occur: both rate equations can not be verified simultaneously, the inter-well distance is much smaller than the fringe spacing of the standing wave, and the barrier height is only of the order of the thermal fluctuation k_bT. These inconsistencies with respect to the experimental data clearly show that, the bead deviating strongly from the bottom of the well, it is not possible

to assume that all forces modeling the potential are of the $-\kappa_i z$ type as is the case with a Duffing potential, the shape of the optical field does not permit it.

2.3.2 *Rayleigh regime and conservative forces*

In the dipolar regime, the bead is characterized by an electric polarizability α_p. Neglecting any source of dissipation within the bead, i.e. assuming that $\mathrm{Im}[\alpha_p] \sim 0$, the gradient force is the only force exerted on the bead

$$\mathbf{F}_{opt} = -\partial_z U_M(z,\ell). \tag{2.20}$$

It directly derives from the interaction potential energy determined from the optical landscape intensity as

$$U_M(z,\ell) = -A\alpha_p I_M^{opt}(z,\ell), \tag{2.21}$$

with $\alpha_p = \frac{\alpha}{2\epsilon_0 n_2 c}$ and $\alpha = 4\pi\epsilon_0 n_2^2 a^3[(n_1/n_2)^2-1]/[(n_1/n_2)^2+2]$, n_1 the refractive index of the bead, n_2 the refractive index of the fluid, a the radius of the bead and ϵ_0 the vacuum permittivity.

Despite the fact that it is related to the bead geometry, the M parameter value for the magnification by the bead is not necessarily a constant of the model as it depends on the width of the beam intercepted by the bead. The A parameter quantitatively corrects the value of the potential calculated in our Rayleigh-based model due the finite size of the bead that should be accounted for in a more realistic description of the optical interaction. In fact, the interaction potential turns out to be smaller by approximately 3 orders of magnitude for a 1 μm bead. This value is in good agreement with existing evaluations for the size effect [67]. We stress that because A is a parameter of the model that characterizes the intensity of the coupling of the bead with the optical intensity, it is kept fixed once determined for a given bead.

2.3.3 *Method of resolution: Kramers rate equations*

Kramers theory is based on a couple of conditions that are clearly met in our experiment. The theory first is limited to situations where local attractors separated by one single saddle point are well defined in the dynamical potential landscape. Then, it is crucial that the transitions between the two local

ℓ (μm)	M	A	Δz (nm)	U_{b1} (k_bT)	κ_b (pN/μm)
1.811	1.505	2.92e-3	285	2.98	2.81

κ_1 (pN/μm)	κ_2 (pN/μm)	ΔU (k_bT)	τ_1 (s)	τ_2 (s)
3.35 (3.12)	3.51 (3.85)	-7e-4 (-7e-4)	0.505 (0.526)	0.494 (0.474)

Table 2.1: Parameters of the interaction potential extracted from the resolution method applied to the bistable ℓ_2-configuration. Values directly obtained experimentally are indicated in brackets.

minima are rare, in the sense that the time scale of escape from one attractor to the other is much larger than all other times scales, in particular the typical relaxation time of the bead inside each attractor. This condition on a *separation of time* is a condition on the ratio between the energy scale associated with the fluctuations that make the bead hoping from one attractor to the other and the barrier energetic height E_b. In our situation of a bead in a thermalized fluid, the fluctuation energy scale is simply given by k_bT so that the separation of time corresponds to the $k_bT/E_b << 1$ conditions [23].

As soon as the process is stationary with a sufficient number of recorded activating events, Kramers' theory connects escape rates evaluated from averaged residency time τ_i within each $\{i = 1, 2\}$ well [70]

$$\frac{1}{\tau_i} = \frac{\sqrt{\kappa_i}\sqrt{\kappa_b}}{2\pi\gamma} \exp\left(-\frac{U_M(z_b,\ell) - U_M(z_i,\ell)}{k_BT}\right) \qquad (2.22)$$

to local trap stiffnesses $\kappa_i = \partial_z^2 U_M(z,\ell)|_{z_i}$ that fix the curvature at the bottom of each well, and to the actual shape of the barrier (position z_b and height) through the absolute value of its curvature $\kappa_b = -\partial_z^2 U_M(z,\ell)|_{z_b}$. Taking the ratio of both rates therefore leads to measuring the potential energy difference between the local equilibrium positions $\Delta U = U_M(z_2,\ell) - U_M(z_1,\ell) = k_BT \ln(\tau_1/\tau_2\sqrt{\kappa_1/\kappa_2})$.

The corresponding trap stiffness is measured by a power spectral density (PSD) analysis [61]. At low Reynolds numbers, this only relies on the determination of the roll-off trapping frequency and on the knowledge of the fluid friction coefficient γ. Note that we neglect the $\sim$ 20% systematic error on the perpendicular viscosity when working at a 2 μm distance from the surface [33].

Measured $\kappa_{1,2}$ and $\tau_{1,2}$ provide a non-linear system of equations which solution fixes the three (M, ℓ, A) parameters needed for a definition of the interaction potential. Experimental values having their own uncertainty, the precision on ΔU is below $k_B T/2$ and below 6 nm for ℓ (see uncertainties determination in the next chapter). We also extract from the resolution algorithm the barrier position z_b, inverted curvature κ_b and height, measured as $U_{b1} = U_M(z_b, \ell) - U_M(z_1, \ell)$. The barrier, 3 times higher than $k_B T$, is still shallow enough to allow the bead mapping, through thermal fluctuations, the bistable potential around $z = 0$. The distance Δz over which the bead is activated is also measured. From the parameter values gathered in Table I, the interaction potential profile can be plotted as a function of the bead displacement as in Fig. 2.5 (d) in units of $k_B T$. We stress that the phase structure of I_M^{opt} forbids a simple 4^{th}-order potential (i.e. Duffing type).

This method is general and a more accurate optical potential could be used [71, 72].

Monitoring the instantaneous motion $I(z(t))$ of the bead in the bistable phase, mean residency times $\tau_{1,2}$ and stiffnesses $\kappa_{1,2}$ are extracted from experimental intensity time traces for each well. Kramers rate equations provide the following system fed with the extracted values:

$$\begin{cases} \partial_z^2 U_M(z,\ell)|_{z=z_1} = \kappa_1 & (2.23) \\ \partial_z^2 U_M(z,\ell)|_{z=z_2} = \kappa_2 & (2.24) \\ \dfrac{\sqrt{\kappa_1}\sqrt{\kappa_b}}{2\pi\gamma} \exp\left(-\dfrac{U_M(z_b,\ell) - U_M(z_1,\ell)}{k_B T}\right) = \dfrac{1}{\tau_1} & (2.25) \\ \dfrac{\sqrt{\kappa_2}\sqrt{\kappa_b}}{2\pi\gamma} \exp\left(-\dfrac{U_M(z_b,\ell) - U_M(z_2,\ell)}{k_B T}\right) = \dfrac{1}{\tau_2} & (2.26) \end{cases}$$

where Eqs. (2.25) and (2.26) are escape equations given by Kramers theory in the over-damped regime for each of the metastable states of the bistable phase. Resolution of this system gives access to the remaining unknown quantities of our model: the mirror waist distance ℓ, the bead magnification effect M and the size correction parameter A related to the coupling between the light field and the finite size bead.

The energy difference between the two metastable wells can be derived from the extracted residency times and stiffnesses as

$$\Delta U = k_B T \ln\left(\frac{\tau_1}{\tau_2}\sqrt{\frac{\kappa_1}{\kappa_2}}\right). \quad (2.27)$$

Taking the ratio of equations 2.25 and 2.26 then removes the dependency of the system on the properties of the barrier but requires the knowledge of A. Fixing A and using the simplex algorithm, the external variable ℓ (piston length) and the magnification parameter M are determined. This therefore gives the entire potential $U_M(z,\ell)$ for a given A. Iterating this resolution over A until the rate equations are verified provides the triplet (ℓ, M, A) that best solves the whole system. Once determined in one ℓ-configuration (say the symmetric bistable configuration), the parameter A is then kept constant when solving other bistable configurations (for instance varying ℓ).

Exploiting this strategie, it is the coherent nature of the optical landscape that provides in our experiments a built-in spatial reference. Because the bistable potential is directly formed by the constructive interferences between the incident and reflected beams, the inter-well distance becomes, for a fixed configuration (i.e. fixed mirror-waist distance), a function of only the laser wavelength and the objective NA.

With a proper modeling of the Gaussian beam passing through the objective we are able to extract from the intensity signal parameters that determine uniquely the potential. Auto-correlations of the intensity signal (i.e. related to the PSD) provide trap stiffnesses and therefore the second order derivatives of the potential at the bottom of each well as given by eq. 2.23 and eq. 2.24.

In addition to the stiffnesses, the measure of residence lifetimes (τ_1, τ_2) in each wells leads to determine the energy difference ΔU between the 2 wells, as discussed above and expressed by eq. 2.27. This, together withvalues for the optical parameters (laser wavelength, objective numerical aperture) enables to know the distance between the attractors.

Our original solving approach can reconstruct the interaction potential of the bead for any length of the optical piston, without resorting to any position density probability of the bead along the optical axis. This is an important capacity of our method since it does not require an absolute calibration of the setup.

2.4 POWER SPECTRAL DENSITY

The PSD is exploited to determine the trap stiffness of the bead in each of its wells. To do so, the full time trace, depicted on Fig. 2.7 is cut on the top of the barrier and the dynamic of

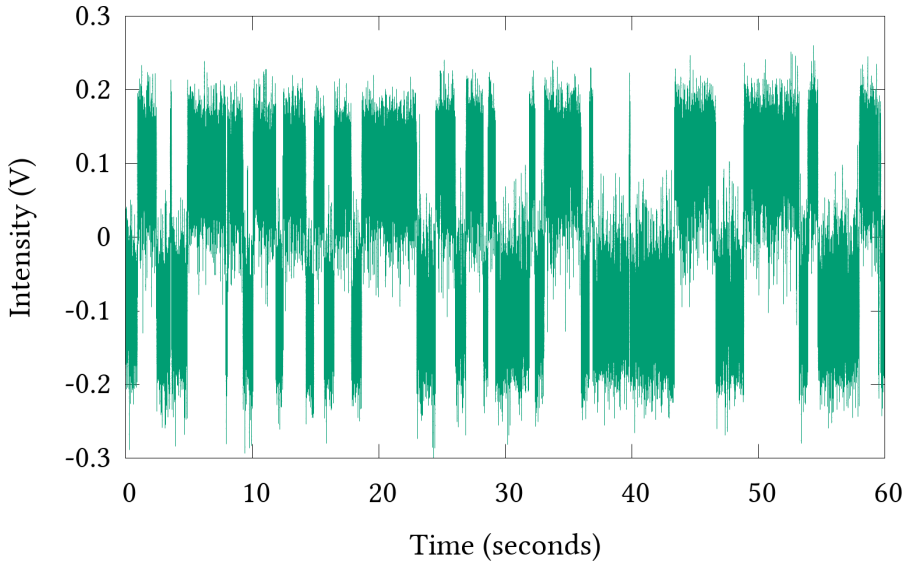

Figure 2.7: Time trace associated with a bistable motion of the bead as recorded by the PIN photodiode on the reflected beam intensity. The acquisition time is set to 60 s, at a rate of 262 kHz.

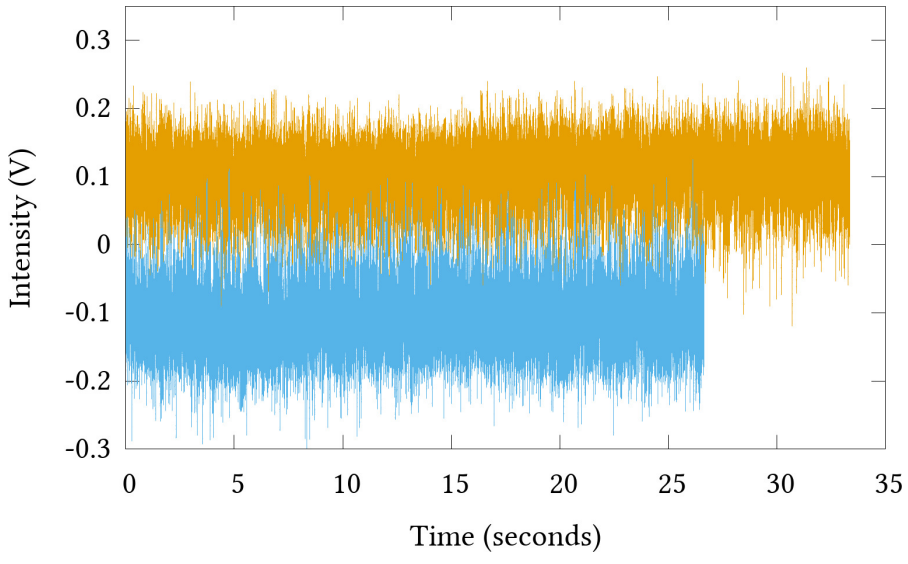

Figure 2.8: Concatenated time traces associated with each of the mean values measured in the time trace of Fig. 2.7.

each side is concatenated forming two new time traces (Fig. 2.8).

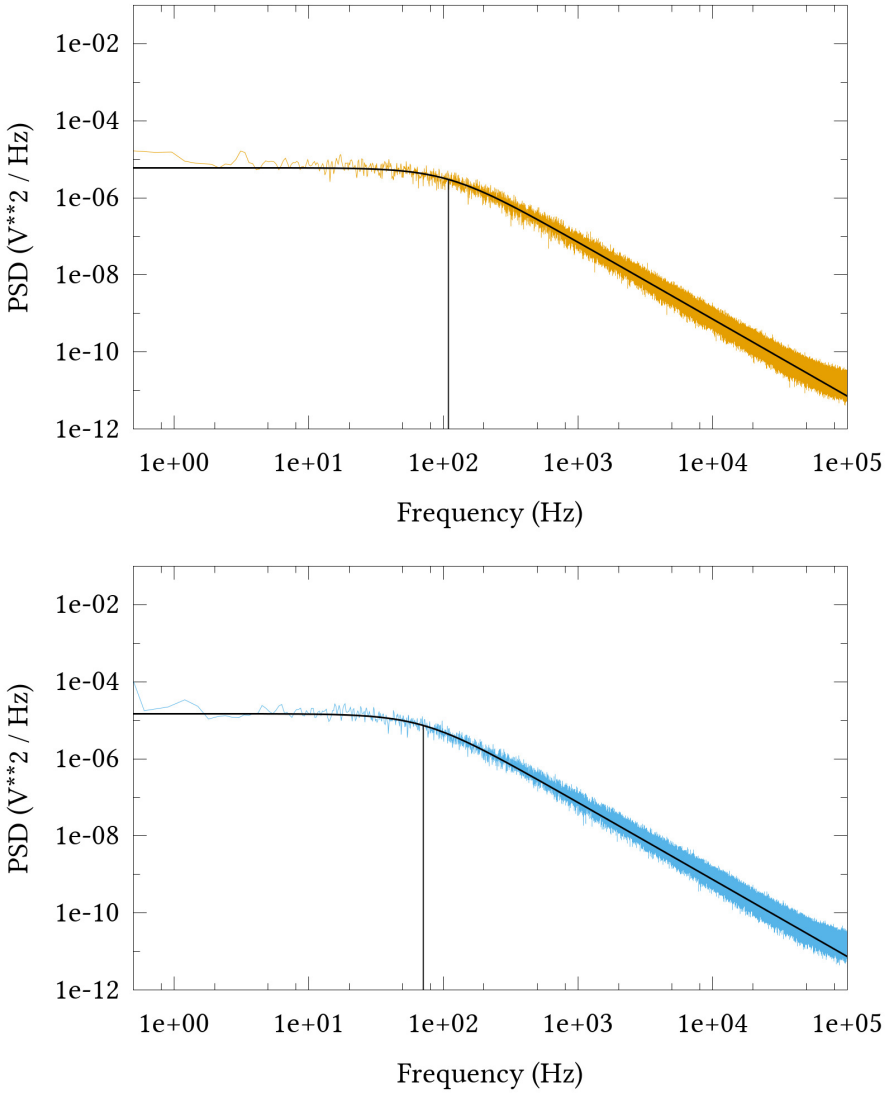

Figure 2.9: PSD taken on each of the concatenated time traces given in Fig. 2.8. Upper curve is the PSD for the $I(t) > 0$ concatenated time trace and the bottom one the PSD of the concatenated time trace when the bead is in the well further away from the mirror (corresponding to $I(t) < 0$). The black solid line is the Lorentzian fit of the data and the vertical line gives the roll-off frequency of each of the quasi-harmonic trap associated with each locally stable positions.

Assuming that the recorded stationary intensity time traces are ergodic, meaning that a time trace is independent of the

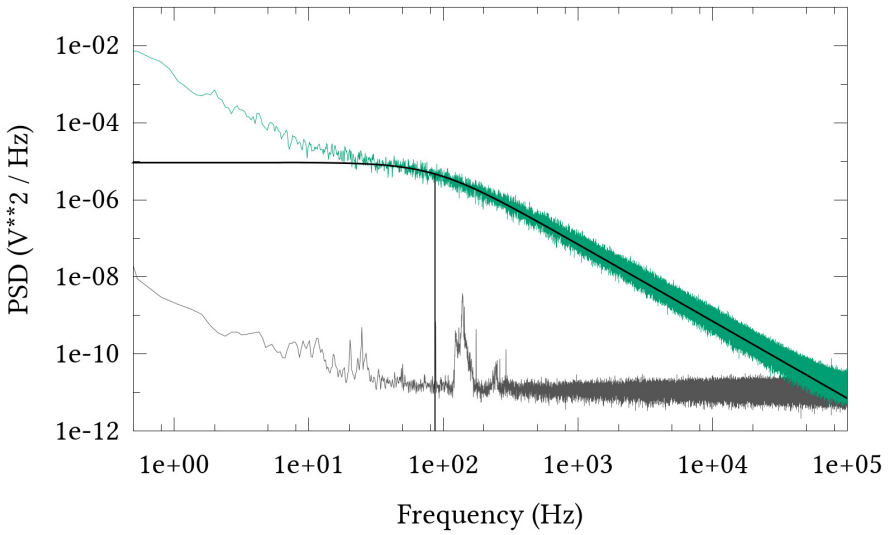

Figure 2.10: PSD taken directly from the full time trace shown in Fig. 2.7 for an acquisition time of a minute. The bottom PSD (dark) corresponds to the experimental noise floor.

initial position of the bead and leads to the same distribution for different realizations with identical parameters, a spectral density analysis can then be performed [73] on each of these trace. The trap stiffness is then directly extracted from this analysis. This standard approach has the advantage of being straightforward to apply on rapidly fluctuating and voluminous data.

It clearly appears that the PSDs associated with the bead motion in each of the attractors, presented as concatenated time traces of Fig. 2.8, follow the typical Lorentzian shape of a Brownian motion performed in an harmonic trap in the over-damped regime. This is shown in Fig. 2.9. The two wells of the bistable potential, separated by the activation barrier, are thus quasi-harmonic, with stiffnesses $\kappa_{1,2} = 2\pi\gamma\, f_{1,2}$ that can be determined directly from the fluid drag γ and the so-called roll-off frequency $f_{1,2}$ of the trap measured on each PSD [61].

In the full PSD signal shown in Fig. 2.10, these quasi-harmonic traps are seen through the Lorentzian fit at high-frequencies and the roll-off frequency is the residency time pondered trap stiffness of each well. But the spectrum within these local wells does not exhaust the bistable dynamics. Low frequencies indeed reveal a strong increase in the power spectrum which is due to the activation process of the bead over the bistable barrier and broadly spread, occurring on a typical

~ 1 Hz regime even though it is not entirely resolved at lower frequencies (this would require longer acquisition times). In other words, the crucial separation of time scales discussed above is readily observed on the PSD associated with the bistable motion of the bead.

The frequency associated to the activation process over the barrier is around 1 Hz, the trap stiffness at 100 Hz and the thermal fluctuations have constant spectral amplitude on the studied region (the PSD tail has a perfect $1/f^2$ decay). It is worth noticing that the activation rate cannot be increased (by decreasing the optical intensity or increasing the thermal noise). This would lead to an overlap between the activation signature and the trap confinement/relaxation processes, breaking the timescale separation criterion.

2.4.1 *Noise floor*

The dark curve on Fig. 2.10 shows the noise floor of the acquired PSD. Shot noise is visible at low frequencies which is small compared to the amplitude of our measurements. The peak slightly above 100 Hz comes from the intensity control loop of the laser. Above this value the spectrum is basically flat, the bottom of the dynamic range of the acquisition card being reached. Throughout our experiments, the noise floor always arises either by reaching the bottom of the dynamical range of the electronics or from the thermal noise. The radiation pressure noise from the laser sources is negligible, as rapidly evaluated.

The energy of a single photon is:

$$E_{photon} = \frac{hc}{\lambda}, \tag{2.28}$$

with h the Planck constant, c the speed of light and λ the light wavelength. It gives in our case an energy of:

$$E_{photon} = \frac{6.62 \cdot 10^{-34}\ 3.00 \cdot 10^{8}}{(785 \cdot 10^{-9})} \tag{2.29}$$

$$= 2.54 \cdot 10^{-19}\ \text{J}. \tag{2.30}$$

For a laser of power $P = 45\text{mW}$, the average number of photons per second $\bar{I}$ is,

$$\begin{aligned}\bar{I} &= P/E_{\text{photon785nm}} && (2.31)\\ &= 45 \cdot 10^{-2}/(2.54 \cdot 10^{-19}) && (2.32)\\ &= 1.78 \cdot 10^{18}. && (2.33)\end{aligned}$$

The coherent laser source has a radiation pressure noise δF_{rad},

$$\begin{aligned}\delta F_{rad} &= 2\frac{h}{\lambda}\sqrt{\bar{I}} && (2.34)\\ &= 2\frac{E}{c}\sqrt{\bar{I}} && (2.35)\\ &= 2\frac{2.54 \cdot 10^{-19}}{3.00 \cdot 10^{8}}\ 1.33 \cdot 10^{9} && (2.36)\\ &= 2.25 \cdot 10^{-3}\ \text{fN}/\sqrt{\text{Hz}}. && (2.37)\end{aligned}$$

This must be compared with the thermal force noise δF_{Th} evaluated from the fluctuation-dissipation theorem as:

$$\begin{aligned}\delta F_{Th} &\simeq \sqrt{2k_b T\gamma} && (2.38)\\ &= \sqrt{2\ \frac{4 \cdot 10^{-21}}{1.0 \cdot 10^{-9}}} && (2.39)\\ &= 2.83\ \text{fN}/\sqrt{\text{Hz}}. && (2.40)\end{aligned}$$

These values imply that a spectral analysis performed on our setup is limited by the thermal fluctuations and not by the laser noise. This justifies well that the intensity monitored is a direct function of the bead dynamics only.

2.5 STATIONARITY AND RESIDENCY PROBABILITY DENSITY

The whole analysis of the bead time traces assumes that the system under study is in a non equilibrium steady-state regime, as seen previously. More precisely, it is assumed that the system, which does not have a single equilibrium position to relax to, keeps the same dynamical rates with time. This assumption is verified by constructing the cumulative evolution C_T of the time τ spent by the bead in each of the (j =up, down) states as

$$C_T(k)^j = \sum_{i=0}^{k} \tau_i^j. \qquad (2.41)$$

Such a construction is presented in figure (2.11) for the previously presented one minute long acquisition. One observes that for each of the up and down states, the evolution is almost linear with time. This means that on average the mean residency time in each state remains the same all through the experiment time. A change of slope in the cumulant evolution would mark the non-stationary character of the system observed over that acquisition time.

That our system is proven to be in a non-equilibrium steady state using such a cumulative construction is important since it allows using spectral analysis in order to treat the signal associated with the instantaneous motion of the bead. It is also clear that the studied system is ergodic: measuring another bead at another time in the same configuration would give the exact same dynamical values because the trapped objects always relaxes to its position around the Gaussian beam waist. The probability density distribution of finding the bead

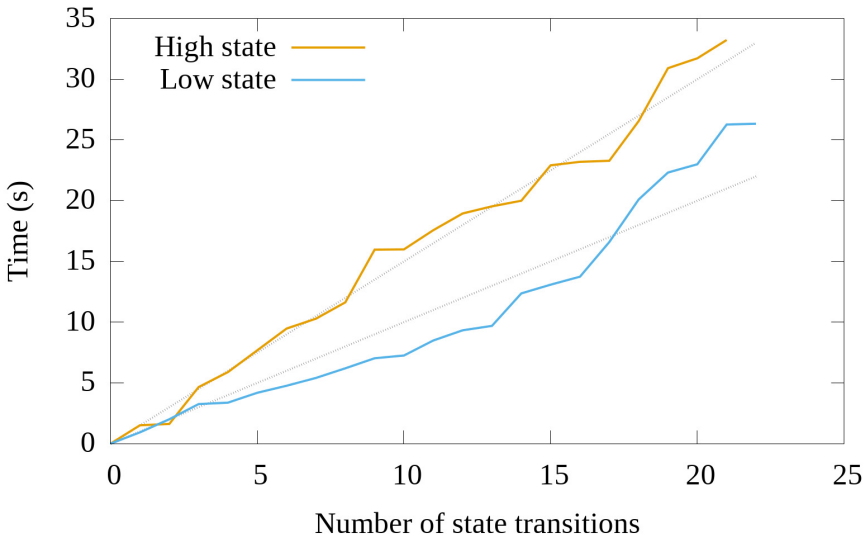

Figure 2.11: Experimental cumulative evolution of the time spent in a given state with "high state" in orange and "low state" in blue. The evolution is almost linear and thus it allows us to say that the system is a non-equilibrium steady-state system.

in state up or down is also constructed from the individual time trace in each of the states and is displayed in Fig. 2.12. $P_{up/down}(\tau) = Prob\{\tau_{up/down} > \tau\}$ quantifies the probability of staying in the same state after some time τ already spent in the state. The probability distribution fits an exponential decay of time constant the mean residency time in each state (to

experimental and fitting inaccuracies), therefore the dynamics of the bead can be considered to follow a Poisson dynamics. On average the bead stays a given time in a well but the knowledge of this residency time gives no hint on the following one. As it is the case for both wells it is equivalent saying that the transition is uncorrelated to the previous one.

2.6 HILBERT PHASE PORTRAITS

Although density probabilities clearly illustrate the time spent by the bead in each well, they provide no hint on the instantaneous dynamics of the motion and in particular on the exact nature of the barrier crossing. In the ballistic regime, a phase space representation displays trajectories that connect all the successive states through which the system evolves in time. In this regime, the phase space is simply built on a (position,momentum) space.

However, the notion of an averaged velocity (and therefore momentum) becomes ill-defined for a diffusive system. The Brownian motion of the bead along the optical axis z is

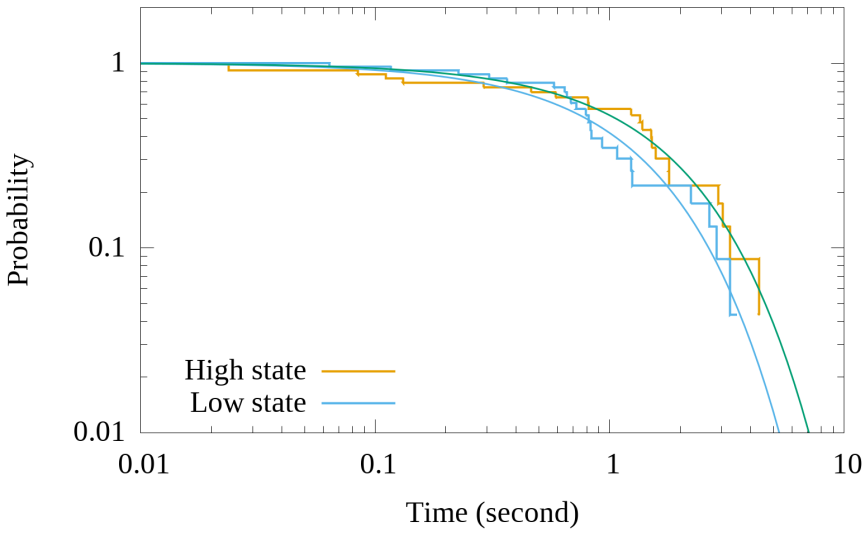

Figure 2.12: Experimental probability of leaving a "state" for the other after a given time already spent within it. The bead is highly confined after arriving in a well and will not diffuse to the other state before a time lag of the order of a second. The shape follows a typical Poisson distribution of time constant equal to the mean residency time.

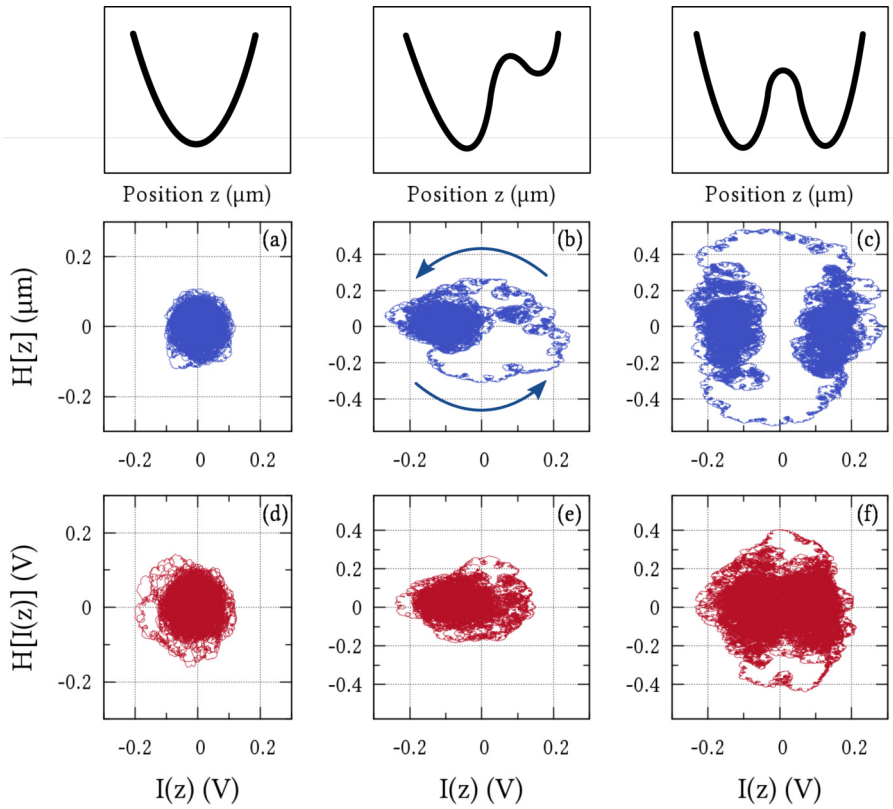

Figure 2.13: Simulated and experimental intensity Hilbert phase space trajectories of the bead dynamics along the optical axis for different mirror positions, i.e, for different energy configurations schematized in the first row. Second long time traces illustrating the typical dynamical of the bead motion for three potential shapes in their Hilbert configuration space. The red curves represent experimental data acquired during the phase transition while blue traces are simulated traces (in meters) of the potential matching the data. Graphs a) and d) represent the stable single well potential like the ℓ_1 position in Fig. 2.4. Figures c) and f) illustrate a typical cycle in a bistable potential ($\ell \sim \ell_2$ from Fig. 2.4) from the lower position to the upper one and coming back to the initial well. We clearly observe both in the data and theoretically that barrier crossing by diffusion involves a big amplitude in the Hilbert component of the signal. Figures b) and e) illustrate the transition between stable and bistable potentials where the bead moves out of its stable well for a very short amount of time.

characterized by a mean square displacement measured over a time t $\langle(\Delta z(t))^2\rangle = 2Dt$ proportional to the diffusion constant D. Defining a mean velocity of the bead over the same time interval as $\bar{v} = \sqrt{\langle(\Delta z(t))^2\rangle}/t$ leads to a $\sim 1/\sqrt{t}$ diverging velocity. This implies that it is not possible to construct a phase space representation that would be independent of the band width chosen for sampling the bead trajectory.

To circumvent this problem, we have implemented the *analytical signal* method well known for processing complex signals, in particular in biological systems [74, 75]. The method consists in forming, for the instantaneous position of the bead $z(t)$, an effective quadrature $\tilde{z}(t) = \mathcal{H}[z(t)]$ based on a Hilbert transform $\mathcal{H}$ of the signal, explicitly calculated as

$$\tilde{z}(t) = \frac{1}{\pi}\int_{-\infty}^{+\infty} d\tau \frac{z(\tau)}{\tau - t}. \tag{2.42}$$

This leads to build the so-called *analytic signal* $Q_z(t) = z(t) + i\,\mathcal{H}[z(t)] = \rho(t)e^{i\varphi(t)}$ which defines in an unique way both the instantaneous amplitude $\rho(t)$ and phase $\varphi(t)$ associated with the bead motion $z(t)$. Our central point is that, contrasting with the standard $(z,\dot{z})$ phase space, the $(z(t),\tilde{z}(t))$ phase *portrait* can still be perfectly defined for a diffusive motion and computed over any chosen bandwidth with the same trajectory patterns.

In the simplest case of a ballistic harmonic motion $z(t) = \rho\cos(\omega t)$, one has $\tilde{z}(t) = \rho\sin(\omega t)$ and the phase portrait draws a mere circle in the $(z(t),\tilde{z}(t)$ coordinates. This is different from the elliptical trajectories in the $(z,\dot{z})$ phase space for the harmonic oscillator.

For 3 different potential configurations -corresponding to the stable and bistable phases and the transition region between them- drawn in panels (a)-(c) of Fig. 2.13, we extract a 1 s-long excerpt of the bead dynamics $z(t)$ data which we Hilbert transform via 2.42. The corresponding phase portraits displayed in panels (d)-(f) are then compared with numerical simulations performed on stochastic Langevin equations with the equivalent potential determined either by resolving the bistable dynamics as detailed above, or by estimating the distance ℓ when the potential configuration is outside the bistability region, such as in the case of panel (a). Importantly, these simulations have been performed with an identical bandwidth as the experimental one. From the simulated $z(t)$ trajectories,

Hilbert transforms are computed together with the phase portraits in panels (g)-(i).

As expected from the Brownian motion in a (quasi-)harmonic well, a Gaussian distribution of positions $z(t)$ should be characterized by a circle in the phase portrait. This is clearly observed both from the experimental and numerical realization of $Q_z(t)$ in Figs. 2.13 (a) and 2.13 (d). Then by construction, the hopping dynamics back and forth between the two local minima and through the barrier of the bistable configuration corresponds to a closed circulation of the bead quadrature. In that bistable phase, the barrier-crossing connects the two attractors following an oriented trajectory at the periphery of the quadrature space.

This *analytical signal* approach enables to directly reveal the diffusive character of the barrier-crossing process. In panel (f), it is even possible to track some recrossing events [69] where the bead, diffusing across the barrier, gets however pushed back into its initial minima by thermal fluctuations. Also, this approach directly leads to a remarkable connection with the amplitude of the Hilbert transform being an increasing function of the activation speed through the barrier (or residency time in the opposite well, since both times are naturally connected in a bistable configuration). Yet, this connection should deserve to be quantitatively discussed in more details.

When evaluating the experimental quadratures $\tilde{z}(t)$, one has to keep in mind, as seen for instance on Fig.2.7, the overlap between the tails of the time-traces of the reflected intensity associated with the diffusion motion of the bead in each potential well. This overlap will necessarily show up in the quadrature representation $Q_z(t)$, as seen in particular Fig. 2.13 (f) where there is no net separation between the two attractors. Comparing simulated and experimental Hilbert transforms on Fig. 2.13, the crossing dynamics that connects the intensity mean values is clear and the overall shapes of the quadrature plots are in good agreement with the simulation. It is indeed an advantage of this method, even when the dynamical signal within both well overlaps, the movement of the bead when crossing the barrier is well resolved and accessible.

Finally, this Hilbert approach has the advantage to allow us discriminating the trajectory sequences associated with intra-well dynamics from trajectories that develop on the barrier as they has stronger amplitude in the quadrature space.

2.7 CONCLUSION

We describe in this chapter our optical piston setup, formed by a Gaussian beam focused in front of a movable mirror. Depending on the position of the mirror with respect to the waist of the Gaussian beam, the interference between the incident and reflected beam can be either constructive or destructive. This gives us the possibility to generate either a strong quasi-harmonic interaction potential or a bistable interaction potential, within which evolves an over-damped Brownian 1 µm polystyrene bead, immersed in water, at room temperature.

With the piston tuned to induce a bistable interaction potential, we study in details the metastable dynamics of the trapped bead, in particular through fluctuating time-traces recorded from the recollected intensity signal that are directly related to the stochastic motion of the bead.

We show how the bistable dynamics of the bead can be described with a two-state model where the bead resides most of the time at two metastable positions in space, with rare hopping events induced by the thermal fluctuations. With metastable states long-lived compared to the intra-well relaxation dynamics, the formalism set up by Kramers can be applied.

We model the interaction potential induced by the optical piston in the dipolar (Rayleigh) regime. By constraining Kramers rate equations with a few dynamical, thus measurable, quantities (i.e. mean residency lifetimes and trap stiffnesses in each of the two metastable wells), we show how such a model can actually be fully resolved, including an effective correction factor accounting for the deviations with respect to a more rigorous Mie-based approach.

We also carefully verify the steady-state nature of the interaction potential. It is important indeed to ensure that the bead, not having a single equilibrium position to relax to, keeps the same dynamical rates with time. This stationarity condition, together with the ergodic character of the dynamics, are necessary when performing power spectral analysis of the bistable regime.

We finally propose a definition of phase portraits appropriate for a stochastic bistable system built on an effective quadrature evaluated from the Hilbert transform of the bead motion. Such phase portraits, displayed for different interaction potential profiles, provide simple illustrations of the dy-

namical evolution of the bead, with a clear separation between intra- and inter-wells dynamics. In particular, recrossing events over the barrier of the potential are perfectly identified.

3

REVERSIBLE COMPRESSION OF THE OPTICAL PISTON

In the previous chapter, the optical piston was described together with the different methods available to us for discussing with a high precision the associated bistable dynamics that an optically trapped bead can probe. In this chapter, we actually operate the piston as a source of mechanical work exerted on the trapped bead. We thus look at the evolution of the interaction potentials as a function of what we will call the piston length ℓ -defined in the previous chapter as the distance between the trapping beam waist and the end-mirror.

In this chapter, we turn this distance as a dynamical external variable in order to induce reversible cross-overs between stable and bistable phases of the over-damped Brownian bead inside the optical piston. With the instantaneous position of the particle being a stochastic process, the position of the mirror controls the piston length ℓ and therefore the optical force field applied to the particle.

We show that the movable mirror injects quasi-statically reversible work into the system (defined as the trapped bead) in the form of Helmholtz free energy. We are able to measure the progressive deformation of the optical potentials exploiting the method based on Kramers' theory described in the previous chapter. This deformation, performed through the incremental displacement of the piston, lead to some reversible heat production. On the experimental time scales that are involved in this work, the reversible piston changes corresponds to an isothermal process. But as expected thermodynamically, the fact that a constant temperature is maintained in the system necessarily implies that some heat is transferred in the process. Interestingly, it is through the optical deformation that we can measure precisely this quantity of heat generated in our experiment.

3.1 AXIAL DISPLACEMENT OF THE PISTON

In this chapter, we now look at our trapping configuration as a system that enables to evolve through different energetic configurations by the external control of the piston length variable ℓ. The experimental setup is the one described in the previous chapter, the bead is first trapped 2 micrometers away from the surface at the ℓ_1 position from Fig. 2.4 and the mirror approaches the waist by infinitesimal steps, compressing the piston. The system is let to relax to its lowest energy configuration after each displacement of the mirror and before an acquisition is started. Only steady state regimes are measured.

3.1.1 *Setup and protocol*

Such a relaxation time is important to insure since it is actually imposed by our detection technique. The trapping beam is also used for the detection of the bead position by measuring the reflected beam intensity. A small displacement of the mirror will change the mean intensity on the PIN photodiode. We want the measured signal to contain on the dynamical signature and centered on zero. It is obtained by waiting 6 seconds before an acquisition after a configuration change, enough to let the high-pass filter (set to 1 second) reject the continuous component of the signal (the mean recollected intensity). Changes at low frequencies or for the continuous component of the signal are filtered out before the start of the next acquisition. The choice of the filter time constant is only chosen by the constraints of our experiment, i.e. a short time between different configurations. The filtered signal is sampled at a frequency much higher than the filter roll-off (262 kHz). The exponential decrease of the signal because of the filter can properly be corrected using the scheme describe in chapter 2, subsection 2.1.6.

Each configuration explored by the bead is sampled for 30 seconds. Even though it may appear short as only about 30 state changes are recorded within a configuration, one has to compose with the experiment stability and drifts as time passes. In this experiment, 10 minutes is the upper time limit considering fluidic drifts from the cell as well as other objects approaching the trapped bead after an initial bead is trapped. The stability of the fluidic cell is around an hour, fluid leakage from the cell or below the spacer changes the optical path length

and thus the repeatability of the experiment. Furthermore, long waiting times decrease the probability of trapping, given the fact that the suspended beads tend to adhere on the surfaces of the walls of the fluidic cell.

3.1.2 *Reversibility / incremental changes of configurations*

An incremental change $d\ell$ of the length of the piston pushes the bead out of equilibrium and forces it to relax in the new $\ell + d\ell$ configuration with a stiffness κ and a fluid friction η on a time $t_D \sim 2\pi\eta/\kappa$ set by diffusion, typically ca. 10^{-2} s in our conditions. Hydrodynamic effects on the bead due to the motion of the mirror can be neglected since the incremental shift of the mirror by $|d\ell| = 20$ nm, performed with a speed V of 1 mm/s set for the piezo-actuator, is associated with a low 10^{-9} Reynolds number [76]. Putting numbers in the computation of the Reynolds number Re yields,

$$\begin{aligned} \mathrm{Re} &= \frac{\rho V d}{\mu} && (3.1)\\ &\simeq 10^{-9}, && (3.2) \end{aligned}$$

with ρ is the fluid density (1000 $\mathrm{kg \cdot m^{-3}}$ for water), μ is the kinematic viscosity (10^{-3} $\mathrm{kg \cdot m^{-1} \cdot s^{-1}}$) and d the diameter of the object (10^{-6} m).

Accordingly, the displacement of the fluid remains purely diffusive and the moving piston therefore has no direct mechanical action on the bead. Under such conditions, the only source of mechanical loss in the system is given by the relaxation process from one configuration to the other.

We emphasize that $z(t)$ does not map the entire canonical equilibrium distribution associated with an ℓ-configuration. It only maps a thermally accessible subset of it, that can be resolved for sufficiently long acquisition times (30 s in our experiment). The notion of stability then corresponds to local stable wells much deeper than k_BT while bistability corresponds to local barrier heights of the order of k_BT over which the bead can be activated. In this picture, stable phases can be identified from bistable phases, as drawn in Fig. 3.5 (a) in the $M - \ell$ parameter space.

3.2 MOTIONAL MAPPING OF INTERACTION POTENTIALS

Brownian trajectories in optical trapping experiments typically last for a few seconds only, or minutes at best. It is therefore clear that the probe bead can only explore a limited amount of space during this finite time and hence a limited region within the entire interaction potential fixed by the optical conditions. The difficulty when studying non trivial potentials is to have a proper mapping by the bead of the energy landscape. It is in fact this mapping that will define the actual interaction potential within which the bead evolves. The term *mapping* is often use to describe the fact that, through its motion, the Brownian object will sample all accessible positions in space such that the probability density of positions is a functions of the potential energy levels via Boltzmann statistics.

The lower energy levels of the potential are obviously more often visited by the bead than higher ones. It is worth noticing that this property for the bead is specific to the overdamped nature of its motion, considering the bath as both the driving and the dissipative medium:

- A lossless bead in the same potential (i.e. the bead without the bath) would indeed only explore one energy level fixed by the initial conditions.
- A lossy but inertial system would never reach levels higher than the initial one.

3.2.1 *Exploring the energy landscape with time*

There is a close relation between the energy landscape characterizing a physical process and the time needed for a system to manifest that process. It is indeed only through the exploration of the energy landscape performed by the system that the given process will be recognized as emergent by the experimentalist. The phenomenon of metastability provides a striking illustration of that connection. Radioactivity for instance, where an excited atom can appear stable on short times and seen to decay on much larger time scales.

Metastability is rooted in the existence of bistable potentials. When aiming at studying experimentally bistable potentials, it is important, as emphasized in [50] (see p. 56), to run the experiment over sufficiently long acquisition times in order to properly map a thermodynamically accessible region

of the whole energy landscape that can characterize the bistable regime. In this situation, it becomes possible to determine accurately the interaction potential through the record of the instantaneous motion of the probe bead.

In order to illustrate the discussion and clarify its meaning, let us consider as an example a bistable potential with very deep wells, separated by a barrier of energy much larger than the thermal energy k_BT. The likelihood for the bead to escape the well at the bottom of which it has been initially confided is very low for a finite experimental time τ_{exp} that is much shorter that the mean escape time τ_{esc} from the well. The recorded signal will hence suggest that the interaction potential trapping the bead is a perfectly single well, harmonic potential. If the second well is not readily accessible to the bead via thermal fluctuations, there can however be bunches of fluctuations that, cumulating on very short time scales, allow the crossing of the barrier. Note that, like tossing 10 successive heads with a coin, the chance for such bunches decreases exponentially with the height of the barrier, in such a way that they become actually extremely rare. While the image of bunches (i.e. trains) is simple indeed, we are mostly confronted to giant fluctuations of a Poissonian nature (the number of coin toss would also change by units of time).

Even then with such occasional bunches, the bead would not have probed sufficiently the potential when aiming at mapping it properly, in particular in the region near the barrier top. Would the barrier height be lower, thermal fluctuations would allow for an exploration of both wells within much shorter times than the whole duration of the experiment and in this case, the barrier would be properly sampled. For a barrier of intermediated height (slightly higher than k_BT set by the thermal fluctuations) a proper sampling is possible and all condition are met to study the bead dynamics through its escape times. As exposed in the previous Chapter, this is precisely where the formalism developed by Kramers is key, allowing to link rigorously residency times with the energy landscape of the bead. In this formalism, for a barrier height of the order of a few k_BT, the so-called escape times correspond to the average residency time the bead, i.e. the time the bead will spend in a well before leaving to the neighboring one by diffusing over the barrier.

3.2.2 *The harmonic regime*

There are no simple expressions characterizing the relation between probed energy levels and the time needed to probe them. But in the case of attractive potentials, taking a simple linear restoring force, it was shown that the time needed to explore higher energy levels of the potential increases exponentially with energy [77]. With respect to our experimental schemes, it is clear that the highest energy levels probed by the bead and driven by the thermal bath can be reached in a reasonably small characteristic experimental time, but that reaching other higher levels is unlikely or requires τ_{exp} so large that it eventually falls outside the time of stability of the experiment itself.

It is possible to give an estimate of this time-energy relation in the case of a bead trapped in a harmonic potential. To this aim, we simply start from the Maxwell-Boltzmann (MB) distribution giving the probability density of reaching an energy ε as $Z^{-1}\exp\left(\frac{-\varepsilon}{k_B T}\right)$ with $Z = \sum_i \exp\left(\frac{-\varepsilon_i}{k_B T}\right)$ the partition function. Our idea is to put this probability in relation with the characteristic time of the trap $\tau_T = \frac{1}{f_T}$ given as the inverse of the roll off frequency of the trap. This frequency is defined by the ratio $\kappa/2\pi\gamma$ between the trap stiffness κ and the Stokes drag γ. Such a frequency is characteristic of the bead dynamics and it separates it into two domains: one at low frequencies $f < f_T$ where the bead motion is confined by the trap, theother one at high frequencies $f > f_T$ where the motion of the bead is a free Brownian motion and the trap becomes transparent to the bead dynamics.

In this harmonic approach, and as presented in the first Chapter, the power spectral density (PSD) $S_z[f]$ of the trapped bead is a simple Lorentzian with

$$S_z[f] = \frac{D}{2\pi^2}\frac{1}{f^2 + f_T^2}, \tag{3.3}$$

with $D = k_B T/\gamma$ the diffusion coefficient.

Our point is to determine how the driving source of energy, namely thermal fluctuations, is distributed across the frequency domain by the modulation of the bead Brownian motion. To do so, we split the position variance, given by the Wiener-Khinchine theorem, over two intervals separated by the roll off frequency of the trap f_T as

$2 \times S_z[f]$ *is the onesided power spectral density.*

$$\begin{aligned}\left\langle \delta z^2 \right\rangle &= 2 \times \int_0^{+\infty} S_z[f]\,df \\ &= 2 \times \left(\int_0^{+f_T} S_z[f]\,df + \int_{+f_T}^{\infty} S_z[f]\,df \right). \end{aligned} \tag{3.4}$$

With a normalized variable $u = f/f_T$, the split variance can be easily computed considering that the primitive function of $\frac{1}{1+u^2}$ is known analytically as $\mathrm{atan}(u) + \mathrm{cst}$ for all real u. The result of the calculation is for the full variance,

$$\left\langle \delta z^2 \right\rangle = \frac{D}{f_T^2 \pi^2} \int_0^{+\infty} \frac{1}{1+u^2}\,du = \frac{D}{f_T^2 2\pi}, \tag{3.5}$$

and for the split variance,

$$\begin{aligned}\left\langle \delta z^2 \right\rangle &= \frac{D}{f_T^2 \pi^2} \left[\int_0^1 \frac{1}{1+u^2}\,du + \int_1^{+\infty} \frac{1}{1+u^2}\,du \right] \\ &= \frac{D}{f_T^2 4\pi} + \frac{D}{f_T^2 4\pi}. \end{aligned} \tag{3.6}$$

This calculation reveals the interesting fact that the position variance of the trapped bead is equally distributed from both sides of f_T. The equipartition argument links the noise power spectrum associated with the variance of the trapped object to the thermal energy via the trap stiffness as $\kappa \left\langle \delta z^2 \right\rangle = \frac{D}{f_T^2 2\pi} = k_B T$. Figure 3.1 provides an illustration of this decomposition. Interpreted through this equipartition argument, our simple analysis therefore leads us to the time-energy relation we were looking for, here that a (mean) energy level $\varepsilon_T = \frac{k_B T}{2}$ is explored by the Brownian system in a time $\tau_T = 1/f_T$.

We now link the characteristic time τ_T with the potential mapping problem, following the spirit of [50]. We use indeed this initial time-energy relation in order to estimate the convergence between the potential probed by the Brownian bead over an experimental time τ_{exp} and the actual equilibrium interaction potential that determines the whole energy landscape of the problem. To this aim, our simple assumption is that the MB probability density for reaching an energy level ε is inversely proportional to the time needed to reach that energy level through thermal diffusion of the bead in the trap, considering an energy ε and a time τ_{exp} larger than the characteristic trap energy ε_T and time τ_T.

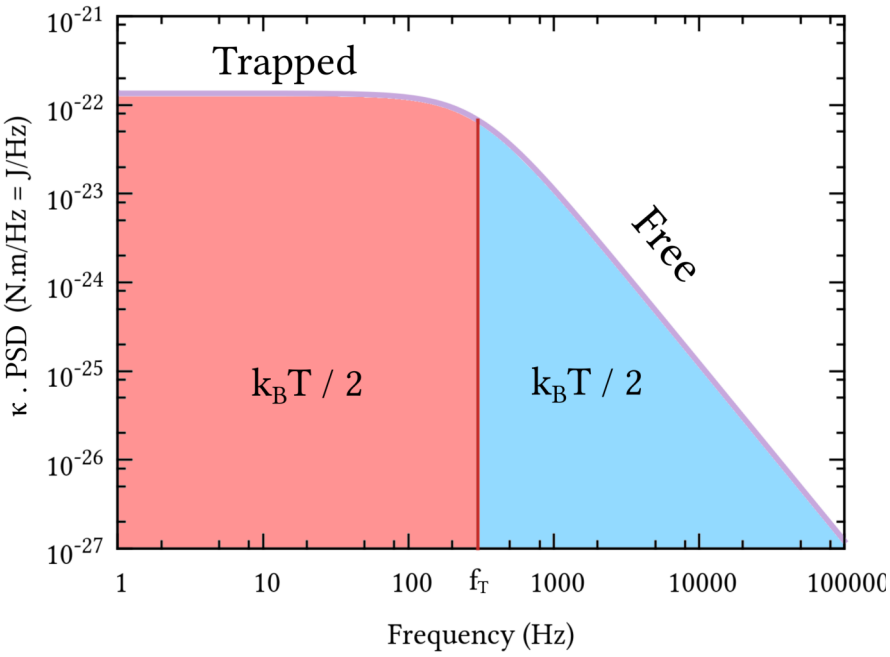

Figure 3.1: Typical power spectral density obtained in our experiments in units of distance multiplied by the trap stiffness. The surface of the colored area is $\frac{k_BT}{2}$. Thermal energy is split equally between the trapped region and the one of free Brownian diffusion.

This idea is in fact related to the mean first escape time problem, which leads to determine the time τ_ε taken on average for the bead to reach a certain position in space (and therefore in energy for an attractive potential) starting from a position near the bottom of the well. Note that a formal derivation of the mean first escape time for a harmonic trap is derived in [77]. The result of this derivation is that the mean first escape time is an exponential function of the energy. Despite the simplicity of our approach, our time-energy based analysis will come to a similar conclusion.

In order to express the statistical relation between time and maximal reached (mean) energy, we write the probability τ_ε as $\tau_\varepsilon = C\ exp(\beta\varepsilon)$, with C a constant independent of τ_ε -but depending on the interaction potential. If we compare two times τ_ε and $\tau_{\varepsilon'}$ within the same potential, the ratio between them is directly computed as $\frac{\tau_\varepsilon}{\tau_{\varepsilon'}} = exp(\beta(\varepsilon - \varepsilon'))$, where all constant factors compensate because we work within the exact same potential.

From the above analysis, the harmonicity of the optical trap precisely yields a connection between the relaxation time

τ_T and the mean diffusion energy ε_T. This allows us looking at energy levels $\varepsilon = n\varepsilon_T$ given as multiples of $\varepsilon_T = {}^{k_B T}/_2$. Reporting these relations yields a simple scaling for the time ratio as

$$\frac{\tau_{n\varepsilon_T}}{\tau_{\varepsilon_T}} = exp\left((\beta(n\varepsilon_T - \varepsilon_T)\right) \tag{3.7}$$

$$= exp\left((\beta\varepsilon_T(n-1)\right) \tag{3.8}$$

$$= exp\left(\frac{(n-1)}{2}\right). \tag{3.9}$$

This clearly reveals that reaching higher energy levels has an exponential cost in time. As an example, we consider an harmonic optical trap of stiffness of 200 Hz, typical of our experiments, and characterized by a relaxation time $\tau_T \sim 5$ ms. In such conditions, the mean first escape time needed to reach an energy level of $4 \times k_B T$ is almost $35 \times \tau_T$ (i.e. ca. 200 ms). This value is precisely of the same order as the time measured in our experiment.

This relation also gives the evolution of the mean highest energy level that can be reached by the diffusive bead as a function of time. Starting from $\frac{\tau_\varepsilon}{\tau_{\varepsilon_T}} = exp(\beta(\varepsilon - \varepsilon_T))$ and now writing τ_ε as a multiple of τ_T gives $\frac{n\tau_{\varepsilon_T}}{\tau_{\varepsilon_T}} = exp(\beta(\varepsilon - \varepsilon_T))$ which can be solved for ε. The solution writes as

$$\varepsilon = \beta^{-1} log(n) + \varepsilon_T \tag{3.10}$$

$$= k_B T\left(log(n) + \frac{1}{2}\right) \tag{3.11}$$

$$\simeq k_B T log(1.65\, n). \tag{3.12}$$

This relation is plotted on Fig. 3.2 in normalized units of $k_B T$. It is an affine function on a semi-log scale. The slope is of $2.3 k_B T$ per decade meaning that, in an experiment, exploring roughly 2 additional quanta of $k_B T$ requires $10\times$ more time than what has been already spent to reach a targeted maximal level of mean energy. It is worth emphasizing again as in Section 3.2 that because of the overdamped nature of the dynamics of the bead with a thermal driving bath, all energy levels are explored, up to the highest ones.

Finally, we emphasize that our analysis only works on average, for experiments which are conceived as multiple runs with identical initial positions. In this framework, the possibility for a rare event to occur more quickly than on average does

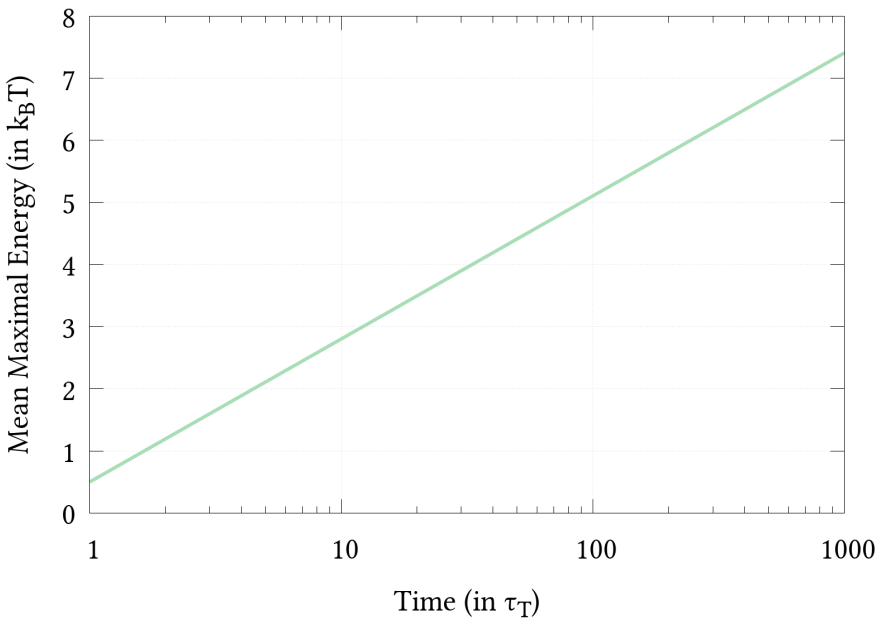

Figure 3.2: Graphical representation of eq. (3.12) in a semi-log scale. The energy is expressed in units of thermal energy k_BT and the time is a multiple of τ_t, the characteristic time of the trapped object. The slope is of $2.3k_BT$ per decade meaning that in an experiment, exploring roughly 2 more k_BT requires 10 $\times$the time already spent to reach the current mean maximal level.

exist, but is not sufficient to characterize the dynamics which is essentially determined by mean time and mean energy values.

3.3 THE CROSS-OVER

Our coherent optical piston configuration gives a unique capacity in monitoring the cross-over between these phases. Indeed, a continuous compression of the piston connecting two stable configurations forces the bead to go through a whole phase of bistability, starting for a piston length ℓ_i with the bead in an initial stable position at the incident waist $z = 0$ and ending for $\ell_f < \ell_i$ with the bead in the very same spatial position but within a different stable potential.

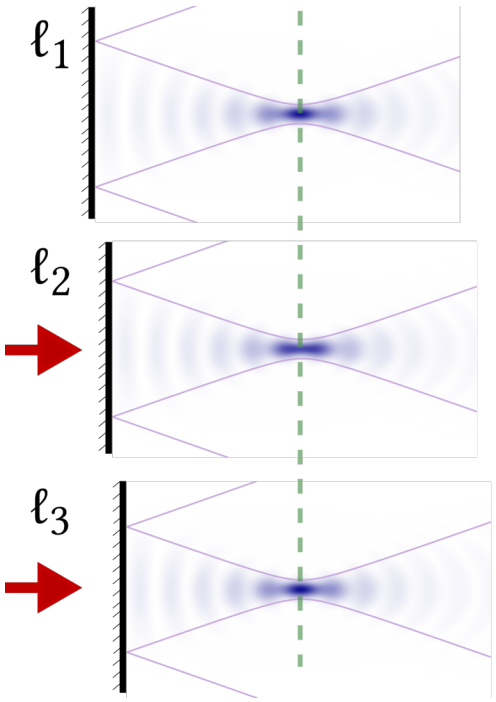

Figure 3.3: Transverse view of the fields intensity along the optical for 3 different mirror positions ℓ. The piston is compressed, starting from a stable position ℓ_1 up to position ℓ_3 crossing through the bistable position ℓ_2.

3.3.1 *Parameter space and trajectories from both sides of the cross-over*

From our resolution method, the bistable dynamics of the bead can be solved for each step in ℓ in a dedicated parameter space (M, ℓ, A). These parameters fix each potential throughout the bistable phase from which they are extracted. The actual steps of the entire path followed by the system between ℓ_i and ℓ_f can be plotted in the $M - \ell$ plane. It is worth noting that the resolved ℓ values follow precisely the mirror actuation command and that the path shows only a small dispersion in M values. This important an outcome of the analysis: it gives the possibility to determine the potential profiles even in the stable phase from a simple extrapolation on the variable ℓ. This is done for instance for the stable ℓ_1-configuration of Fig. 2.4 with the measured potential profile plotted in Fig. 2.5 (b).

As shown in Fig. 3.5 (b), the path can also be represented through intensity probability densities calculated from the evolution of the reflected intensity of the trapping beam as a func-

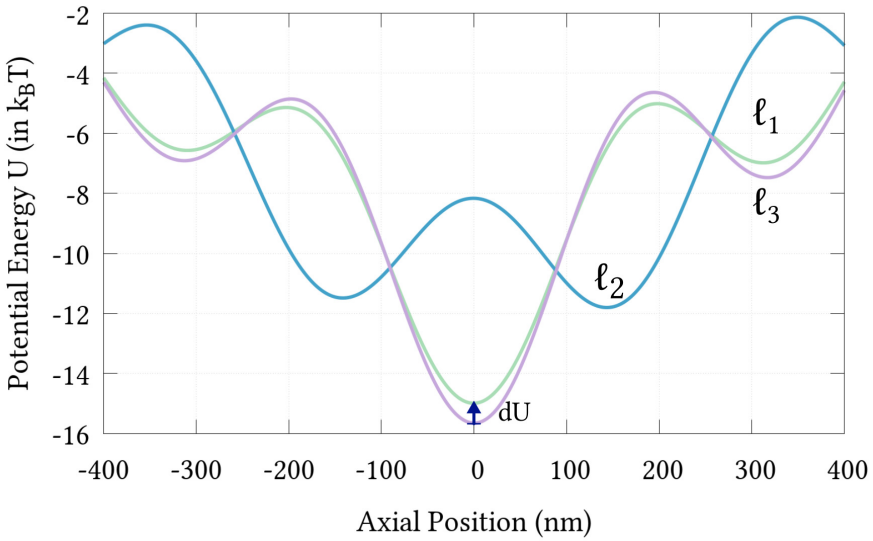

Figure 3.4: Trapping potential energy the bead evolves within for 3 different positions of the cross-over. The first curve in green corresponds to the initial position of the cross-over, the ℓ_1 position from Fig. 2.4 (b) with minimal energy position at the beam waist. The blue curve is the ℓ_2 position from Fig. 2.4 (b), the potential has local minima at both sides of the waist, the dynamic is bistable. The purple curve ends the cross-over, the piston is compressed over an inter fringe and the bead comes back to a stable single welled potential at the beam waist (mirror position ℓ_3). It is worth noticing that over the cross-over and although the bead comes back to its same spatial position, the potential energy changes. Optical field illustrating these positions are given on Fig. 3.3.

tion of ℓ. These densities link each probability density extrema to a local minima (a local well) of the resolved potentials. These plots clearly reveal the progressive onset of a bistable dynamics of the bead along the optical axis of the setup.

We want to stress here a clear advantage of our statistical method: this cross-over dynamics can be probed with a high precision, despite the unknown exact relation between the measured intensities and the bead positions along the optical axis.

In standard treatments [8, 78] the interaction potential $V(z)$ is recovered from the probability density of position $p(z)$ of the trapped bead from a MB distribution approach as

$$V(z) \sim -k_B T \cdot \log(p(z)) \tag{3.13}$$

when the bead is observed for a sufficiently long time, leading to well-defined position histograms. This method assumes however:

- that each configuration is at thermal equilibrium
- that the bead dynamics is sufficiently well sampled in order to properly map its successive positions in space
- that the bead position is properly calibrated in space throughout the whole accessible positions of the bead in the fluid

This last assumption turns out to be crucial but it is inoperative within our framework. This comes from the very specific detection scheme we use in our experiments that was described in Ch. 2. This schemes leads to an overlap between the temporal dynamics of the bead in each local well with intensity levels that are equal to the intensity signal related to the events associated with the barrier crossing. This typical overlap is clearly seen when looking back at the Hilbert phase portrait representation of the bistable configuration displayed in Fig. 2.13 (c) and (f). Due to this overlap, the approach of Eq. (3.13) cannot give neither the correct waist-mirror separation distance ℓ corresponding to the interaction potential of the experiment, nor the correct barrier height.

In fact, and as already discussed in Ch. 2, section 2.3, we do not measure in our experiments any distance from intensity histograms but the spatial calibration is obtained through the resolution of our complex potential, exploiting its coherent nature which sets the interference fringe as a natural meter of the problem.

After the interaction potentials are solved in the bistable region giving parameters A, M and ℓ_1 it becomes straightforward to illustrate the potential evolution as a function of the mirror position ℓ. Such a representation is given on Fig. 3.4 where the potential energy $U(z,\ell)$ is given for 3 difference mirror positions, ℓ_1, ℓ_2 and ℓ_3 corresponding to the start of the cross-over, a compression of the piston half way through the

cycle and the end of the compression respectively. At the initial piston position, the bead spends most of its time at the waist as it is the potential minimum. This potential is represented by the green curve on Fig. 3.4. By compressing the piston the bead is then pushed backward behind the waist and another metastable position emerges in front of the waist. This emerging well is explored as soon as the bead can be thermally activated over the induced barrier. The blue curve on Fig. 3.4 depicts the potential for a compression halfway through the cycle. At this position of the piston, the bead explores both metastable wells and its dynamic is clearly bistable, as illustrated on Fig. 2.5 (c). Here, both wells are populated and the bead is activated over the barrier sufficiently often in order to properly characterize the bistable configuration. Finally, once the cycle has been completed, the bead reaches its equilibrium position back at the waist of the trapping beam. The associated potential is presented in purple on Fig. 3.4. It is worth noting that while the minima of the initial and final position match, their energy slightly differ. This difference is a clear indication that some of the work injected in the system by the compression of the piston is consumed as a potential energy difference. In the next section, a precise thermodynamic analysis of this compression process is given where the associated thermodynamical quantities are derived and evaluated.

3.4 THERMODYNAMIC QUANTITIES : WORK, HEAT AND ENERGY

It is possible to give a thermodynamic description of the path from an incremental energy balance point of view. This is at the core of the field of *Stochastic Energetics* [50]. Following this approach, the thermodynamic description of our system can be drawn from the Langevin equation describing the over-damped motion of the bead inside the optical piston where

$$\gamma \dot{z} = -\partial_z U_M(z,\ell) + F_{Th}, \tag{3.14}$$

with γ the viscous Stokes drag, $U_M(z,\ell)$ the internal energy and F_{Th} the random thermal force.

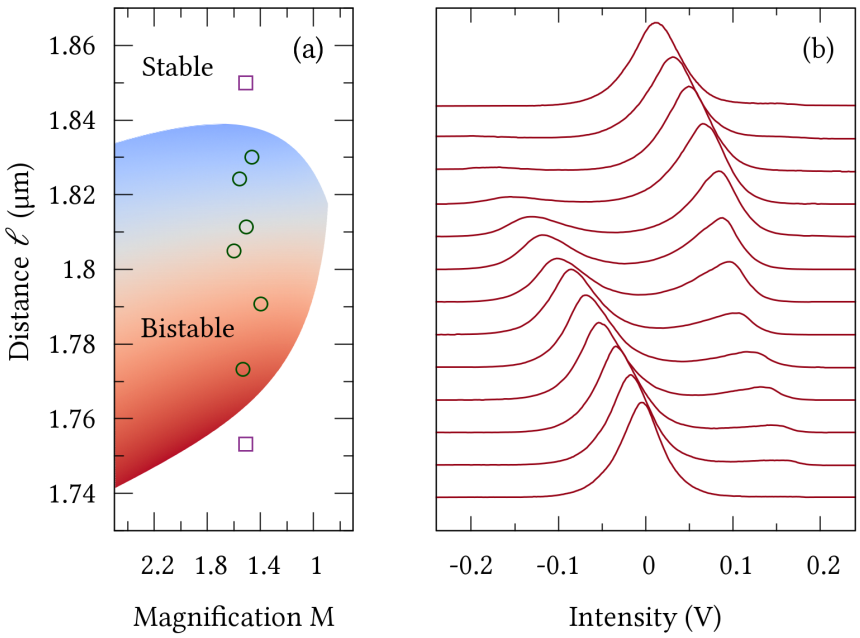

Figure 3.5: (a) Regions of stability and bistability in the $\ell - M$ parameter space. Experimentally solved bistable configurations are displayed in open circles as ℓ is varied. The points in the stable region (open squares) are extrapolated from the extreme bistable points according to the 20 nm piezo-actuation. The color map in the bistable phase codes the asymmetry of the bistable potential as $\Delta U/(U_M(z_1,\ell) + U_M(z_2,\ell))$ positive in red, negative in blue. (b) Intensity probability densities (for 30 s acquisition) as the mirror distance ℓ is reduced, crossing over the bistability region between two stable bead dynamics. The six central bistable plots correspond to the six open circles plotted in (a).

3.4.1 *Defining heat for a single dynamical realization*

Heat represents a quantity of energy that is transferred from a system to its surrounding environment in a different way than work is. Heat -usually denoted dQ- expresses an exchange of energy between two systems and is not a state function of the system, in contrast with the internal energy U. The standard example describing the process of heat exchange consists of two separated bath at different temperatures that are mixed together: particle exchanges of both baths will occur such that, through mechanical diffusion of the constituents of each

bath and collisions between them, the bath now shared by both initial systems will have, at equilibrium, a single temperature in between the two initial ones (pondered by the ratio of fluid volume for each initial bath).

In the case of a single microscopic object immersed in a fluid at equilibrium, defining the heat is more challenging. For macroscopic objects the notion of temperature is directly accessible by, for example, touching the object (i.e. an ice block). In the microscopic world, it is apparent that it is the jiggling motion of the fluid molecules that will define the temperature of the system. Considering a Brownian particle in thermalized bath, the motion of the particle is driven by the colliding particles of the fluctuating bath, giving to the large particle its momentum. This newly acquired momentum is then given back to the bath by friction via the term $-\gamma\frac{dz}{dt}$. Microscopically, the particle collides with bath particles moving in opposite direction transferring its momentum and therefore being slowed down. Both friction and random fluctuating forces have on average a zero contribution on the Brownian particle.

The work done by the particle on the thermal bath on a small displacement change $dz(t)$ is $-\left(-\gamma\frac{dz}{dt}+F_{Th}(t)\right)dz(t)$ where the sign convention stems from the action/reaction principle: the force $-\gamma\frac{dz}{dt}+F_{Th}(t)$ exerted by the bath on the particle is the opposite of the force that the particle exerts on the bath. As it is clear that from the environment standpoint, an energy of $(-\gamma\frac{dz}{dt}+F_{Th}(t))dz(t)$ is transferred from the bath to the system. This energy lost to the Brownian particle is defined as heat $dQ = (-\gamma\frac{dz}{dt}+F_{Th}(t))dz(t)$. A positive heat exchange $dQ > 0$ means that energy is received by the system from environment. Again, it is the law of action and reaction allows us to identify this term as an energy transfer, despite the fact that the microscopic motion of the thermal environment is not explicitly expressed in the Langevin equation.

This is summarized on Fig. (3.6) illustrating the interplay between the change of internal energy dE of our system, the Brownian object optically trapped. In our case the energy dE is only potential energy dU, the bead has no internal degrees of freedom. Heat, as discussed above, comes from exchanges with the bath and work is injected in the system through the compression of the piston, our external parameter.

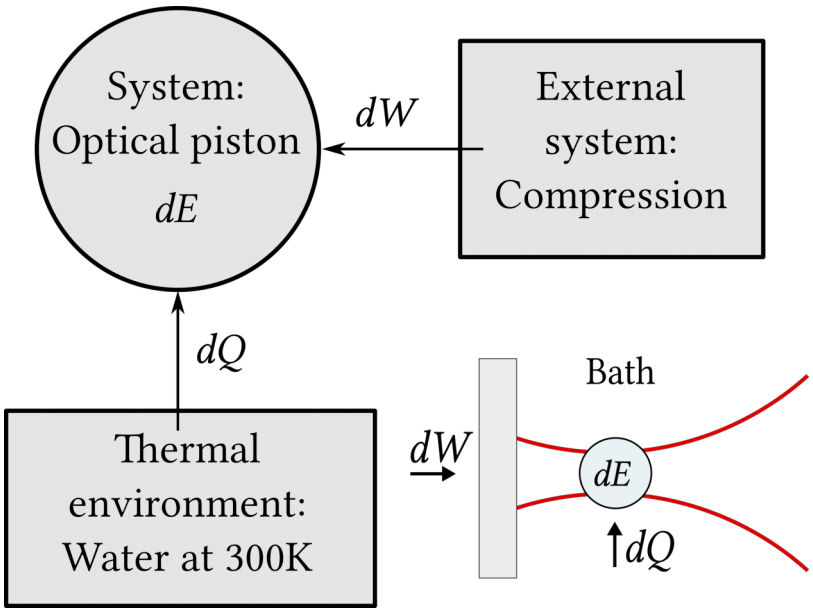

Figure 3.6: Diagram depicting the energy balance between the internal energy δE, the heat δQ and the work δW. Adapted from [50] (page 139).

In order to study the interplay between these quantities the Langevin equation is multiplied by dz and adding $\partial_\ell U_M(z,\ell)d\ell$ yields a *first principle* relation

$$dU_M(z,\ell) = dQ + \partial_\ell U_M(z,\ell)d\ell, \tag{3.15}$$

with $dU_M(z,\ell) = \partial_z U_M(z,\ell)dz + \partial_\ell U_M(z,\ell)d\ell$ and $dQ = F_{Th}dz - \gamma\frac{dz}{dt}dz$. Compressing the mirror provides a change in $dU_M(z,\ell)$, the potential energy of the bead. It is illustrated on Fig. 3.4 by the blue arrow when integrated over a cross-over cycle. This change comes from two sources: *(i)* the heat balance $dQ = F_{Th}dz - \gamma\dot{z}dz$ between fluctuation (determined by a thermal stochastic force F_{Th}) and friction (related to γ), and *(ii)* the external work $dW = \partial_\ell U_M(z,\ell)d\ell$ done on the bead by the displacement of the piston where the external variable ℓ controls the evolution of the potential configurations.

By waiting over time much longer than t_D between each incremental change $d\ell$, the steady-state of every new configuration is reached through mechanical relaxation of the bead. This insures that the system evolves through the configurations in an isothermal and quasi-static way. Moreover, all incremental changes in the optical potential are kept smaller than k_BT. This implies that the bead would go back exploring the same configurations if the displacement of the piston would be

reversed. As a consequence, the whole path in Fig. 3.5 is thermodynamically reversible.

Under such conditions, the averaged external work is directly related to the Helmholtz free energy with [79, 80]

$$\langle \partial_\ell U_M(z,\ell)\rangle_{\{z\}} d\ell = dF(\ell). \tag{3.16}$$

The averaging process is performed over the positions occupied by the bead in the given configuration. The free energy is then only function of the external variable ℓ.

The total amount of work performed by the piston through the isothermal reversible process is directly given by the free energy difference between the initial ℓ_i and final ℓ_f positions of the piston which can be calculated from the (ℓ_i, ℓ_f) canonical partition functions as

$$W = F(\ell_f) - F(\ell_i) = -k_B T \ln\left[\frac{Z(\ell_f)}{Z(\ell_i)}\right]. \tag{3.17}$$

For both initial and final stable configurations, the partition functions can be expanded to second order around the waist. Starting from the partition function

$$Z(\ell_{i,f}) = \int_{-\infty}^{+\infty} \exp\left(-\frac{U_M(z,\ell_{i,f})}{k_B T}\right) dz \tag{3.18}$$

the potential is expanded around its minimum at $z = 0$. Because the force is null at the bottom of the stable well, it has the expression $U_M(z,\ell) = U_M(z=0,\ell) + \frac{1}{2}\left(\partial_z^2 U_M(z,\ell)|_{z=0}\right) z^2 + o(z^2)$ and introducing $\kappa_{i,f} = \partial_z^2 U_M(z,\ell_{i,f})|_{z=0}$ the stiffnesses of the (ℓ_i, ℓ_f) stable potentials the partition function becomes

$$Z(\ell_{i,f}) \simeq \exp\left(-\frac{U_M(z=0,\ell_{i,f})}{k_B T}\right) \int_{-\infty}^{+\infty} \exp\left(-\frac{\frac{1}{2}\left(\partial_z^2 U_M(z,\ell_{i,f})|_{z=0}\right)}{k_B T}\right) dz \tag{3.19}$$

$$= Z(\ell_{i,f}) \simeq e^{-\frac{U_M(0,\ell_{i,f})}{k_B T}} \cdot \sqrt{\frac{2\pi k_B T}{\kappa_{i,f}}}. \tag{3.20}$$

These approximate expressions are then replaced in the expression of the work

$$W = -k_B T \ln\left[\frac{Z(\ell_f)}{Z(\ell_i)}\right] \tag{3.21}$$

$$= -k_B T \ln\left[\frac{e^{-\frac{U_M(0,\ell_f)}{k_B T}}\sqrt{\frac{2\pi k_B T}{\kappa_f}}}{e^{-\frac{U_M(0,\ell_i)}{k_B T}}\sqrt{\frac{2\pi k_B T}{\kappa_i}}}\right] \tag{3.22}$$

$$= U_M(z=0,\ell_f) - U_M(z=0,\ell_i) - k_B T \log\left[\sqrt{\frac{\kappa_i}{\kappa_f}}\right] \tag{3.23}$$

so that the total energy balance writes $\Delta U_M = W + Q_{rev}$ with

$$\begin{aligned} \Delta U_M &= U_M(0,\ell_f) - U_M(0,\ell_i) \\ Q_{rev} &= k_B T \ln\left[\sqrt{\frac{\kappa_i}{\kappa_f}}\right]. \end{aligned} \tag{3.24}$$

This balance connects, along the path, the total amount of energy change ΔU_M to the heat Q_{rev} produced by the whole reversible process. For the cross-over of Fig. 3.5, $\Delta U_M = (-6.41 + 6.176) \times 10^{-20} = -2.34 \times 10^{-21}$ J ($\pm 3\%$). As clearly seen, a stiffness difference between the initial ℓ_i and final ℓ_f configurations is directly related to the production of heat. We unambiguously calculate a quantity of reversible heat $Q_{rev} = -2.48 \times 10^{-22}$ J ($\pm 10\%$) transferred to the fluid by the bead along the path.

The negative Q_{rev} value means that friction dominates over fluctuation as the source of heat. This is consistent with the fact that the bead is displaced from an initial stable ℓ_i-configuration to a final ℓ_f one which is optically more confined. The small Q_{rev} value quantifies the deviation from adiabaticity with $W > \Delta U_M$. This deviation stems from the mechanical deformation of the interaction potential at both ends of the path which is due to an increase in the optical intensity as the mirror gets closer to the waist.

The cross-over study is performed here in a reversible and isothermal way. Usually, in order to maintain the temperature throughout the process, a certain quantity of heat must be generated. In our situation, the heat is actually measured from the optical deformation of the potentials from the initial to the final stable phases of the entire cross-over. In essence therefore, our optical piston configuration enables to control the source of heat. This could lead to the possibility to reach adiabaticity

with $W = \Delta U_M$ in a simple way, with consequences in terms of effective temperature of the system yet to be explored. For instance, in a pure standing wave configuration, both ends of the path have identical trapping stiffnesses leading to $Q_{rev} = 0$. In this context, tailoring the optical landscape is particularly appealing. It leads to the possibility to induce and probe all kinds of thermodynamic processes through the control of both heat production and potential energy differences. Because these quantities are optically determined, the level of control available is expected to be much smaller than $k_B T$.

3.4.2 *Measurement uncertainties and high spatial resolution*

This section explicits the method used to determine the measurement uncertainties associated with the different thermodynamical quantities, in particular the free energy and the heat exchange, through the propagation of experimental uncertainties.

We assume that the distribution of the measured residency times are Poissonian, implying that their mean values $\tau_{1,2}$ equal their variances $\sigma_{\tau_{1,2}}$. Measuring a given $N = 25$ number of back and forth activations of the bead through the barrier (over an acquisition time of $T = 30$ s) for the bistable configurations described in the main text, leads to an experimental uncertainty in the $\tau_{1,2}$ determination of $\delta\tau_{1,2} = \sigma_{\tau_{1,2}}/\sqrt{N} = 0.2\ \sigma_{\tau_{1,2}}$. Because the signal is stationary (see Chapter 2 for a detailed discussion), $\tau_1 + \tau_2 = \frac{T}{N}$ and therefore $\tau_2 = \frac{T}{N} - \tau_1$.

In addition, by taking the expression of the perpendicular viscosity [33] and its derivative, and neglecting the systematic error in the region where the bead evolves, the uncertainty in the change of viscosity along the displacement of the bead can be estimated at a 3% level over 300 nm bed displacement. To this uncertainty, 1 % is added from the extraction of the roll-off frequency at the level of the PSD coming from the fit uncertainty. These uncertainties leads to a global stiffness uncertainty of about $\delta\kappa_{1,2} = 0.04\ \kappa_{1,2}$.

The 6 resolved M values have mean and sample deviation respectively of $\overline{M} = 1.508$ and $\sigma_M = 0.071$. The uncertainty therefore is $\delta M = \sigma_M/\sqrt{6} = 0.029$ and $M = \overline{M} \pm \delta M = 1.508 \pm 0.029$ which is an uncertainty of 4% of the value.

These uncertainties are propagated [81] to determine the uncertainty on ΔU used as an input (through $\kappa_{1,2}$ and $\tau_{1,2}$)

in our system solver. Propagation of $\delta\tau_1$ and $\delta\kappa_{1,2}$ in ΔU in bistable configurations where $\tau_1 \sim \tau_2$ lead to

$$\begin{aligned}
&\left(\frac{\delta\Delta U}{k_B T}\right)^2 = \\
&\left(\frac{\partial\Delta U}{\partial\tau_1}\right)^2 (\delta\tau_1)^2 + \left(\frac{\partial\Delta U}{\partial\kappa_1}\right)^2 (\delta\kappa_1)^2 + \left(\frac{\partial\Delta U}{\partial\kappa_2}\right)^2 (\delta\kappa_2)^2 \\
&= (0.2)^2 \left(1 + \frac{\tau_1^2}{\tau_2^2} + 2\frac{\tau_1}{\tau_2}\right) + \left(\frac{0.04}{2}\right)^2 + \left(\frac{0.04}{2}\right)^2 \\
&\simeq 0.16.
\end{aligned}$$

Remarkably, because the propagation of uncertainties is logarithmic for $\delta\Delta U$, resolution of energy differences between the two well is lower than half a $k_B T$ despite the uncertainty on average lifetimes.

Taking $M = \overline{M}$ (given the small δM value) allows us computing the sensitivity of ΔU as a function of ℓ. The computation yields $\partial\Delta U/\partial\ell = 0.07\ k_B T \cdot nm^{-1}$. Combining this sensitivity with the uncertainty $\delta\Delta U$ of $0.4\ k_B T$ gives an uncertainty on the waist-mirror position $\delta\ell$ of 6 nm only. We can highlight this rather high spatial resolution as an interesting by-product of our approach.

The reversible heat measured with our method on our experimental configuration through the cross-over path (see main text) is computed from trap stiffnesses which depend on the waist-mirror distance ℓ. The measured heat uncertainty δQ_{rev} produced along the path is thus estimated from the determination of $\delta\ell$. The trap stiffness of the stable positions (around $z = 0$) is computed for an incremental displacement of ℓ of $\pm\delta\ell$. A worse-case scenario is then followed, taking the highest differences in trap stiffnesses between $\kappa(\ell)$ and $\kappa(\ell + \delta\ell)$. The heat uncertainty can then be computed as $\delta Q_{rev} = \left| k_B T \ln\left[\sqrt{\kappa(\ell)/\kappa(\ell+\delta\ell)}\right]\right| \simeq 2.2 \times 10^{-23}$ J with $\kappa(\ell) = 6.47 \times 10^{-6}\ N \cdot m^{-1}$ and $\kappa(\ell + \delta\ell) = 6.40 \times 10^{-6}\ N \cdot m^{-1}$. Similarly, the worse-case uncertainty for the potential energy $\delta\Delta U_M = U_M(0, \ell+\delta\ell) - U_M(0,\ell)$ is determined and is about 6×10^{-23} J that can be compared with $k_B T = 4 \times 10^{-21}$ J at room temperature.

3.5 CONCLUSION

In this chapter, the piston length becomes a dynamical parameter that enables the incremental deformation of the interaction potential. After each displacement of the end-mirror of the piston, the bead is let to relax in the newly formed potential.

Using the resolution method exposed in the previous Chapter, we solve the bistable interaction potential at each increment of the piston length. The resolution of the potential parameters in the bistable region gives us access to the potential in the nearby stable regions.

We then monitor the cross-over between regions of stability and bistability, simply by compressing the optical piston through a whole phase of bistability. This leads to study in details the progressive onset of dynamical bistability. Remarkably, while the positions of the minima in the stable potentials match on the optical axis at both ends of the compression cycle, their energy differ. This difference in energy clearly indicate that some work is injected in the system (the trapped bead) by the compression of the piston.

This is taking us to a thermodynamic interpretation of the results:

- from the progressive deformation of the potential we draw an energy-time relation between the energy landscape defined by the interaction potential and the time needed for the bead to map the potential through its stochastic motion. Our analysis gives a simple estimation for the convergence between the region of the potential probed by the Brownian bead over a given experimental time and the actual equilibrium interaction potential determining the entire energy landscape of the problem.

- from a thermodynamic description of the bead by the Langevin equation describing its stochastic motion inside the piston at a fixed length, we measure the quantity of work injected in the system, the heat produced by the whole reversible cross-over cycle and from a first principle energy balance, the total amount of energy change. These quantities are measured with a remarkable ca. $k_BT/100$ precision level. Throughout our reversible process, most of the injected work is consumed as a potential energy difference, the few remaining percent are lost as heat

when a configuration change occurs and the bead needs to relax to a new equilibrium position.

The thermodynamic approach, only touched upon in this Chapter, emphasizes how controlling and tailoring an optical landscape leads, through the control of the production of heat and potential energy differences, to the appealing possibility to induce any kind of thermodynamic processes.

4

SYNCHRONIZATION AND STOCHASTIC RESONANCE

In Chapter 3, the bistable dynamics of the bead was discussed in the quasi-static regime. In this Chapter, we carry on with the study of the Brownian dynamics of the bead immersed in a bistable optical potential but with an external forcing potential that forbids the bead to relax in the energy landscape associated with each sequence of motion.

The regime of an externally driven bistable potential is determined by the natural bistable dynamics of the bead on which is exerted an externally modulated force, derived from a time-harmonic potential $F_{drive}(t) = -\nabla U_{drive}(t)$, so that the force does not depend on the position of the bead:

$$F_{drive}(t) = F_0 \sin(2\pi f_d t), \tag{4.1}$$

where F_0 is the force amplitude and f_d the drive frequency.

With the addition of $U_{drive}(t)$, the resulting potential probed by the bead is not static. This is clearly illustrated in Fig. 4.1 taken from [24] in the simplest case of a symmetrical potential. The depth of the wells are modulated by the harmonic external drive. The resulting potential is displayed for 4 different positions of the external force within a drive period $T_d = 1/f_d$. Starting at the top, when the time t is a multiple of the drive frequency, the bistable symmetric potential is unaltered. After a quarter of period, on the right hand-side, the sine is 1 and a positive force is applied on top of the potential. The potential is hence deformed and the ratio of the well depth changes, with one metastable state favored over the other. After half a period, the potential becomes symmetrical again as the sine goes back to 0. Finally, with a -1 sine after three-quarter of period, a (negative) force is applied on the potential, deforming it again with the opposite metastable state this time favored, as the new lowest potential energy position.

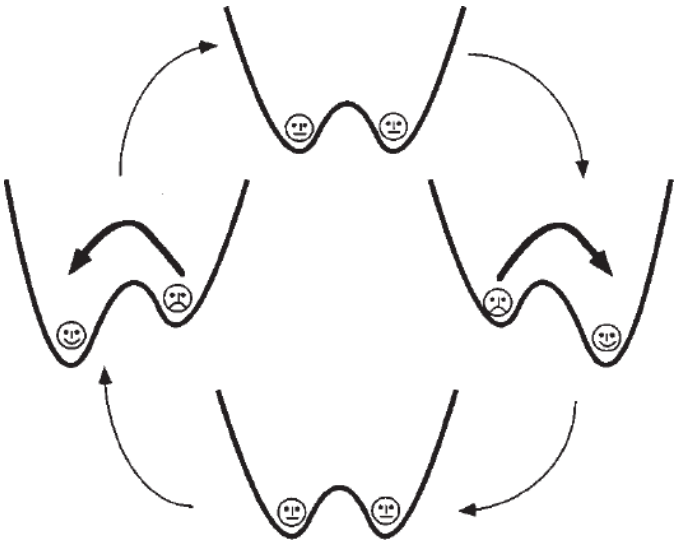

Figure 4.1: Schematic representation of a periodically modulated bistable potential. Every half period of the drive, the potential asymmetry changes wells. When the potential is biased, one well is favored within which the bead spends the longest amount of time. Illustration directly taken from [24].

Looking back at Fig. 3.5, the cross-over studied in Ch. 3 is made of a compression - decompression sequence, with *(i)* a compression stage where the piston is moved from an initial stable position to half of the cross-over configuration and, once a symmetrical bistable potential is reached, *(ii)* a decompression performed along the exact same path (easy to perform when considering a 1D displacement). The crucial difference with the dynamics studied in this Chapter lies in the facts that in Ch. 3, the crossing of configurations is one-directional and that the bead is allowed relaxing in each of the explored potential configurations throughout the reversible cross-over. With respect to Fig. 4.1, this is equivalent to having a very slow drive period or step-wise increments.

This picture however does not account for the fact that the bead itself evolves in a stochastic manner within the bistable potential thermally accessible, be it symmetric or asymmetric. The Brownian bead therefore has its own dynamics, characterized by the interaction landscape (local traps' relaxation times, mean escape times, etc.). The central question in this context of external forcing is to understand how, and under which conditions, the periodic modulation of the potential illustrated

in Fig. 4.1 is actually followed by the bead. This is at the core of the study of the phenomenon of stochastic resonance and this analysis constitutes the main objective of this Chapter.

4.1 SYNCHRONIZATION AND STOCHASTIC RESONANCE

It is known [24] that a bistable potential, when periodically modulated, can lead to a rich variety of phenomena, with the possibility to synchronize the stochastic inter-well dynamics of the bead whenever the drive frequency matches the so-called natural (Kramers) escape rate of the system. Going back to Kramers' formulation of a symmetric bistable potential (see Ch. 2), the escape rate writes as

$$k_K = k_r e^{-E_b/k_B T} \tag{4.2}$$

$$k_r = \frac{\sqrt{\kappa_w \kappa_b}}{2\pi\gamma} \tag{4.3}$$

where E_b is the height of the bistable barrier, κ_b the effective stiffness associated with the (negative) curvature of the potential at the barrier maximum, κ_w the stiffness associated with the wells, and γ the Stokes drag. The rate k_r characterizes the intra-well rate of relaxation. That $k_r \propto \sqrt{\kappa_b}$ and not merely proportional to $\sqrt{\kappa_w^2}$ precisely corresponds to the influence of the barrier as an open channel for escape, breaking the harmonic approximation that can be performed at the bottom of each metastable state.

From the separation of times argument presented in Ch. 2, Kramers' theory implies that $k_K \ll k_r$, which writes in the time domain as $\tau_r \ll \tau_K$ where τ_K correspond to an averaged waiting time between two inter-well transitions induced by the thermal fluctuations, in other words to a natural mean residency lifetime in one metastable state of the bistable potential.

In the case of a periodic drive exerted on the particle, a matching condition emerges when the forcing period T_d matches τ_K, more precisely when

$$2\tau_K = T_d. \tag{4.4}$$

At this condition, the bead synchronizes its position with the external drive. Depending on the strength of the external drive this synchronization effect is more or less marked. Remarkably in the case of a weak forcing, where forces induced on the particle are smaller than thermal forces, the thermal fluctua-

tions -that are the main source of state changes in the system- actually help to lock the bead activation over the barrier, in phase with the drive. In this regime, noise-activated jumps over the barrier become synchronized with the weak drive: one refers to stochastic synchronization or stochastic resonance.

This phenomenon of stochastic resonance has already been largely studied and exploited, in particular in the context of dual optical traps [7, 15, 54]. It can be studied from various angles, thermodynamically with the determination of the external work consumed by the system [15], or from the point of view of the evolution of the probability distribution of residency times [7]. It can also be viewed as a signal over noise ratio enhancement effect where the driven system, when synchronized, emerges out of the thermal noise floor [24] with interesting consequences in the context of weak force detection strategies [60].

Our optical piston configuration appears ideal in order to study such forcing dynamics. In our setup indeed, the bead evolves in a continuous potential, contrasting with experiments based on time shared traps (usually performed with a motorized mirror or acousto-optical deflector (AOD)). The singular aspect of our scheme is the truly one-dimensional (1D) nature of the motion of the bead along the optical axis, which differs from configurations where the bistable potential is generated laterally using two beams and the depth of the wells modulated by varying the beams' intensities.

In this Chapter, we will explore the different regime of forcing accessible with our setup. From the time-scale separation (4.3), the stochastic resonance is reached in the adiabatic regime $T_d \gg \tau_r$ where the short-time dynamics within each metastable state is fully decoupled from the drive. In this regime, for forcing period larger than the synchronization time $2\tau_K$, it becomes possible to actually rectify the motion of the bead within the bistable potential. This regime will be discussed in details in subsubsection 4.3.3.3. But, as we will show below, the possibility to drive at high frequencies leads to reaching a non-adiabatic regime with $T_d \ll \tau_r$. In this regime, the inter- and intra-well dynamics becomes mixed with specific motional signatures.

Our approach will be based on analyzing the residency time distributions in each of the metastable states and their evolutions as a function of the forcing parameters. The analysis of such residence-time distributions is an efficient tool

when studying stochastic resonance [7]. As emphasized by Gammationi *et al.* [24], this approach naturally stems from considering *"stochastic resonance as a 'resonant' synchronization phenomenon"*. In this view, stochastic resonance is a *"physical synchronization effect"* where the periodic drive acts as an external clock for the bistable system.

4.2 EXTERNAL FORCING AND CONTINUOUSLY DEFORMED POTENTIALS

The continuous deformation of the potential is a central characteristic of our optical piston setup. The description of such a deformation is done through the introduction of time as a new dynamical parameter in the potential itself. This implies that the potential $U(z(t),t)$ becomes a function of both space and time. Contrasting with the previous discussion (Ch. 2 and 3), the bead here does not evolves in successive fixed potential configurations.

With the necessity of separating spatial and temporal variables, the bistable dynamics of the bead is entirely fixed by the static part of the potential $U_0(z(t))$ while the periodic driving contribution $U_{drive}(z(t),t)$ alternatively pushes and pulls the bead. The potential writes therefore as:

$$U(z(t),t) = U_0(z(t)) + U_{drive}(z(t),t). \tag{4.5}$$

4.2.1 *Periodic compression of the piston*

A natural way for exerting a periodic forcing to the bead is to put the optical piston into periodic motion by considering here the mirror position $\ell(t)$ as a continuous function of the time, periodically modulated around an average position ℓ_0 by a time dependent harmonic function $\delta\ell(t)$

$$\ell(t) = \ell_0 + \delta\ell(t) \tag{4.6}$$

$$= \ell_0 + \ell_{mod}\sin(2\pi\, f_d\, t), \tag{4.7}$$

with ℓ_{mod} the amplitude of the modulation and f_d the drive frequency.

As was discussed in the previous chapters, the interaction potential in the optical piston experiment has a rich structure that cannot be expressed in a polynomial way. Nevertheless, assuming that *(i)* the potential shape is independent of the bead

position and that *(ii)* all possible dynamical back action from lensing effects (or photonic jets) created by the trapped object can be neglected, the interaction potential is given by:

$$U(z(t),\ell(t)) = U_M(z(t),\ell_0+\delta\ell(t)) \tag{4.8}$$
$$= U_0(z(t)) + U'_{drive}(z(t),t), \tag{4.9}$$

with $U_0(z(t)) = U_M(z(t),\ell_0)$ the unperturbed static bistable potential and $U'_{drive}(z(t),t) = U_{drive}(z(t),\delta\ell(t))$ the time-dependent modulated potential.

It is clear for the optical piston that $U'_{drive}(z(t),t)$ can not be expressed in a simple form like an amplitude $\times$ a sinusoidal drive. Nevertheless, a first order development of the potential around the mirror position ℓ_0 yields

$$U(z(t),\ell(t)) = U_M(z(t),\ell_0+\delta\ell(t)) \tag{4.10}$$
$$\simeq U_0(z(t)) + \left.\frac{\partial U_M(z(t),\ell)}{\partial\ell}\right|_{\ell=\ell_0}\delta\ell(t). \tag{4.11}$$

Taking both expressions 4.8 and 4.11 leas to identify a first order development of the perturbed potential as

$$U'_{drive}(z(t),t) \simeq \left.\frac{\partial U_M(z(t),\ell)}{\partial\ell}\right|_{\ell=\ell_0}\delta\ell(t). \tag{4.12}$$

It is important to stress here that the driving potential depends on the instantaneous position $z(t)$ of the center-of-mass of the bead. As such, this forcing is of a parametric nature.

4.2.2 *External harmonic forcing*

This parametric situation contrasts with the usual Duffing potential $U_{Duffing}(z) = \alpha z^4 + \beta z^2$ where modulating the trap potential is equivalent to applying a linear sinusoidal force on the bead $U_{drive}(z(t),t) = U_A z(t)\cos(2\pi\, f\, t)$. The exerted force is then a function of time only, and not anymore of the bead position $z(t)$. In such regimes the total force becomes:

$$F_{tot}(z(t),t) = -\nabla_z U_{tot}(z(t),t) \tag{4.13}$$
$$= -\nabla_z U_{Duffing}(z(t)) - \nabla_z U_{drive}(z(t),t) \tag{4.14}$$
$$= F_{Duffing}(z(t)) + F_{drive}(t). \tag{4.15}$$

The possibility to separate the potential in two terms, one term representing the rest potential, the other the exter-

nal drive, is critical. This is especially true when the force associated with the external drive has no dependency with respect to the bead position -as it is the case when considering the bead under the influence of an external periodical force field. Such conditions are not met in the optical piston forcing mode induced by modulating the position of the mirror. In this configuration, as described above, the driving force varies with the position of the bead in the trap. This marks a clear difference between the dynamical response of the trap under an external drive (independent of the bead position) and its parametric response when the forcing contribution is a function of the bead instantaneous position.

4.3 NUMERICAL EXPERIMENTS ON SYNCHRONIZATION PROCESSES

We now study numerically the dynamics of a Brownian bead trapped in a bistable potential via the resolution of the Langevin equation

$$m_B D_{tt}(z(t)) + \gamma D_t z(t) = F(T, z(t), t) - \nabla U(z(t)) \tag{4.16}$$

that describes the center-of-mass motion $z(t)$ of the bead.

Here, as fully detailed in Appendix A, we use differential operators with D_t the linear differential operator, $D_{tt} = D_t D_t$, m_B the mass of the bead, γ the viscosity of the fluid, $U(z(t))$ the potential energy exerted on the bead and $F(T, z(t), t) = \sqrt{2 k_b T \gamma}\,\eta(z(t), t)$ the Gaussian white noise with $\eta(z(t), t)$ a Wiener process.

Note that despite the fact that the inertial term has a completely negligible contribution to the bead dynamics in our conditions, it is included in our simulation for the sake of generality. When depending on time, the potential $U(z(t), t)$ will combine, as in eq.(4.5), a static term that will describe the metastable interaction potential induced by the optical piston and a driving contribution.

The typical displacements of micron-sized objects being around the tens of nanometers, some of the dynamic variables have very small values. Moreover, the thermal energy $k_B T$ in SI units is ca. 10^{-20} J/K and the mass of the polystyrene 1 µm bead of the order of 10^{-16} kg. In order to avoid possible numerical hindrances occurring when operating with very big or small values, we propose to change the unit system and use

micrometers, micrograms, seconds and absolute temperature in Kelvins. In this system, k_B has a value of $1.3806503\,10^{-2}\,\frac{\mu g\,\mu m^2}{s^2}$ and the mass of the bead around $10^{-7}\,\mu g$. The unit of force associated with our system is the femtoNewton (fN) which is exactly the order of magnitude of the forces measured experimentally (see Ch. 5 in particular). Similarly, the energy scale is at the zepto 10^{-21} Joule level, precisely the order of magnitude of the thermal fluctuation energy $k_B T$.

4.3.1 *A model for bistability: the Duffing potential*

We will perform our numerical experiments by resorting to the standard Duffing-type potential which allows discussing in a well-controlled manner the regime of bistability, in particular regarding the influence of the potential depths. The force associated to this class of potentials is written as:

$$F(z) = A * (-1 \times 10^4\, z^3 + 5 \times 10^2\, z), \tag{4.17}$$

with A an amplitude giving the strength of the force. Coefficients are chosen such that the orders of magnitude in the simulated signals are similar to the experimental data obtained in our experiments (see below).

Written under this form the potential is symmetrical with respect to the barrier, with a barrier-top located at a position $z = 0$ where both force and energy cancel. Integrating the force expression leads to the potential expression:

$$U(x) = -A * \left(\frac{-1 \times 10^4}{4}\, x^4 + \frac{5}{2} \times 10^2\, x^2 \right). \tag{4.18}$$

Such a potential and its associated force are drawn in Fig. 4.2 with an amplitude parameter A of 1. The red curve depicts the potential with a depth around 7 zJ (a bit less than 2 $k_B T$) and the force in blue is of the order of 100 fN.

We gather in Fig. 4.3 a few trajectories that we simulated from eq.(4.16) using a Duffing potential with different amplitudes A, in order to visualize the effect of the potential depth on the bead trajectory. The bath and the bead properties are kept constant.

For very small amplitudes (panel 4.3a, $A = 0.01$), the bead loosely diffuses in a localized region of space. The bead is trapped but the trajectory does not provide any hint regarding

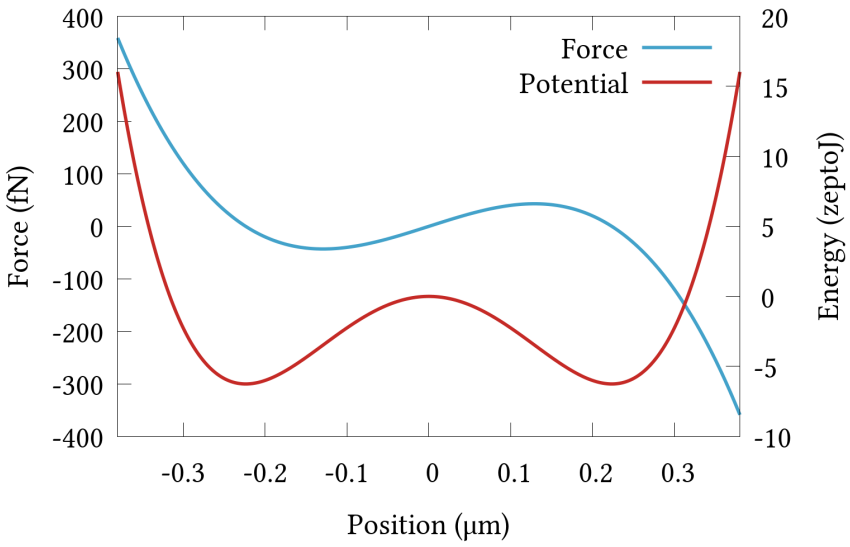

Figure 4.2: Duffing-type potential and derived force profile calculated with an amplitude parameter $A = 1$

the presence of two distinct attractors or regarding a fixed inter-well distance. It is not even clear that the bead avoids the central (repulsive) region of the barrier of the bistable potential.

For a moderately small amplitude (panel 4.3b, $A = 0.21$), the bead starts sharing its time between the two wells (at ± 0.220 μm). Furthermore, the shading in the central region of the time trace around $z \simeq 0$ appears lighter. The bead is mapping the potential well, but there is not yet a clear separation that would allow one talking about metastable states localized at the two wells positions.

Increasing the potential amplitude (panel 4.3c, $A = 1.41$) reduces the variance of the bead position in each of the wells and improves on the determination of the well positions. Because the spread in position is smaller, the rejection induced by the barrier becomes more apparent. The residency times in each of the wells increases. The large number of noise-induced hopping events between the two wells leads to start having a well-defined mean residency time. This trajectory perfectly illustrate the conditions of Kramers' theory based on a clear separation of intra- vs. inter-well dynamic times.

When the potential amplitude become too strong (panel 4.3d, $A = 4.91$), the bead barely hops between the wells, so that over the time of observation, only few transitions occur. The two attracting positions are sharply defined and unambiguously identifiable as well as the bottom position of each well. When

no transition occurs (or scarcely), there are long time intervals where the potential probed by the bead is only the potential at the bottom of the well, which is quasi-harmonic (although the general shape of the Duffing potential is not).

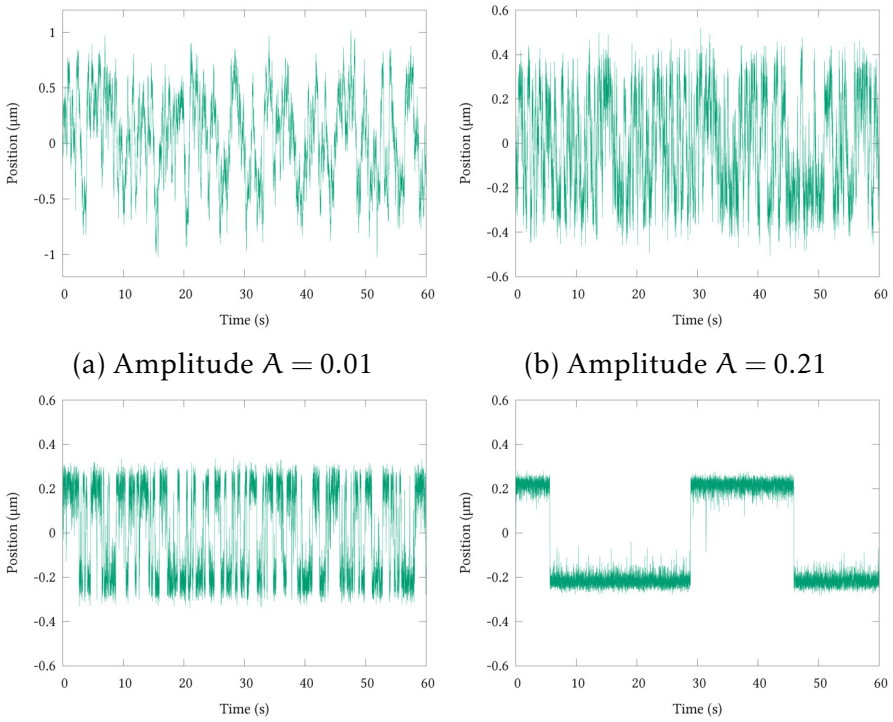

(a) Amplitude $A = 0.01$ (b) Amplitude $A = 0.21$

(c) Amplitude $A = 1.41$ (d) Amplitude $A = 4.91$

Figure 4.3: Simulated trajectories for a bead in the same environment but with different Duffing potential amplitudes A. All figures present the trajectory of the center-of-mass of the trapped bead for 60 seconds, with an associated time step equivalent to a sampling rate of 262 kHz.

4.3.2 *Statistical nature of bistability in the absence of drive*

It appears from this description that the evolution of the bead dynamics can be monitored looking at the the changes in the residency time statistics associated with each of the two attractors. In the context of an *escape* problem, it is critical to be able to properly validate what a hopping event is and how the escape is numerically accounted for.

One possibility is to define the escape position at the exact top of the barrier with a strict condition such as (*if* $[z > 0]$ *then* [state has changed]). But this choice of condition neglects the

fact that the bead sees a reduced force when approaching the top of the barrier. This implies an increased probability for the bead to come back, through thermal fluctuations, to its initial well after having crossed the barrier. Such a possibility is of no importance when considering only the escape time from one well and when mapping the potential through the time-traces of the bead, i.e. by integrating the trajectory as an histogram. But it definitely bias any residency time-based analysis performed over a whole acquisition.

Indeed, because the force applied on the bead is null or weak in a small region around the top of the barrier, the bead can recross the barrier a few times through mere Brownian diffusion. The strict condition becomes problematic: a short time later, the bead crosses the barrier backwards through diffusion, with the consequence that the state change condition becomes valid again. It is also problematic in the other (less frequent) recrossing scenario where the bead, coming from the first well and crossing the barrier, starts moving down-hill towards the second well but nevertheless, at some point, re-crosses the barrier to come back to the initial well, without having actually reached the bottom of the second well, despite the fact that it went down close to it.

These situations make clear why such a top-barrier condition leads to simulated mean residency times many times smaller than what is naively observed on the simulated trajectory plots in Fig 4.3. A criteria to circumvent this limitation was implemented in the previous chapter by defining an arbitrary time constant in order to separated fast fluctuations from the average bead motion. This separating time leads to filter out recrossing phenomena that occur on a shorter time scale than the typical relaxation time of the bead in one of the wells.

In this Chapter, we adopt another approach for identifying state changes. A change of state is only validated when the bead reaches the bottom of the opposite well. With this scheme, recrossing effects are fully taken into account: the bead can explore the region around the barrier and can come back to its original well without accounting for any state change. A slight drawback of our method is that time measurements happen to lag with respect to barrier crossing events. The lag is however systematic and therefore not critical for any statistical analysis when considering many realizations of noise-induced barrier crossings. But one clear numerical advantage of our criterion lies in the possibility to determine a change of state

while the signal is recorded (i.e. simulated) without having to store previous position values or having to take into account future events. This is exactly is necessary to implement with top-barrier condition, when the bead, in its near future, does not explore the opposite well but rather returns to its original state. For such scenario, the state change must be canceled *a posteriori* in order to be numerically consistent with mean residency time measurements.

4.3.3 *External periodic forcing in a Duffing bistable potential*

We now turn to numerical simulations of the trajectory of the bead trapped in a bistable Duffing potential in presence of an external periodic forcing. We define the rest potential in the absence of drive, with a bead trajectory simulated in Fig. 4.4 for a Duffing potential (4.18) with an amplitude $A = 2$. The trajectory displays well defined attractors and therefore a good time separation between the characteristic short time of the bead in the trap and its activation over the barrier which is defined on a slower time scale. In such a regime of clear time separation, Kramers' theory is valid.

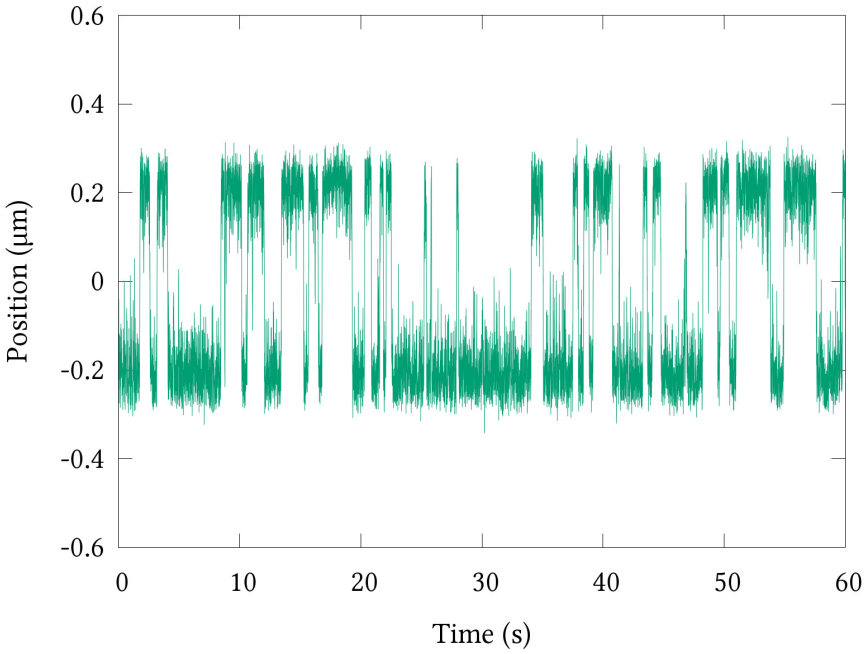

Figure 4.4: One-minute long simulated trajectory of a bead trapped in a Duffing potential of amplitude $A = 2$ in the absence of the external drive.

4.3.3.1 *The Mandel factor*

As emphasized above, our aim is to monitor the influence of the external drive on the statistical properties of the state residency lifetimes. Our approach is to analyze the evolution of the successive lifetime values computed along a given time-trace of the bistable trajectory of the bead. This series will be, as always, characterized by its two first momenta, namely lifetime mean values (those involved in Kramers' theory) and associated variances (that characterize the spread of the lifetime values).

Escape phenomenon from attractive (harmonic) potentials usually imply for the residency lifetime in the trap to follow a Poisson distribution [77] for which the mean is equal to the variance. The Poisson distribution is characteristic of non-correlated processes. It can be expected that in a bistable regime, the hopping mechanism could induce correlations in the distribution of residency lifetime in each metastable states.

A standard tool implemented in the field of quantum optics for characterizing induced correlations on initially independent processes is the Mandel Q factor. This factor describes the enhancement ($Q > 0$ - photon bunching signature of thermal light) or reduction ($Q < 0$ - antibunched non-classical light) of the photon noise with respect to the Poisson distribution [82]. We adapt this tool to our bistable dynamics defining a Mandel factor associated with the upper (up) and lower ($down$) metastable states

$$Q_{up/down} = \frac{Var(\tau_{up/down})}{Mean(\tau_{up/down})} - 1 \tag{4.19}$$

with the mean and variance computed for, respectively, the upper and lower residency times τ_{up} and τ_{down}. How these times are actually measured from the time-traces within the framework of our state change identification method is explained in Fig. 4.5.

With $Q = 0$, the distribution of residency lifetimes is Poissonian, where all successive residencies are independent to each other. Correlations appear as soon as $Q \neq 0$.

- For $Q < 0$, the variance is smaller than the mean. With a small spread of lifetimes around the mean, successive values tend to be similar. In the time domain, this implies that successive events tend to be evenly separated. In our experiments, this sub-Poissonian regime will obviously be a feature of a synchronization mechanism, with a

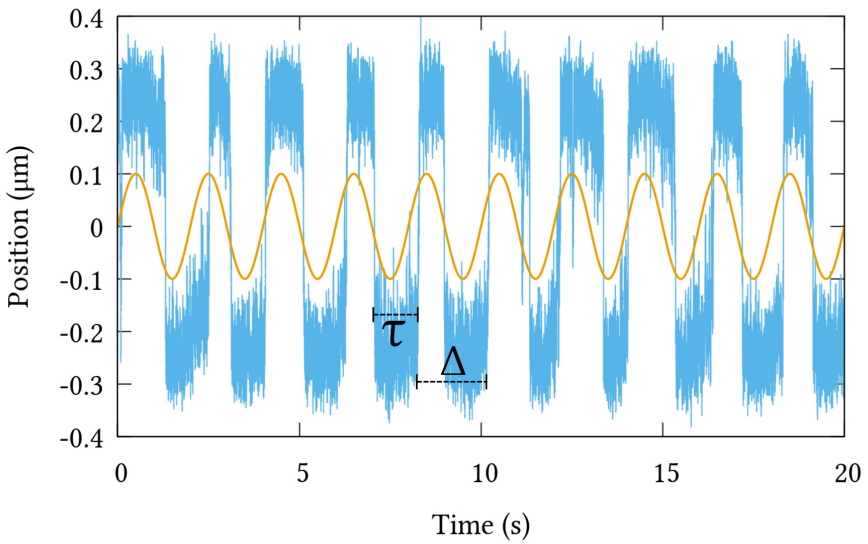

Figure 4.5: Simulated time trace for a potential amplitude parameter of 2. An external force of 80 fN is applied on the object and modulated at 0.5 Hz, the Kramers mean escape frequency of the non-driven potential. The blue curves shows the position time trace of the object and the orange curve is the applied drive. The figure also illustrates one residency time τ in a state (the low positions state) and a transition delay Δ between two successive escapes of the same kind.

mean residency lifetime well defined in the sense that its dispersion around the mean is minimal. $|Q|$ values increase as the synchronization gets stronger (down to the $Q = -1$ perfect synchronization limit).

- For $Q > 0$, the variance is larger than the mean, and the statistics becomes super-Poissonian. The spread of values being large with respect to the mean, a sequence of events is characterized by successive short events followed by long 'blanks'. In our experiments, positive Q factors imply that one well is favored over the other. This is the signature of a localization process within the bistable potential that can be interpreted as a *rectified* bistable dynamics for the bead.

Note that the Mandel factor has the dimension of the quantity under study. Because of this, no normalization is performed via Q: experiments that compare different dynamical regimes through the Mandel factor have to be expressed in the proper dimension.

4.3.3.2 *Evolution of the Mandel factor in the absence of an external forcing*

It is interesting to look at the evolution of the Q factor as the potential amplitude A is varied (that is, the depth of the potential is changed). Figure 4.6 shows the mean, the variance and the Q factor of the residency lifetimes of the upper metastable states. On this figure, 64 realizations of the bead trajectory in every potentials are simulated. The statistical parameters are then extracted and averaged, with corresponding error bars. We only show the statistics for one of the two well since the potential is perfectly symmetric. As observed, there is one single point (around $A = 2.1$) where mean and variance cross, i.e. where the bistable dynamic is strictly Poissonian. This is seen on the Mandel Q factor with $Q = 0$ on the right axis. We therefore conclude that even for simple Duffing potentials, there is a unique combination of inter-well distance, barrier height and thermal energy that provide a truly Poissonian statistics of the residency lifetimes. The sub-Poissonian regime ($Q < 0$) is the region of low potential depths where more state transition events occur and the super-Poissonian regime ($Q > 0$) emerges in regions of deep potential wells.

4.3.3.3 *Evolution of the Mandel Q factor with an external harmonic forcing*

An external drive is now added to the bistable potential that has been carefully prepared in the symmetric configuration, characterized by a *rest* Mandel factor Q_{rest}. Different dynamical regimes can be distinguished over the parameter plane (amplitude, frequency) of the external forcing. These regimes are schematized in the diagram 4.7. As already explained in the introduction of the Chapter, three frequency regimes can be identified: the adiabatic regime, over which the frequency of the drive $f_d \geqslant f_K$ the natural Kramers frequency, the synchronization regime where $f_d \simeq f_K/2$, and the non-adiabatic regime where $f_d \ll f_R$ the intra-well relaxation frequency. Depending on the strength of the forcing (i.e. the amplitude of the external drive), the evolutions of the statistical distributions of the mean residency lifetimes correspond to specific dynamical phenomena.

Our simulations will enable us to explore these regimes and illustrate these phenomena. We will start with an initial Duffing potential amplitude $A = 2$ for which the mean

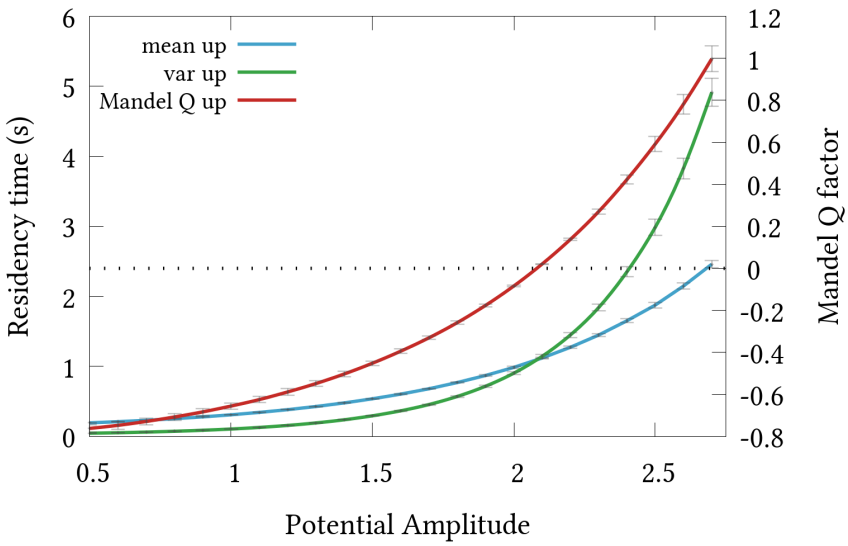

Figure 4.6: The mean, the variance and the Mandel Q factor are presented for a non-driven bistable potential with various potential depth A. 64 simulations of 128 minutes each, are realized with a sampling rate of 262 kHz and the statistical properties of each averaged. Simulations are run with the same bath parameters for each varying amplitude. The blue curve shows the averaged residency lifetime while the green curve is the averaged variance. The resulting Mandel Q factors are displayed in red.

residency lifetime distribution is close to be Poissonian with $Q_{rest} \simeq -0.06$.

A first pool of simulations are performed varying the driving frequency and fixing the external drive at two different amplitude levels: a strong drive of 80 fN and a moderate one of 20 fN. For these simulations, very long runs are considered with each of the 64 realizations, representing 512 minutes of trajectory. Such a large pool is important in particular when aiming to study the low frequency regimes where events occur less frequently. This is leading to averaged values with error bars that are determined over many realizations of the same potential, with identical initial conditions, but performed with different baths.

The results of these numerical experiments are displayed in Fig. 4.8. As presented in the diagram 4.7, three distinct regimes are identified. The region centered around the Kramers frequency $f_K = \frac{1}{\tau_K} = \frac{1}{0.99} \simeq 1.0$ corresponds to the synchroniza-

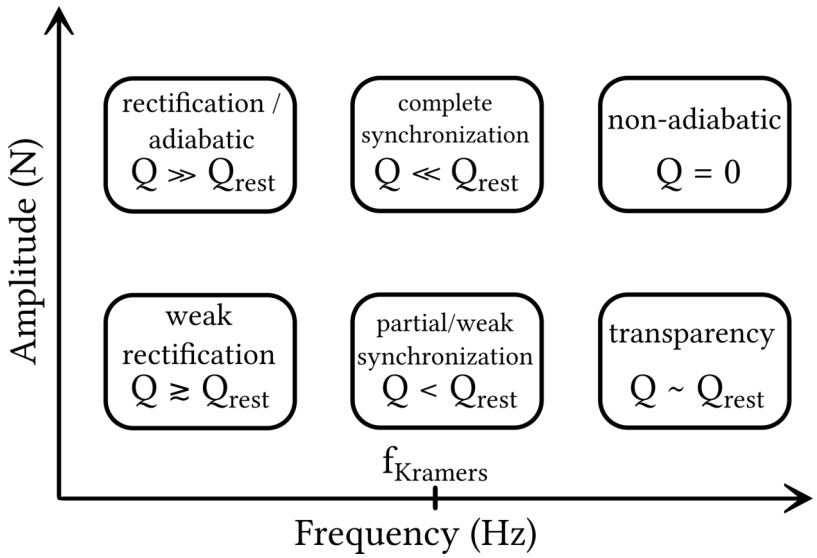

Figure 4.7: Diagram illustrating the different statistical regimes that a bead can explore in a bistable potential as a function of the external drive frequency and amplitude. These regimes are simply characterized by their Mandel Q factor with respect to Q_{rest}, the Mandel factor of the initial unperturbed bistable potential.

tion regime where $Q < 0$ is below Q_{rest}. As expected, the lowest Q factor in this region is around 0.5 Hz which is indeed near the natural activation frequency of the bead over the barrier such that $f_d \simeq f_K/2$. Yet, synchronization is not perfect ($Q = -1$): in fact, thermal fluctuations still randomize the precise time at which the bead hops over the barrier.

At high frequencies, the drive is so fast that in the case of a moderate drive amplitude, one recovers the initial bistable statistics: this is the so-called transparency limit. However, for a larger drive amplitude, $Q \simeq 0$, implying that the distribution of residence events becomes Poissonian. Such conditions correspond to the non-adiabatic regime where the forcing cannot be considered as an external perturbation *adiabatically* separated from the bistable potential. The drive happens on such a short time scale that the bead does not relax in a well-defined metastable state.

The low frequency regime appears particularly interesting. With large $Q > 0$, the super-Poissonian distribution corresponds to a rectified bistable dynamics. Here, the drive frequency being much smaller than the natural transition frequency, the bead tends to be forced to stay in one of the two

metastable states. Thermal fluctuations still lead to hopping events through the slowly varying drive. But these occurrences are short lived and the bead soon returns to its initial well to follow the drive. While it is clear that the combination of short and long residency times increase their variances, leading to $Q > 0$ values, the rectified motion implies that when the bead escapes a metastable well, its probability to come back to that initial well is very high. This is a typical non-Markovian situation where the nature of one event essentially determines the outcome of the next one.

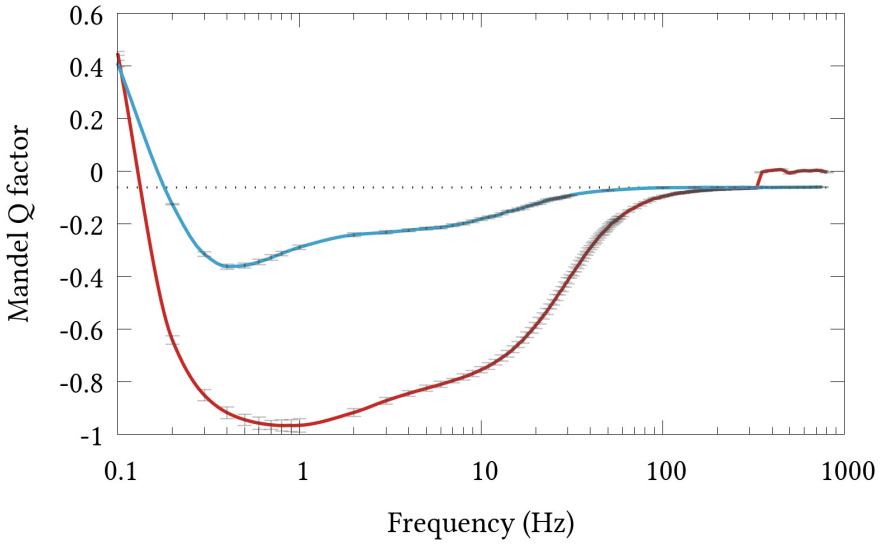

Figure 4.8: Evolution of the Mandel Q factor for strong (80 fN -red) and moderate (20 fN -blue) drive amplitudes over a wide range of frequencies. 64 simulations of 512 minutes each, are realized with a sampling rate of 262kHz and the statistical properties of each averaged. The horizontal dashed line is set at the value of the initial Mandel factor $Q_{rest} = -0.06$ of the unperturbed bistable potential.

4.3.3.4 *Monitoring the onset of ergodicity*

We observe that at low driving frequencies (0.01 Hz), the Mandel factors associated with the upper and lower residency time distributions are different (the error bars do not overlap), despite the symmetric character of the bistable potential. This contrasts with what is seen at higher frequencies, with exactly similar Q up/down factors. The deviation between the Q

factors associated with the up and down metastable states observed at low frequencies is plotted in Fig. 4.9 as a function of the simulation time T (given in units of 512 minutes).

These plots show how the initial localization of the bead determines, over a certain time, the whole dynamics. The initial metastable state in which the bead is placed in the beginning of the simulation thus biases the symmetric distribution of Q factors expected from the perfectly symmetric shape of the bistable potential.

It turns out that by performing the simulation over long enough times, both Q factors eventually converge, as seen on the Figure: both values have perfectly merged for a time $T = 512 \times 16 = 8192$ minutes. In the condition of these simulations, the separation is still visible after 2048 minutes, implying that one has to wait more than 10^3 periods in order to lose any dependence on the initial position of the simulated trajectories. This numerical result actually stresses the huge sensitivity of the bistable dynamics towards single irregular events with an external drive at low frequencies. But it also nicely brings forward a simple way to look at how ergodic conditions can be ensured at the level of our numerical experiments.

4.3.4 *Increasing the external forcing amplitude*

A second pool of numerical experiments explores the influence of the forcing amplitude on the frequency evolution of the Q factors. The results are gathered in Fig. 4.10. A clear departure from the resting Q parameter (dotted line) appears even for a low driving amplitude around the synchronization frequency. At a driving amplitude of 5 fN, the synchronization bandwidth is smaller than 1 Hz.

With increasing amplitude in the driving force, the strength of the synchronization (measured by $|Q|$) increases together with the synchronization bandwidth. Remarkably, an increase in the drive amplitude shifts the maximal frequency of synchronization to higher values. We will confirm this trend experimentally below.

As already observed, the non-driven dynamics is recovered at higher frequencies. At low frequencies with $Q > 0$, the bistable dynamics is rectified by the drive.

At strong forcing amplitudes, the bead can still follow the drive as the driving frequency increases. One therefore can expect that the mean residency time in one metastable state

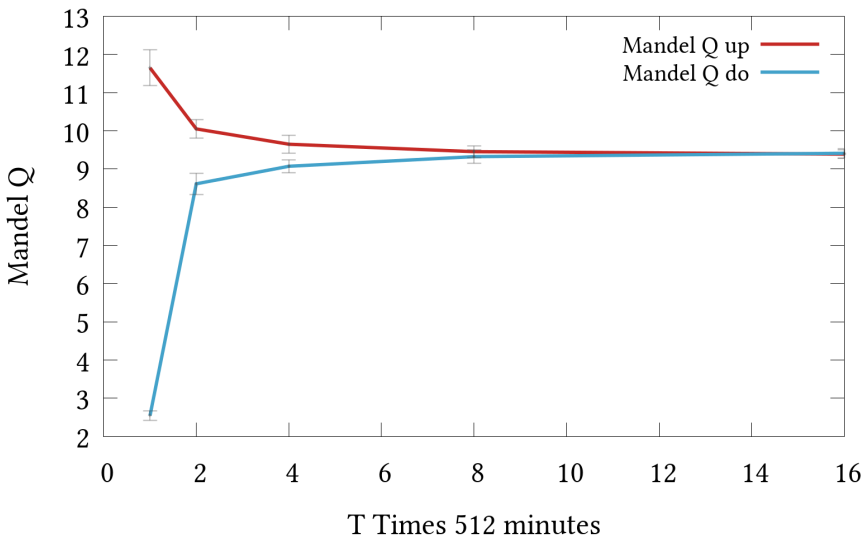

Figure 4.9: Evolution of the Mandel Q factor for both upper and lower metastable states as a function of the acquisition time, when the bistable potential is driven at a very low drive frequency (0.01 Hz, amplitude 80 fN). 64 simulations of $512 \times T$ minutes each, are realized with a sampling rate of 262kHz. The statistical properties of each realization is then averaged.

will decrease. Nevertheless, as we have seen, the regime of maximal synchronization occurs at a specific frequency near the natural transition Kramers frequency f_K associated with the rest potential. Figure 4.11 confronts the frequency evolution of the mean residency lifetime in one of the two metastable states to the evolution of its Mandel Q factor. Only the characteristic parameters for one state are displayed because they are the exact same for the other state in the considered frequency range.

As observed, the lifetime minimum occurs at a higher driving frequency (around 8 Hz) than the frequency of maximum synchronization. This can be simply understood: the bead is still synchronized at this frequency and therefore partially follows the drive. In such regimes, the state transition does not occur for every drive period but the drive provides enough opportunities to help in activating a state change, often at multiple of the period. On average, because more state changes occur, the mean residency lifetime will become smaller but state changes become more spread. This interesting effect will, too, be observed in our experiments.

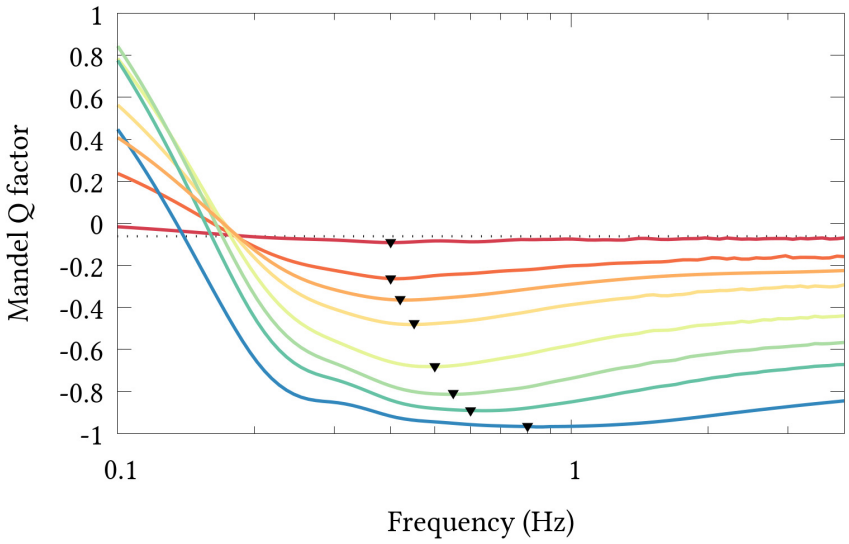

Figure 4.10: Evolution of the Mandel Q factor as a function of increasing external drive amplitudes. 64 simulations of 128 minutes each, are realized with a sampling rate of 262 kHz and the statistical properties of each averaged. The external drive amplitudes range from 5 fN (in red) to 80 fN (in blue). Intermediate amplitudes are: 15, 20, 25, 35, 45, 55 fN. The frequency range $[0.1 - 4]$ Hz is centered on 0.5 Hz, the natural Kramers frequency associated with the non driven bistable potential. The minimal Q parameter recorded on each curve is represented as black triangles. The rest Mandel factor Q_{rest} is given by the dotted line.

4.3.5 *Transition time delay analysis*

There is another approach to analyze the evolution of the distributions of hopping events that consists in building probability histograms associated with the time delays between successive changes of metastable states of the same kind: either transitions from lower to upper metastable states or transitions from upper to lower states. This yields two series of data for a given drive frequency, as schematized in Fig. 4.5. As we now show, a delay-based analysis is a good complement to the Mandel Q factor description.

In our simulations, the phase of the external drive can be recorded at the exact time when a hopping event occur. Then, the delays between successive changes of the same kind

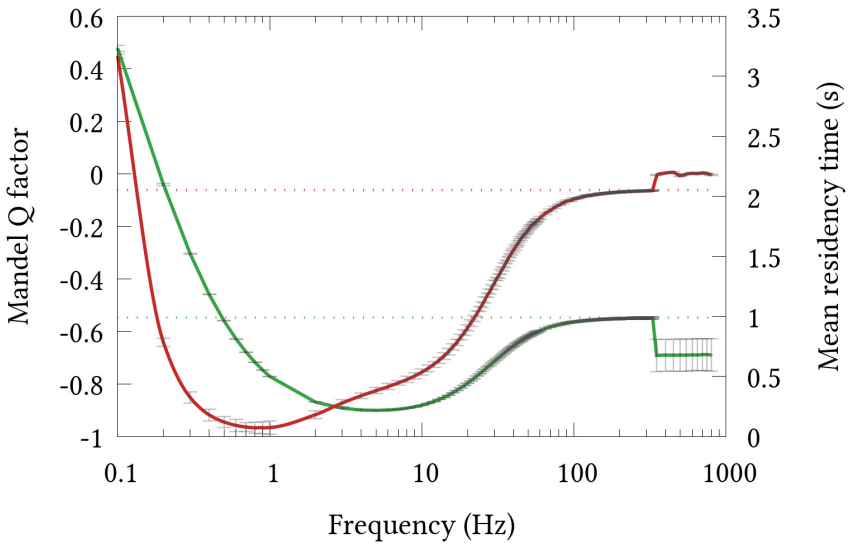

Figure 4.11: Comparison between the Mandel Q factor and the mean the residency lifetime in one metastable state, considering an external drive amplitude of 80 fN at different frequencies. 64 simulations of 512 minutes each, are realized with a sampling rate of 262kHz and the statistical properties of each averaged. The maximum of synchronization, i.e. where Q is minimal (red curve, axis on the left), differs from the shortest residency life time (green curve, axis on the right) of the bead in the state. Dashed lines represent the values without drive for both quantities in their respective colors.

are determined with respect to the drive periodicity. Fig. 4.5 summarizes the measurement of the phase delay Δ. This delay in a bistable potential reduces to computing the difference in the two successive instants the object reaches the opposite state.

The time delays are then converted in "drive delays" by simply normalizing the time between two event of the same kind with the drive period T. This enables us to built a distribution of the transition probability of changing state as a function of the number of period between two state changes of the same kind.

Such a construction is presented on Fig. 4.12 for the same rest potential, with four significant regimes that can be identified:

- when the drive period is much longer than the natural Kramers residency lifetime of the bead in a metastable state (the low frequency regime of rectified motion). In

such a regime, as shown in panel 4.12a, a state change occurs before the end of a single period T of the drive. This implies that there is still a strong signature of the natural distribution (close to Poissonian) at short times,

- when the drive period is slightly reduced, we observe in panel 4.12b a progressive depletion of the initial short-time distribution which start populating multiple harmonics of the drive period. This marks the onset of synchronization,

- when the drive frequency starts matching the natural Kramers transition frequency, the synchronization phenomenon is clearly visible on panel 4.12c. State changes mainly occur at multiples of the drive period with a severe reduction in the short time probability distribution. Synchronized transitions are observed up to five periods of the drive. This means that the drive is slightly too fast, forcing the bead to wait over multiple periods before hopping to the next metastable state. Obviously, the probability to remain in the same state decreases with the number of waiting periods, as observed indeed in the simulation with a probability envelop that decays exponentially,

- when the drive period is much shorter than the natural Kramers residency lifetime, panel 4.12d reveals that the distribution of state changes becomes much larger, with transitions occurring up to 100 times the drive period. Although the bead still follows partially the external drive, it progressively becomes transparent.

4.4 EXPERIMENTS

We now present the experiments corresponding to the external forcing of the bistable potential that we performed inside our SWOT configuration. Two different types of experiments have been done:

- A first experiment where the bead is inserted in our optical piston which length is adjusted in order to obtain a rest bistable potential as symmetric as possible. The end-mirror of the piston is then moved periodically, modulating the potential around the initial symmetric configu-

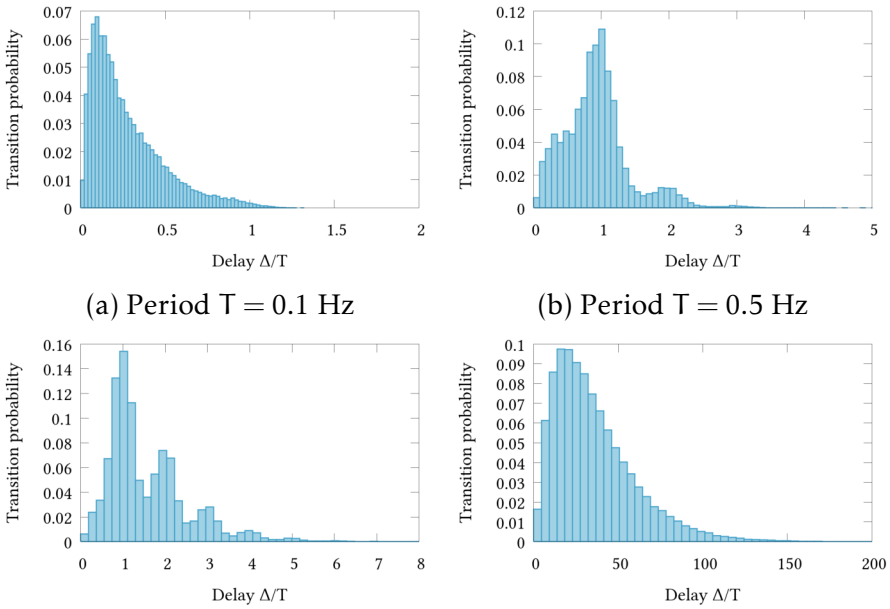

(a) Period T = 0.1 Hz

(b) Period T = 0.5 Hz

(c) Period T = 1 Hz

(d) Period T = 20 Hz

Figure 4.12: Simulated histograms of the transition probabilities for state change of the same kind, for a drive amplitude of 80 fN, as a function of the number of drive periods.

ration. This experiment corresponds to a parametric drive nd is described by eq. (4.8).

- A second experiment, where the piston is again adjusted to a bistable configuration but this time, the external forcing is done by a second laser injected in the SWOT that exerts a strong, external, optical force on the trapped bead. This is similar to eq. (4.15) but the rest potential is the one of the optical piston.

4.4.1 *End-mirror modulation*

In this first experiment, a 1 µm polystyrene bead is trapped in a SWOT formed between a (0.85 NA, 60×) air-objective and a gold mirror using a 785 nm trapping laser beam. The beam reflected by the mirror is recollected by the objective and sent to a PIN photodiode after being spatially filtered by a pinhole. A schematic representation of the experimental setup is given on Fig. 4.13.

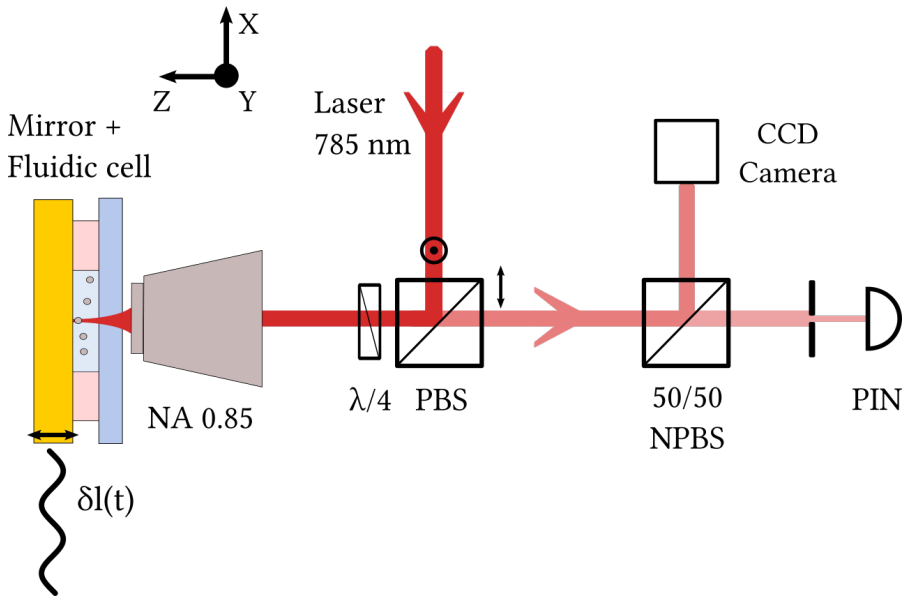

Figure 4.13: Schematic of the experimental setup for the parametric perturbation of the potential. The bead is trapped in a standing wave in front of a gold mirror (SWOT). The mirror position is periodically modulated at a given amplitude $\delta\ell(t)$ and frequency.

The mirror, mounted on a piezo stage, oscillates at a given frequency and amplitude $\delta\ell(t)$ in order to deform periodically the potential $U(z(t),t)$ around the rest mirror position ℓ_0,

$$U(z(t),t) = U_M(z(t),\ell_0 + \delta\ell(t)). \tag{4.20}$$

As we discussed in subsection 4.2.1, this method of external forcing corresponds to an effective parametric excitation of the system, the drive term being proportional to the instantaneous position of the bead.

For this experiment, the long-range step piezo motor (Newport PZA12) used to move the fluidic cell over millimeter-distances is actuated in an open loop mode, yielding a 30 nm position resolution. Because the open loop mode does not allow sinusoidal displacement of the mirror, a fine grained closed-loop piezo actuator (Newport NPA50SG) is added. This new piezo actuator has a short displacement range of 50 µm with a of 1nm resolution in position. The long-range stepper actuator is installed on a secondary translation stage that holds the new closed loop actuator in contact with the sample translation stage. Using this strategy, the coarse mm-long displacement

of the mirror is preserved while the new actuator offers the requirements to drive the mirror harmonically. When performing an experiment, the long range piezo is first displaced, its position is locked before the closed loop piezo motor is actuated. This actuator is driven by a frequency generator in order to generate a sinusoidal displacement of the mirror with a chosen frequency and amplitude, around a rest value chosen in such a way that the bead exhibits a quasi symmetrical bistable dynamics.

To do so, the mirror is approached towards the trapping beam waist (using the stepper actuator) and its position adjusted about 3 µm behind the waist (using the closed loop actuator). By finely tuning the position of the mirror ℓ_0, a symmetric bistable regime is obtained and the associated Kramers mean residency times are determined.

The mirror position is then periodically modulated at a frequency matching Kramers residency times. In our experiment the drive period is of 1 Hz and the amplitude of 80 nm. Under such conditions, a strong synchronization is recorded as shown in Fig. 4.14. The intensity time trace exhibits a whole region where state transitions are well synchronized with the drive.

Note that, while the signal separation between the two states is widely marked thanks to the collection pinhole (see Ch. 2), the intensity signal keeps trace of the mirror position when this one is modulated. This makes the determination of the instantaneous position of the bead difficult. A solution would be to subtract to the time-trace a sinusoid proportional to the drive to the signal. But in our configuration, where the measured intensity is not linear with the bead position, such a simple substraction scheme would be unreliable.

Another difficulty with this experiment arises when the drive frequency is increased (with a fixed amplitude). It turns out that for increasing frequencies, the displacement of the mirror $\delta\ell(t)$ increases with a maximum observed around 100 Hz. Throughout a wide frequency range (up to 1 kHz), the feedback control of the piezo reports the selected constant drive amplitude. This suggests the existence of a mechanical resonance in one of the translation setup (one of the stage or a coupling between both).

These shortcomings have led us to adapt the optical setup in order to be able to drive the bistable potential by a genuine external force.

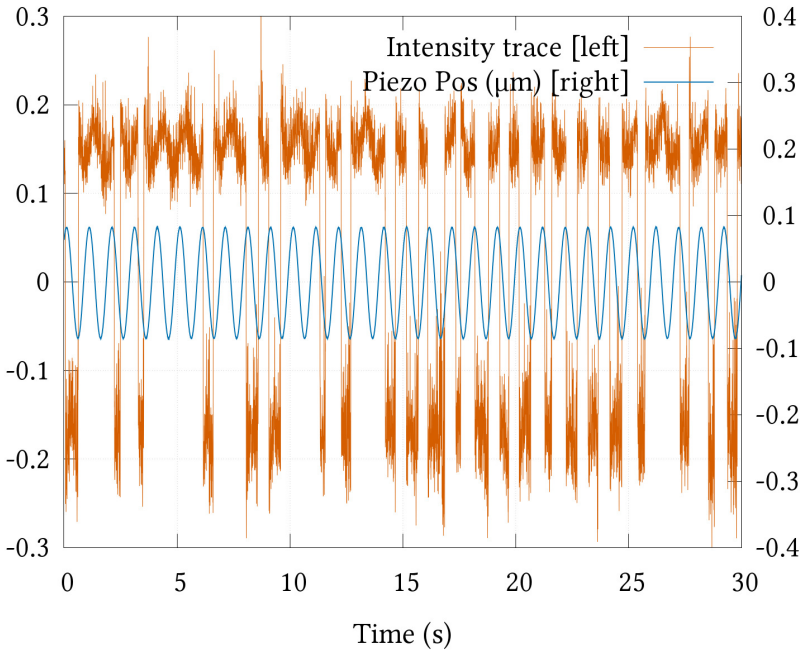

Figure 4.14: Illustration of a 30 s long time-trace recorded with a 1 Hz drive of 80 nm. The orange curve gives the time-variation of the intensity measured by the PIN photodiode, corresponding to the instantaneous trajectory of the bead. The blue curve is the instantaneous position of the closed-loop piezo actuator. The intensity trace, function of the bead position follows the external drive with synchronized state changes clearly visible.

4.4.2 *External force drive*

These difficulties have led us to modify our setup in order to reach simpler conditions where the external forcing of the interaction potential $U(z(t),t)$ is done via an external optical force directly exerted on the bead. This approach corresponds to the simple expression of a time-dependent potential associated with the external driving force superimposed to a rest bistable potential:

$$U(z(t),t) = U_0(z(t)) + U_{drive}(z(t),t). \tag{4.21}$$

The experimental setup described in Fig. 4.15 is adapted in such a way as to permit the addition of a second laser beam

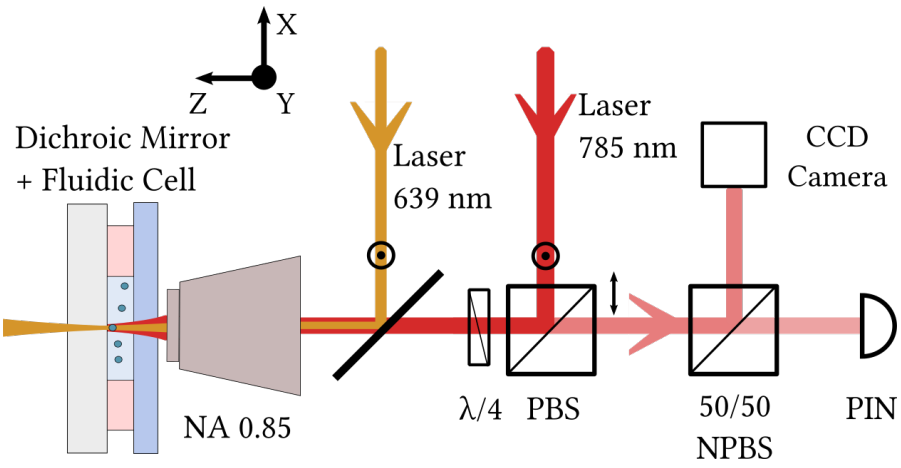

Figure 4.15: Schematic setup of the experimental configuration used to apply an external force on a trapped bead in a bistable potential. The gold mirror is replaced by a 0° dichroic mirror used to form a SWOT with the 785 nm (Excelsior, 45 mW) laser beam. A second beam at 639 nm (Thorlabs laser diode, 70 mW) is inserted collinear to the trapping beam by a 45° dichroic mirror. This second beam is modulated at a given amplitude and frequency acting as the external driving force.

that can act as the source of the external *pushing* optical force, without perturbing the trapping conditions. To do so,

- The gold mirror is replaced by a 0° dichroic mirror that is reflective from 700 nm to the near infrared regime and transparent below. This ensures that the 785 nm laser beam is reflected and a SWOT is formed on top of the mirror.

- A second beam at 639 nm is inserted in a collinear way to the trapping beam by a 45 ° dichroic mirror (with a cut off frequency of 710 nm) transparent to the trap beam. This laser, perfectly transmitted through the 0° angle dichroic mirror, will act as the external drive.

- The trapped probe particle, previously a 1 µm polystyrene bead, is replaced by a 1 µm melamine bead (from Fluka). We observed indeed that melamine beads (with higher refractive index than polystyrene -1.68 vs 1.57) are more stable in the SWOT than polysterene beads, with mean residency times obtained in bistable regimes slightly shorter.

- All the recollected light from the trap beam is sent to the PIN photodiode. There is no filtering (pinhole) needed anymore in order to observe a good state separation in bistable regimes, since the higher refractive index of melamine gives a better contrast in the recollected signal.

4.4.2.1 *Detailed experimental protocol*

The following protocol is implemented in order to *(i)* reach a bistable dynamics and *(ii)* perform the synchronization experiment.

In a first stage, the stepper actuator brings the waist of the trapping beam on the mirror, before the closed loop actuator is moved to generate the trap a few micrometers away from the surface. After a bead enters in the trap, the "pushing" laser is turned on -but not yet modulated- and its intensity tuned to keep the bead stable in the trap. The mirror position is then adjusted to obtain, with both lasers active, a symmetric bistable dynamics where the bead shares its time equally between the two metastable states.

Once the appropriate initial conditions of symmetric bistability are reached with the two lasers on, a frequency generator is used to modulate the pushing laser beam intensity (through a modulation of the current supplied to the laser diode) at a given frequency. This approach is useful in order to simulate a negative force acting on the bead. Indeed, in this configuration, reducing the pushing laser intensity is equivalent to pulling the bead backward. This resolves the difficult, but necessary in our 1D configuration, task of creating a negative force on the bead. It is clear that in the bistable regime, even without driving the system, the potential created by the trapping beam is not a bistable symmetrical potential. It is only with the addition of the second pushing beam that the bead spends an equal time on both sides of the waist. Increasing or reducing the intensity around this mean value for the pushing laser beam effectively adds or subtracts a force applied on the bead. It is the combination of potentials associated with each beams that yields our effective symmetric bistable potential.

Care is taken to ensure that the second 639 nm laser beam only acts as a pusher. This beam is focused 3 to 5 micrometers before the waist of the trapping beam (a shorter wavelength for the pushing laser helps in achieving this!) and does not entirely fill the entrance of the objective. This decreases the effective NA and as a consequence, reduces the gradient force contribution

of the pushing laser beam. We verified that the 639 nm beam does act as a pusher and is totally unable to trap the bead. For instance, it does push immediately the bead against the mirror as soon as the 785 nm trapping beam is switched off. We will make the reasonable assumption, although this is difficult to fully guarantee, that the pushing force is constant over the 300 nm spanned by the axial displacement of the bead.

4.4.2.2 *Allan variance*

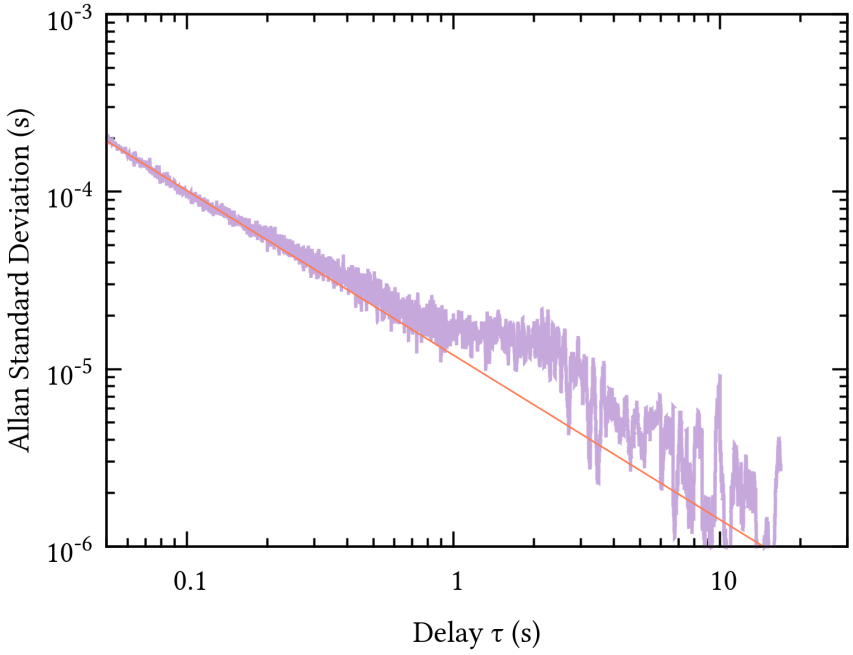

Figure 4.16: Allan standard deviation computed from a 1 minute long acquisition for a 1 µm trapped melamine bead. The bead is trapped with a mirror configuration such that the potential is quasi-harmonic. The red line represents the thermal noise limit.

An important limitation in our experiments comes from the fact that reaching a clear bistable (symmetrical) regime is difficult and does not last for too long, mainly because of slow drifts in the experiment. Drift of the fluidic cell in particular have obliged us to improve on our cell design, but despite our efforts, we have been limited in the synchronization experiments to a ca. 10 s long integration time for each sequence. This can

be compared to the stability of the experiments of Ch. 2 and 3 performed over $30-60$ s.

The Allan variance is an interesting tool that leads to measure the time over which the experiment can be considered as statistically stable [83–85]. The Allan variance is computed from normalized (3 points) variances of a signal at different bandwidth for a given delay τ in the series of points,

$$\sigma_y^2(\tau) = \left\{ \sum_{i=0}^{1} \left[\frac{x((i+1)\tau) - x(i\tau)}{\tau} \right]^2 - \frac{1}{2} \left[\sum_{i=0}^{1} \frac{x((i+1)\tau) - x(i\tau)}{\tau} \right]^2 \right\}. \tag{4.22}$$

The time of stability (i.e. the optimal measurement time) corresponds to the minimum in the Allan variance.

In practice, the long time-trace is subsampled in order to provide various shorter traces of a given length which variance is computed using eq. (4.22) and averaged over all down-sampled series of the same delay:

$$\sigma_{Allan}^2(\tau) = \langle \sigma_y^2(\tau) \rangle \tag{4.23}$$

The Allan standard deviation (the square root of the variance) of a trapped melamine bead is shown in Fig. 4.16. The variance of the measured intensity (almost proportional to the displacement of the bead) follows the thermal limit (red curve) for short time scales (below 1 s). In this region, the stability is optimal and the main source of noise is the bath which also drives the dynamics. Above 1 s, the Allan variance departs slightly from being thermally limited but stays low, up to at least 10 seconds. From this curve, it is apparent that an acquisition time of 10 seconds is fully valid, the noise associated with the measured intensity variance remaining at a low level.

Dispersion in the variance makes higher time delays non-significant. Our acquisition card does not permit longer acquisitions at our usual sampling rate. Computing the variance above 15 seconds gives dispersed values even for successive time delays. We consider this region as non significant because it is statistically ill defined (too few samples are available when computing the variance). Nevertheless, the determination of the trap stability at longer times is interesting. Empirically, we estimate 30 s as a good upper limit, when all other cultural noise sources are minimal.

4.4.3 *Synchronization, time-traces, and PSD*

As explained above, a synchronization measurement is performed only when a symmetric bistable interaction potential has been formed in the SWOT including the contribution of the pushing laser, *not yet modulated*. That the potential profiles are all similar is important in oder to be able to compare different residency lifetime / time-delays distributions. But this obliges us to go through a tedious protocol.

Starting from an apparently robust bistable dynamics (as observed on a oscilloscope with a good separation of times), we retract the mirror 20 nm away from the initial position and acquire a first time-trace over 10 s. We then move step-wise the mirror back forward, by steps of 2 nm. Doing this, we actually cross the bistable region (see Ch. 3). At each step, a 10 s time-trace is recorded.

This sequence is repeated for each modulating frequency of the pushing laser, over the chosen frequency bandwidth. All the time-traces and associated histograms of all the acquisitions are then displayed, from which all the traces stemming from non-symmetric histograms are simply discarded. This is how we are able to ensure (up to experimental errors and limitations) that the potential exerted on the bead is bistable and *on average* residency lifetimes are evenly symmetric, throughout the drive frequency scan.

Typical validated data are shown in Figs. 4.17 and 4.18. The histogram representation in particular is helpful in checking the symmetric character of the bistable dynamics. Such data are then exploited through the residency time statistical analysis in order to study the bead dynamics with a high level of precision.

It is interesting to look at the PSD associated with the time-trace of Fig. 4.17 acquired by the PIN photodiode. This is done in panel 4.19a which clearly displays the complex dynamics observed at low frequency on the time trace: bistable transitions do not exactly occur at the same frequency each time. The contribution state changes is actually strongly observed at 2 Hz. As expected from the fact that state changes are fast hopping events, their contribution does not follow a regular sine curve.

The PIN photodiode can be complemented by a quadrant photodiode (QPD) in order to measure transverse displacements of the bead in the SWOT with the presence of the external

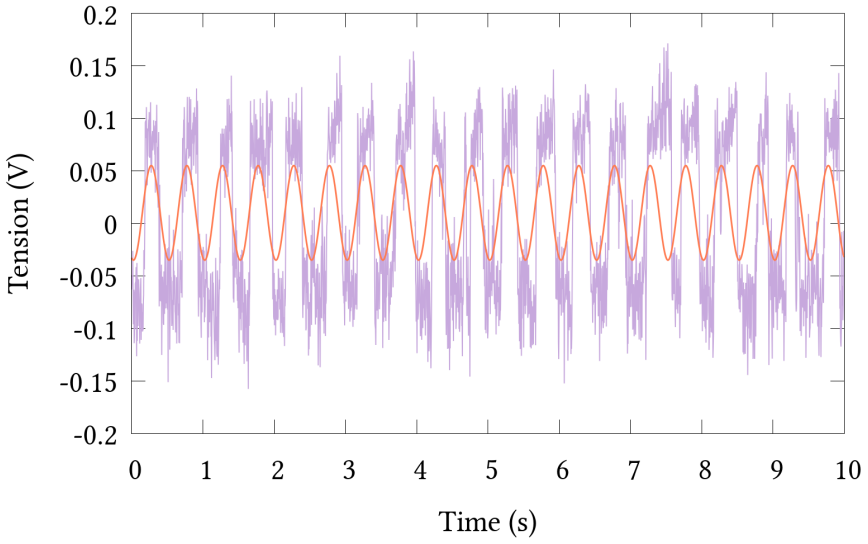

Figure 4.17: Experimental time-trace of 10 s recorded by the PIN photodiode. A 1 µm melamine bead is trapped in a bistable potential under an external drive at 2 Hz. The bead dynamics is strongly synchronized with the external displayed in orange.

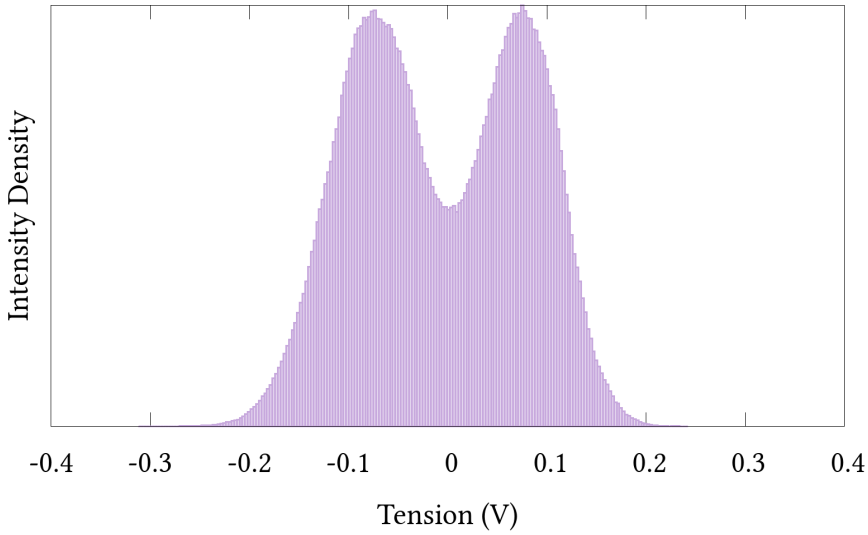

Figure 4.18: Histogram associated with the intensity time trace presented on Fig. 4.17. This histogram shows two regions of high intensity associated with two attracting positions for the trapped bead. Each attractor is considered as a metastable state populated by the bead. Both metastable states are approximately equally populated, the bead spending half of its time in each states.

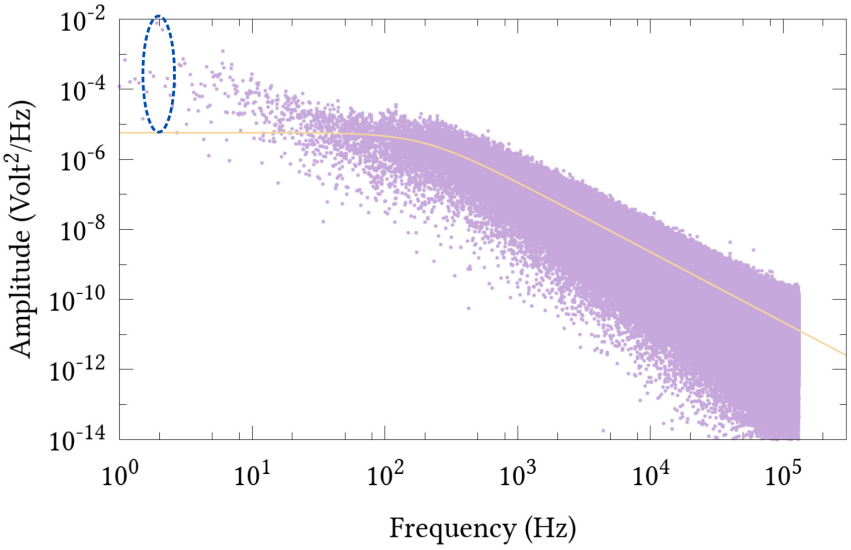

(a)

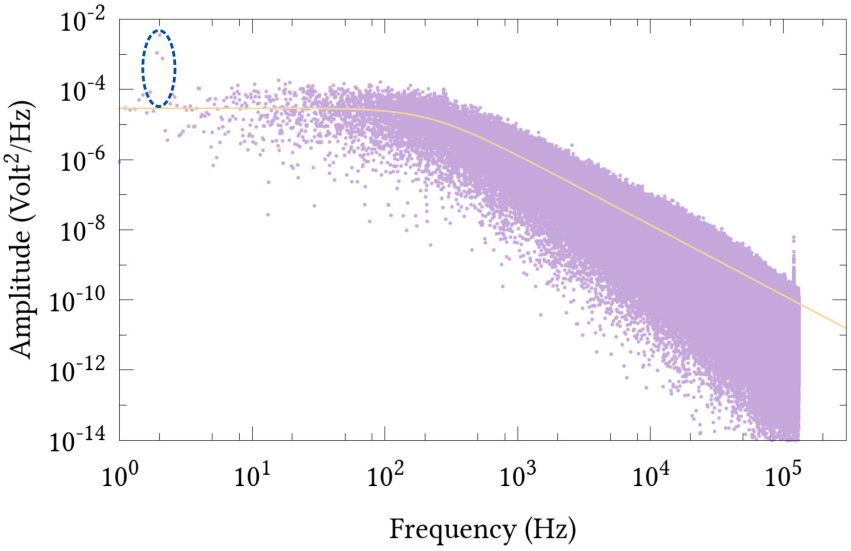

(b)

Figure 4.19: Power spectral density of a 1µm melamine bead trapped in a bistable potential under the influence of an external sinusoidal drive at 2 Hz. Panel (a) displays the PSD calculated from the PIN signal. Panel (b) the transverse PSD acquired via the QPD.

drive. The transverse PSD is shown in panel 4.19b.The curve follows a proper Lorentzian shape, even at low frequencies. This suggests that the overall transverse dynamics is similar to the one of a bead trapped in a harmonic potential.

Interestingly, the presence of the driving force is clearly seen on the PSD as a peak at 2 Hz in both longitudinal (z-axis)

and transverse PSD traces. The sharp character of the peak insures that this contribution does not come from the bistable dynamics itself, in which case one would expect a broader response. It is however unclear whether the strength of the signal originates only from the bead displacement in the trap or whether some of the contribution to the spectral density at 2 Hz could come from cross-talks between the acquisition channels used on the NI acquisition card (one channel for the PIN signal, two others for the x— and y—QPD outputs). The acquisition card works in a time-shared mode when performing multiple channels acquisition, in which case cross-talk must be accounted for. It is estimated that cross-talks can contribute to the signal up to 1/100 - 1/50 part of it. While it is expected that the strong drive has an impact and a signature on the transverse displacements spectral signature, all the sources contributing to that amplitude are difficult to determine. Looking at the amplitude of the peak in both panels 4.19a and 4.19b, taking the lorentzian shape as a reference, we estimate that the peak reaches ca. 3 orders of magnitude along the optical axis and ca. 2 transversely, i.e. typically a 1/5 ratio between the channels, from which we cannot exclude any cross-talk effect.

4.4.4 *Mandel* Q *factors*

Similarly to what we did numerically, we now analyze the evolution of the experimental Mandel factors associated with each of the metastable states as a function of the driving frequency f_d, for a fixed driving amplitude. The 639 nm pushing laser induces on the bead an external force

$$F_P(t) = F_{DC} + F_{AC}\sin(2\pi f_d t) \tag{4.24}$$

where F_{AC} corresponds to the driving amplitude. The experimental determination of both DC and AC amplitudes is presented in the Appendix B with the results that $F_{DC} \simeq 2$ pN and $F_{AC} \simeq 700$ fN.

We start the experiment with an unperturbed symmetric bistable rest potential -displaying an histogram similar to the one presented in Fig. 4.18. As we explained in subsubsection 4.4.2.1, the rest potential is induced with the DC component of the pushing force acting on the bead (i.e. the pushing laser is not yet modulated). We carefully adjust both the pushing laser intensity and the end-mirror position in order to

have equal mean residency lifetime in both metastable states with $\tau_{up} \simeq 0.27$ and $\tau_{down} \simeq 0.29$ s (natural Kramers mean residency time). The associated Kramers natural frequency is 3.7 Hz and 3.5 Hz respectively.

The rest potential is also characterized by the associated Mandel factors Q_{rest} which, despite the fact that $\tau_{up} \simeq \tau_{down}$ are not identical for both metastable states. In such non-driven conditions, we measure $Q_{rest,up} \simeq -0.7$ and $Q_{rest,down} \simeq -0.6$. These negative values denote an initial tendency to bunch the residency time in both metastable states. This stems from a combination of effects: first, the potential walls are not harmonic, so that the restoring force is not linear with respect to the potential wells. Then, in our configuration, the potential depth lies at the limit of a clear separation of time necessary to apply Kramers formalism. It turns out indeed that the characteristic time, associated with metastable state changes, is only slightly longer than the relaxation time inside each metastable states. The dynamics of our rest potential is similar to the one simulated in Fig. 4.3c, corresponding to a moderately deep bistable potential, where state changes are readily observed but with a negative small Q factor (Fig. 4.6).

Considering the relative uncertainty associated with the determination of Q, both value are close.

In such resting conditions, we modulate the pushing laser around its DC value and record the evolution of the Mandel factors $Q_{up/down}$ as a function of the driving frequency. Lists of residency times for both the upper and lower states are formed, and when multiple acquisitions are validated (in the sense of subsection 4.4.3) with the same external drive frequency, their values are concatenated to form larger lists. This helps in reducing the experimental uncertainty. The results are presented in Fig. 4.20.

The evolution observed experimentally is well consistent with our numerical simulations of Fig 4.8. The experimental error bars are given by the relative uncertainties of the Mandel Q factors computed from the number of state transitions recorded. Considering a pool of N independent residency times, the relative uncertainty of both the mean and the variance is set to $\frac{1}{\sqrt{N}}$ of their value. Using the propagation of errors formula for product [81], the uncertainty becomes

$$\frac{\delta Q}{Q} = \sqrt{\left(\frac{1}{\sqrt{N}}\right)^2 + \left(\frac{1}{\sqrt{N}}\right)^2} = \sqrt{\frac{2}{N}}. \tag{4.25}$$

Note that the errors are computed assuming the independence of the measured values (mean residency times) in throughout the recorded series. But this is not was is observed experimentally. For that reason, we can only provide error estimates.

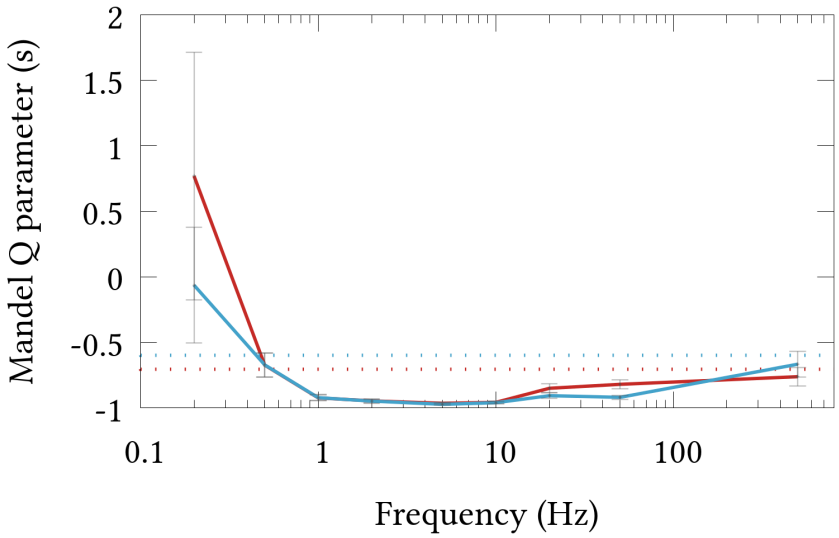

Figure 4.20: Evolution of the Mandel Q factors for the upper and lower state residency times. A 1 µm melamine bead is trapped in a rest symmetric bistable potential and the frequency of the external drive is changed while the amplitude remains constant. The blue curve represents the lower state and the red curve the upper state. The dotted lines display, in the same color code, the values $Q_{rest,down} \simeq -0.6$ (blue) and $Q_{rest,up} \simeq -0.7$ (red) of the rest Mandel factors.

Within the error bars, both the upper and lower curves show similar values which separate, as expected from the simulations, three distinct regimes:

- At low frequencies, it is difficult to prove that the super-poissonian regime is reached, considering the large error bars. These large error bars are due to the small number of state changes that can be recorded over only two periods in a 10 s-long experiment at a driving frequency of 0.2 Hz. Only ca. twenty transitions where extracted in total from the acquisitions. This small number naturally gives a large relative uncertainty. Nevertheless, it is clear that the dynamics of the bead is starting to be rectified by the drive, with Mandel Q factors at 0.2 Hz significantly larger than the rest ones.

- At frequencies associated with the Kramers mean residency time (around 2 Hz), the Mandel Q factors of both states are minimal and approach -1. In this regime

the Q factors are much below the rest values obtained without external drive. As clearly seen, the presence of the external drive causes a strong synchronization of the bead dynamics with the drive. Remarkably, both up/down curves have similar values in the synchronization regime. More precisely, we measure minimal Qs at 5 Hz, with values below −0.96 s for both curves. At 5 Hz, the associated mean residency time (in case of a perfect synchronization) is expected, from eq. (4.4), to be 0.1 second, that is three times shorter than the values obtained in the rest potential (without drive). This clearly illustrate the frequency blue-shift associated with the maximum of synchronization that we predicted under strong drive conditions in Fig. 4.10.

- At high frequencies, the Q parameters tend to the rest ones. The dynamics start becoming transparent to the external drive, with a bead that does not follow the external drive anymore. Working below the kHz, it does not seem that we can observe any signature of a non-adiabatic coupling between the external forcing and the bistable potential.

It is interesting to stress that our experiments confirm another effect that our simulations have revealed (see subsection 4.3.4): namely that the minimal mean residency time is reached at a higher frequency than the maximum synchronization frequency. This is clearly visible in Fig. 4.21 which gathers the mean residency lifetimes of both metastable states as a function of the external drive frequency. The minimum of mean residency time is obtained around 10 Hz in both states, clearly above the maximum synchronization frequency. At low frequencies, in the rectified regime, the mean residency lifetimes increase above the rest mean residency lifetimes in both states, while at high frequencies, they progressively approach the limiting rest values of the transparency regime.

4.4.5 *Time-traces and time delay analysis*

All these properties that we have been discussing are directly visible on the intensity time-traces experimentally acquired for different drive frequencies. Fig. 4.22 gathers some of the analyzed time-traces.

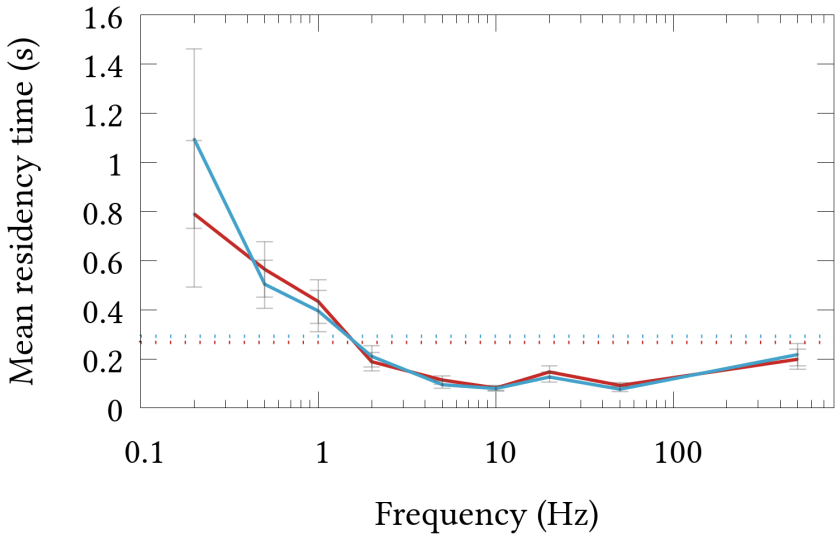

Figure 4.21: Evolution of the mean residency lifetimes of both metastable states as a function of the driving frequency, in the same conditions as in Fig. 4.20. The blue curve represents the lower state and the red curve the upper state. Dotted lines (same color code) display the mean residency lifetimes in the rest potential.

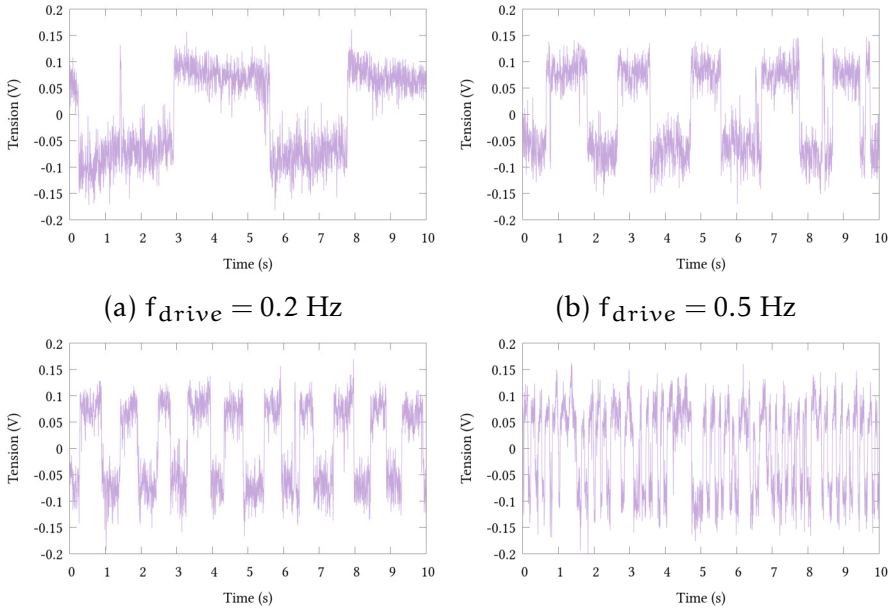

(a) $f_{drive} = 0.2$ Hz (b) $f_{drive} = 0.5$ Hz

(c) $f_{drive} = 1$ Hz (d) $f_{drive} = 5$ Hz

Figure 4.22: Experimental time traces of 10 seconds with different external drive frequencies.

Periodic components are clearly apparent in these time-traces. In particular, we see that transitions between metastable states only occur at specific instants with respect to the drive. This behavior is readily visible on panel 4.22b and even panel 4.22c where the bead quite strictly follows the external drive.

A Mandel Q factor provides a good measure on the level of synchronization. Nevertheless, it becomes less efficient for understanding how synchronization emerges from the external drive. Panel 4.22d gives a clear example of these limitations. At this driving frequency, we observe (for instance in the 4-5 s time interval) that the bead can miss a jump with respect to the drive frequency. The mean residency time distributions will witness an increased spread in the lifetime value. But looking at the trace, it seems that after a few missed jumps, there is a high probability to jump in the next period of the drive. The Mandel Q factor cannot characterize this behavior. Here, one has to resort to the approach described in subsection 4.3.5 where one monitors the evolution of the time delays between successive transitions of the same kind.

Just as exposed in that Section, we now adopt the time-delay point of view and build the histograms of the probability of state changes of the same kind (see above) as a function of the number of drive periods. These histograms are plotted in Fig. 4.23 for driving frequencies ranging from 0.2 to 50 Hz.

The absolute phase difference [86] between the drive and state changes was not studied here.

- At low frequency (panels 4.23a 4.23b) no state transitions is observed after one drive period. As is expected from the notion of rectification, the bead can hop between metastable states many times before a drive cycle is completed, i.e. hop many time per drive but for short times only. In other words, the bead follows the slow drive and the transition to the other metastable state are short lived. This is exactly what the simulations revealed (see Fig. 4.12). The only difference is that, experimentally, the small number of transitions available over the time of the experiment (10 s) makes the histogram badly defined. Nevertheless, the sharp cut above T is perfectly clear. For a drive frequency of 0.5 Hz, one third of the transitions occurs around one drive period of time and the rest is distributed at shorter times only.

- For driving frequencies at 1 and 2 Hz (panels 4.23c and 4.23d), we clearly observe the strongest tendency for the bead to change state every drive period exactly, with most

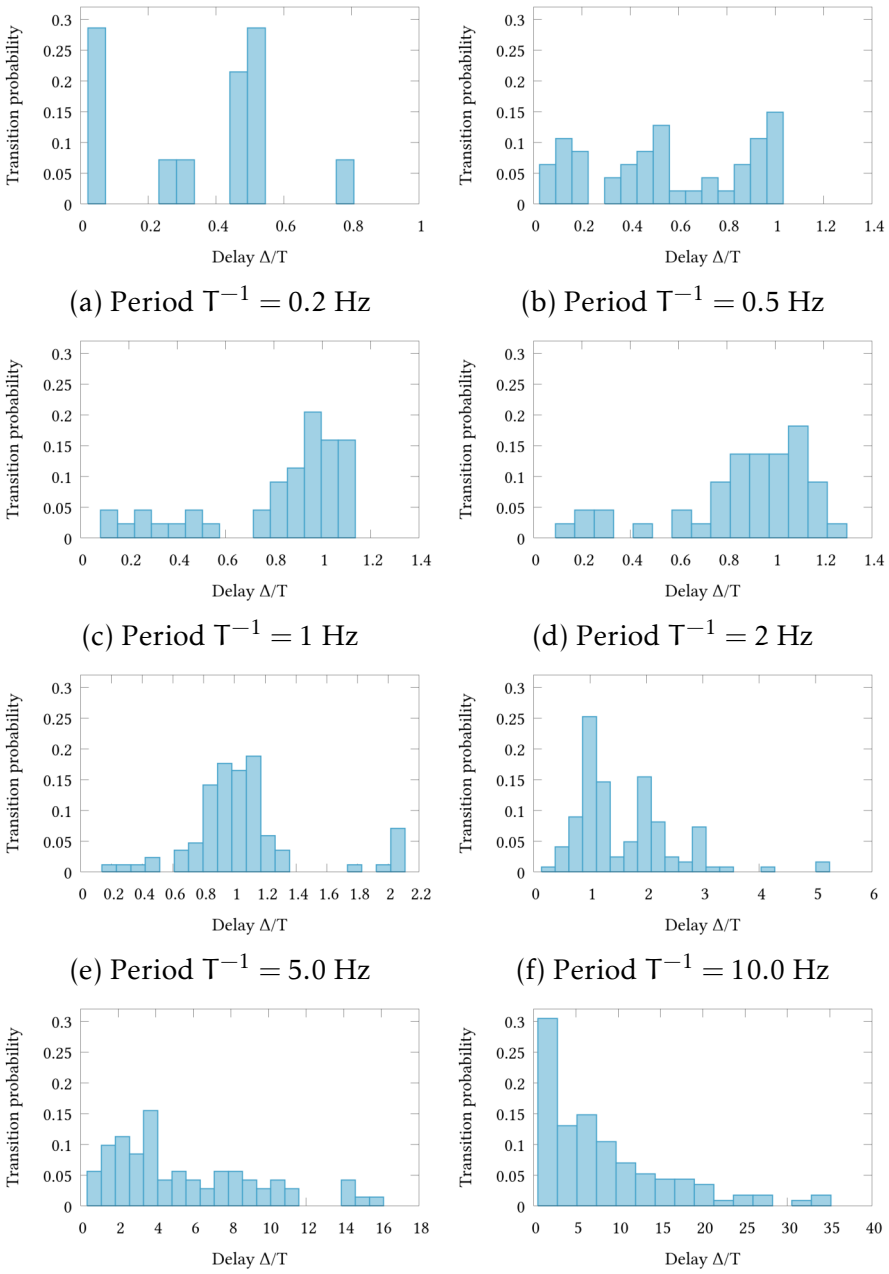

(a) Period $T^{-1} = 0.2$ Hz

(b) Period $T^{-1} = 0.5$ Hz

(c) Period $T^{-1} = 1$ Hz

(d) Period $T^{-1} = 2$ Hz

(e) Period $T^{-1} = 5.0$ Hz

(f) Period $T^{-1} = 10.0$ Hz

(g) Period $T^{-1} = 20.0$ Hz

(h) Period $T^{-1} = 50.0$ Hz

Figure 4.23: These histograms show the transition probabilities for state changes of the same nature (down to up) as a function of the number of drive periods. The time τ between successive state changes is normalized by the drive period. Very strong synchronization is observed (Fig. 4.23c, 4.23d) then partial synchronization emerges with increasing frequencies (Fig. 4.23e, 4.23f) before progressively losing the synchronization with broad transition probabilities (Fig. 4.23h).

of the transitions centered around 1. Remarkably, there is a strong depletion of the short-time distribution without any harmonic structure. This corresponds to the regime of "complete synchronization" with very low Q factors at high forcing amplitude (see our diagram 4.7). Note that "perfect" synchronization would be associated with negligibly small spread around 1.

- Interestingly, the smallest Mandel Q factors have been measured for a drive period of 5 Hz. The associated histogram, displayed in panel 4.23e, reveal that, while almost all the probability density is sharply distributed around 1 -as expected in a complete synchronization regime- few transitions are occurring outside the first drive cycle. These transitions do not occur randomly since they clearly peak at $2 \times T$. This means that the rare occasions where the bead "missed" its jump with the external drive, it waits for the following cycle to effectively perform the transition between the metastable states. It is important to emphasize that an analysis purely based on a Mandel factor approach would have missed this important possibility of the synchronization dynamics. We note that a similar behavior has been reported by Libchaber *et al.* [7].

- This catch-up behavior after a missed drive cycle is much more clearly seen in panel 4.23f with an external drive of 10 Hz. At this drive frequency, the bead can change state up to 5 drive cycle after the previous one. Transitions remain well synchronized with the drive, not only at its fundamental period but also at multiples of the drive period. The most remarkable feature is that the probability of changing state outside of the appropriate drive "wave" becomes very small. These experimental observations are confirming our simulations presented in panel 4.12c.

- Increasing further the external drive frequency leads to the regimes of transparency where the bead is desynchronized, losing any periodicity in its state transition time delays with respect to the drive (panel 4.23g). At high frequencies above 50 Hz, the distribution gets closer to a Poisson distribution (panel 4.23h). It is not obvious, in particular from the Mandel analysis in Fig. 4.20, that this distribution can be taken as an indication of the non-adiabatic regime.

4.5 CONCLUSION

In this chapter, we have studied the regime of an externally driven bistable potential. Considering the stochastic evolution of the bead within the bistable potential, an external periodic forcing can lead to the phenomenon of stochastic resonance as described from a synchronization point of view. The conditions under which such a phenomenon can be observed in our optical piston setup have been carefully studied in this Chapter.

In our optical piston setup, the external forcing can be performed in two ways:

- by putting the end-mirror of optical piston into periodic motion. This amounts to define a driving potential which eventually depends on the instantaneous position of the bead. The forcing has thus a parametric nature
- by exerting on the bead an external, modulated, force. In this situation, the forcing can merely be derived from a time-harmonic potential, with no dependence on the bead position.

Starting with a Langevin equation and a standard model for bistability, the Duffing potential, we study numerically the phenomenon of stochastic resonance by adding an external periodic force. We carefully look at the evolution of the statistical properties of the residency lifetimes in both metastable states as a function of the drive frequency and amplitude. This leads us exploring different statistical regimes:

- for a weak drive: going through a regime of rectified bistability at low frequency, a regime of partial synchronization at a frequency close to the natural Kramers frequency, and a regime of transparency at higher frequency,
- for a strong drive: going through an adiabatic regime of strong rectification, a regime of full synchronization at the Kramers frequency, and a regime of non-adiabatic coupling at high frequency.

We exploit for this detailed analysis an efficient tool for characterizing the residency lifetime distributions: the Mandel factor. This factor describes the onset of correlations in the statistics and enables us looking in particular at the onset of ergodicity under the influence of the external forcing.

We also develop an alternative approach based on a transition time delay analysis in order to study the evolution of the probability distributions associated with the hopping events themselves.

In the second part of the Chapter, we gather the experiments that we perform in this context. Experimentally, the external forcing is induced by a pushing laser added to the optical piston. This pushing laser, that can be modulated in frequency and amplitude, exerts an optical force on the trapped, over-damped, bead.

For all our experiments, we took great care that the bistable potential is symmetric with the trapping and the pushing laser on before modulating the amplitude of the latter. This is an important condition in order to be able to compare the different experimental results in the different conditions of drive.

Using the same methodology of the Mandel factor and the time delays, our experimental results turn out to be in good agreement with our simulations. We demonstrate the regime of rectification, and even reached the regime of complete synchronization. At high forcing frequencies, harmonics in the state change transition probability histograms are observed, corresponding to missed state transitions. These signatures are present up to the level of desynchronization reached at higher frequencies.

5

EXPERIMENTAL DEVELOPMENTS AND PERSPECTIVES

The experiments on stochastic synchronization performed in Ch. 4 have led to improve our optical piston configuration with respect to the experiments done in Ch. 2 and 3. Essentially, we have implemented a control of the position of the piston end-mirror at a nm level of accuracy. We have also added in the setup a second laser (called below the pushing laser) in order to be able to perform experiments in the presence of an external forcing. This forcing is induced by this second laser that exerts an optical force on the bead trapped in our SWOT.

This is precisely here that our setup meets one important topic in optical tweezing: high-resolution force measurements. Optical tweezers have indeed revealed a unique capacity to monitor force fields in fluidic environments with a high level of resolution [87–89]. For force measurements, the state-of-the-art level of control on optical tweezers is such that optical trapping can compete with other types of methods, such as atomic force microscopy (AFM) [19–21].

One appealing aspect of our SWOT is the possibility to trap small metallic nanoparticles (NPs). We will exploit a remarkable feature of the SWOT. where the scattering forces induced on the NP immobilized on an anti-node of the standing wave pattern (induced by the reflection of the trapping beam on the end-mirror) actually stabilizes the trapping dynamics rather than ejecting the Au NP from the waist -as it would happen in the case on conventional single beam traps [42].

This possibility important in the context of force measurements because resorting to small NPs gives a way to reduce the Stokes drag, and hence an efficient way to improve force resolution levels. The metallic character of the NPs is also important when it comes to trap and push small beads in standard laser intensity conditions, ca. 10^{-2} mW $\cdot$ μm^{-2}. Metals give the possibility to tune the second laser, acting as a *pushing*

laser, at a maximum of the extinction cross-section, i.e. the possibility to overcome the limit set on optical force strengths by the R^3 dependence of the NP extinction cross-section. In this Chapter, combining these advantages of our optical piston, we will present a series of experiments that measure, in a fluid, optical forces on single Au NPs with a fN resolution.

We will finally show that our setup is ready for manipulating more exotic nano-scale metallic objects. Chiral Au nanopyramids fabricated in the group of Prof. D.J. Norris, at the ETH-Zurich are the perfect systems for demonstrating this. In this Chapter, we will trap single chiral nanopyramids and we will propose an experimental polarization analysis strategy that enables the recognition of the enantiomeric form of the optically trapped single chiral object.

5.1 INTERFEROMETRIC SCATTERING MICROSCOPY

Trapping small objects however leads to some difficulties. With sizes below the diffraction limit, it becomes hard to get any reliable information by simply looking at the recollected intensity of the SWOT beam -as it was done for the large polysterene or melamine micron-sized beads of Ch. 2, 3, and 4. At these sizes with our standard method, it becomes practically impossible to determine the actual number of objects inside the trap. Depending on the stability of the colloidal dispersion, various types of aggregates can be formed that can all be trapped, stressing the importance of being able to discriminate between them all.

One interesting approach that can help in overcoming these difficulties is the so-called interferometric scattering microscopy (iSCAT), as developed in particular in the group of Prof. V. Sandoghdar [90–92]. We have therefore equipped our SWOT setup with an iSCAT imaging line, as described in Fig. 5.1. This addition consists in a third laser focused, at low power, at the back focal plane of an objective behind the dichroic mirror. This allows to have this third beam almost like a plane wave between the two objectives. The interference formed between (i) the partial reflection of a transmitted plane wave at the dichroic mirror / water interface and (ii) the field back scattered by an object in the fluid is imaged on a CCD camera.

The interference process is schematized in panel 5.2 (a). A scatterer is illuminated (from below) by a plane wave E_i. A

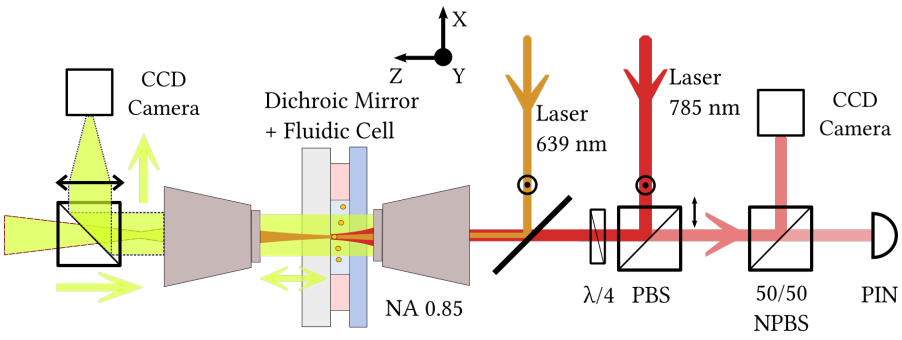

Figure 5.1: Schematics representation of the experimental addition of the iSCAT imaging line. A laser beam at 594 nm (50 mW, Excelsior, Spectra Physics) is focused at the back focal plane of an objective (NA 0.6, 40×) behind the dichroic end-mirror of our SWOT. The power of this laser is reduced down to 15 μW. A fraction of this light is scattered back at the mirror/water interface and another fraction from the trapped NP. These scattered beams are sent back to a CCD camera for imaging and tracking.

fraction of this light is reflected at the glass/water interface forming the backward propagating reference field E_r. Some of the transmitted light is also back scattered by the illuminated object as E_s. The two backward propagating fields E_r and E_s interfere.

As for any interfering setup with two beams, 3 terms are involved when computing the resulting intensity (imaged on the CCD camera). The first term is the constant and dominant contribution $|E_r|^2 = |r|^2|E_i|^2$ coming from the reflection of the incident beam on the mirror's interface, characterized by a reflection amplitude r. A second term arises from the field $E_s = sE_i$ scattered by the trapped object. Because $|s| \ll |r|$, this term is considered as a negligible second-order term in $|s|/|r|$. The cross-term however, stemming from the interference between E_r and E_s, is a first-order term. It is this term that yields the relevant iSCAT signal. The intensity measured on the camera then writes as:

$$I_{iSCAT} \propto |E_i|^2(r^2 - 2r|s|\sin(\phi)), \tag{5.1}$$

with ϕ the phase between the two interfering fields.

The iSCAT approach offers a label-free detection of objects in the fluid against a bright background (contribution from $|r|^2|E_i|^2$). It turns out to be an extremely useful technique that

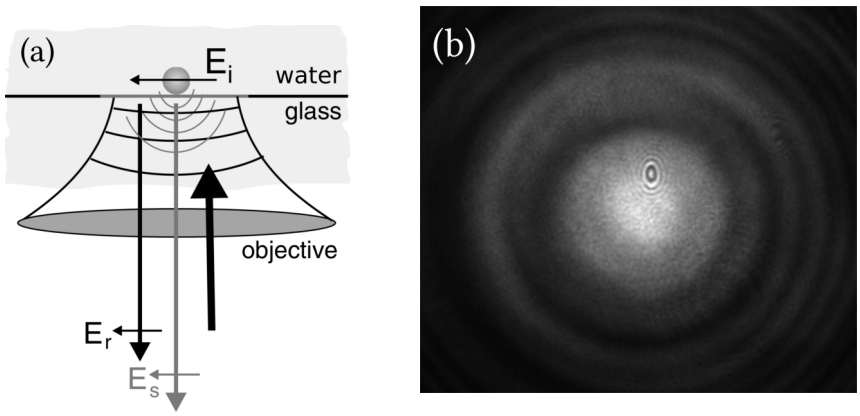

Figure 5.2: (a) Schematic representation of the iSCAT detection scheme. A scatterer is illuminated (from bellow) by a plane wave. A fraction of this light is reflected at the glass/water interface. Some of the transmitted light is also backscattered by the illuminated object. The two fields E_r and E_s, propagating backwards, interfere. Schematics adapted from [90]. (b) CCD image taken on our optical steup, for a 1 µm melamine bead, diffusing in water. The presence of the object is clearly seen by the contrast localized on the background light.

helps in determining the size of an object dispersed in the fluid through (i) the size of the imaged spot and its contrast, and (ii) through the blinking dynamics of the image on the CCD video, which strongly depends on the size of the object. Small objects, with large average diffusion rates, will span the phase ϕ -a function of the distance between the object and the mirror surface- through diffusion more rapidly than larger ones.

The iSCAT technique is very useful in our experiments at the level of dielectric beads which provide a strong phase contrast. Polystyrene, melamine and silica beads have been used throughout our experiments and iSCAT actively helped in all of them. An illustration of a diffusing particle observed with our iSCAT microscope is presented in panel 5.2 (b). It shows a 1 µm melamine bead in water, diffusing nearby the surface. The contrast and the visibility of the object is sharp and much better defined than with a simple bright field imaging approach.

Exploiting the informations brought by the iSCAT method has turned out to be very important when dealing with small moving metallic scatterers, just as in our optical force experiments described in the next Section. It has indeed given

us a valuable tool in order to "diagnose" the quality of our metallic NP dispersions. For recollected intensities from the SWOT measured as identical on the PIN photodiode, iSCAT helps determining the nature of the trapped object in the trap, as well as counting how many objects are actually trapped. This capacity has allowed us to use Au NP dispersions at low concentrations, which is important for reducing the probability of having aggregates formed in the dispersion too rapidly.

The iSCAT technique is offering a straightforward way of doing the experiments: the imaging configuration enabled us going literally "fishing" by moving the sample holder with the piezo actuators. Note however that this simple approach only works for experiments that are not alignment sensitive. A shift of the sample position, changing the reference distances along the optical axis, can cause slight offsets between the different beams that can become detrimental.

5.2 HIGH-RESOLUTION OPTICAL FORCE MEASUREMENTS

Very recently, Lui and colleagues [20] have demonstrated the possibility to implement on an total internal reflection force microscope a detection strategy analogous to dynamic mode (DM) atomic force microscopy which has been extensively used in the context of weak force measurements [93]. In a DM operation, the external force is modulated at a fixed frequency f_0 and the amplitude of the signal is measured with a lock-in amplifier driven at the modulation frequency. The DM is particularly interesting in the context of weak force measurements since it can yield a better sensitivity, in particular as far as $1/f$ noise limitation is concerned. Using this method, Lui *e*t al. have have measured forces exerted on optically trapped dielectric particles by an evanescent field down to 7 fN, with an error smaller than 1 fN for the smallest (0.5 μm diameter) dielectric beads [20].

We propose here to push the resolution of DM optical trapping further down and to improve the experimental sensitivity in force detection. These improvements are reached by combining three intertwined ingredients:

- Our SWOT allows trapping a single Au NP of radius $R = 75$ nm in a stable way. As already stressed above, it is important for such experiments to be able NPs as small as possible in order to reduce the Stokes drag.

- Our SWOT allows trapping in stable conditions small objects that offer an extinction cross-section as high as possible. With low extinction cross-sections, dielectric NPs are not ideally suited when performing optical force measurements in standard laser intensity conditions. Metallic NPs, and Au NPs in particular, are much better probes, particularly when the pushing laser is tuned to the extinction cross-section maximum.

- Our SWOT is characterized by a spectral response such that it is possible to reject the modulation frequency f_0 far away from the roll-off frequency f_T of the trap.

A radius of $R = 75$ nm for an Au NP is a compromise between these three ingredients: the Stokes drag reduction argument, the limit set on optical force strengths by the R^3 dependence of the NP extinction cross-section, and the trap stability condition determining an appropriate roll-off frequency. As we will calculate below, this combination directly leads to optimizing the thermally limited force resolution of the SWOT in the DM operation.

5.2.1 *Mie cross-section evaluations*

Our experiments consist in illuminating a trapped NP with a pushing laser in order to exert an optical force on the NP independently from the restoring force at play inside the SWOT.

One difficulty when dealing with a single small object, is to reach, despite its small size, a good extinction cross-section with respect to the pushing beam. A Mie calculation is performed to determine the optimal wavelength to use for an optical force experiment. The results of the calculations [94–97] for an Au nanospheres of radius of $R = 75$ nm (assuming an incident plane wave) for the absorption, scattering and extinction cross-sections are displayed in Fig. 5.3.

The extinction maximum is around 640 nm and its contribution mainly comes from the scattering of the incident light field. The wavelength chosen at 639 nm for our pushing laser is therefore optimal for this experiment, leading to a maximized force at a given intensity with minimal heating (minimal absorption cross-section).

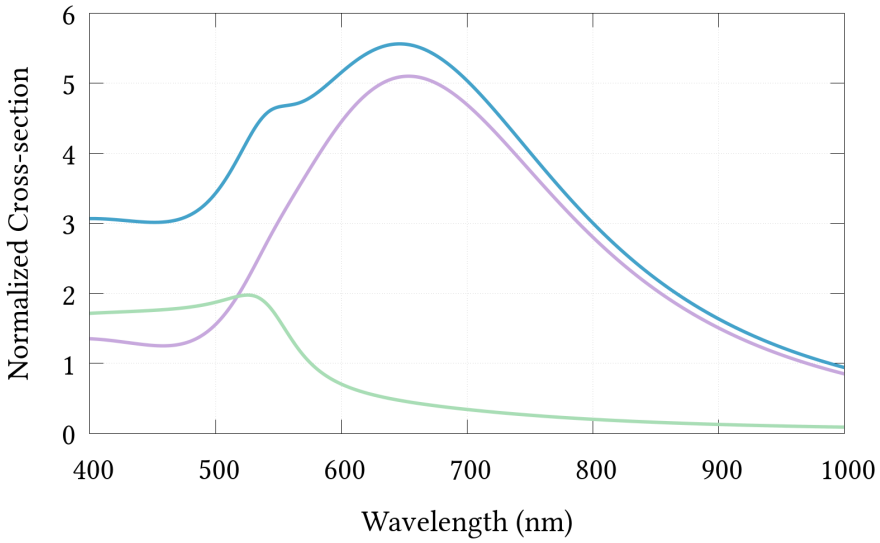

Figure 5.3: Cross-sections for absorption, scattering and extinction calculated for a R = 75 nm Au sphere as a function of wavelength computed using the Mie theory. They are normalized to the sphere diameter.

5.2.2 *Experimental setup*

A schematics of the setup is shown on Fig. 5.4 where, as discussed in CH. 4, the end-mirror of the SWOT is replaced by a dichroic end-mirror such that the trapping laser at λ_T = 785 nm is reflected, while the pushing laser - tuned at λ_P = 639 nm- is transmitted. The trapping beam goes through a water immersion objective and forms the SWOT by reflection on the dichroic mirror. The trapping laser reflected intensity is recollected and sent to a PIN photodiode. As always, the instantaneous motion of the bead inside the trap is monitored from the recollected intensity modulations. The pushing laser at 639 nm is injected along the optical axis using a 45° dichroic mirror transparent to the trapping beam. This 639 nm beam pushes the bead along the optical axis without trapping it (see Ch. 4), thus not perturbing the SWOT dynamics. To avoid any possible intensity signature of the modulated pushing beam on the PIN signal, an additional high-pass filter at 650 nm is added.

The experiment is performed on an Au NP with a diameter of 150 ± 15 nm (i.e. taken from the same commercial mono disperse suspension). The NP is illuminated by the pushing laser, focused slightly behind the trap position. The pushing beam does not overfill the objective entrance pupil, so that the effective NA at the output of the objective is reduced. In such

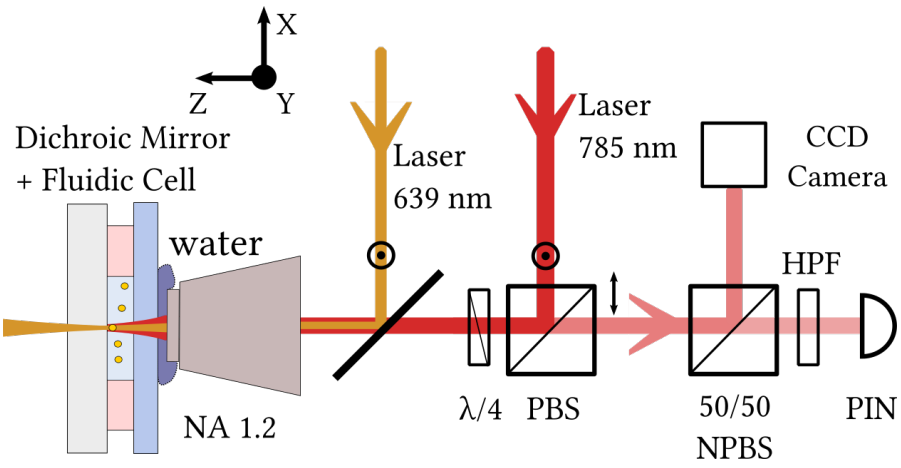

Figure 5.4: Schematics of the experimental setup. A SWOT optical trap is formed by a water immersion objective (NA 1.2, 100×) on top a dichroic mirror (cut-off at 700 nm). Gold nanospheres are trapped by a near IR laser (785 nm, 45 mW Excelsior-Spectra Physics laser diode, optically isolated). The recollected reflection carries the displacement signature of the object in the trap and is sent to a PIN photodiode (Thorlabs det10A70 mW) and recorded. A second beam (639 nm, 70 mW Thorlabs laser diode) is injected along the optical path using a 45° dichroic mirror (cut-off at 710 nm), transparent to the trapping beam. The 639 nm beam is used to push the bead along the optical axis. To avoid any intensity signature of the modulated signal on the photodiode, a high-pass filter (HPF) at 650 nm is added. The iSCAT microscope is not shown here. The setup is similar to the one in Ch. 4, with however melamine beads are replaced by Au nano-spheres.

situations, both gradient and scattering forces are at play but it is crucial to stress that the pushing laser never traps the NP and thus never perturbs the SWOT dynamics. The control on the pushing laser focalization on the NP is a simple way to tune the intensity flow incident on the NP and therefore the strength of the acting optical force with similar laser amplitude modulation levels.

5.2.3 *Trap susceptibility*

Fig. 5.6 displays the measured PSD $S_z[f] = |z[f]|^2$ associated with the overdamped axial displacement $z(t)$ of the NP described inside the SWOT by the spectral Langevin equation $z[f] = \chi[f]F_{th}[f]$ where $\chi[f]$ is the mechanical susceptibility of the NP inside the trap and $F_{th}[f]$ the Langevin force responsible for the Brownian motion of the NP.

Assuming that the response is harmonic, the susceptibility is Lorentzian with

$$\chi[f] = \frac{1}{\kappa_T - i2\pi\gamma f}. \tag{5.2}$$

At thermal equilibrium, the Langevin force spectral density is given by the fluctuation-dissipation theorem with [98],

$$S_{th}[f] = -2k_B T\, \mathrm{Im}(\chi^{-1}[f])/f = 2\pi k_B T\gamma. \tag{5.3}$$

We fit the PSD with this Lorentzian susceptibility and hence extract the roll-off frequency of the trap $f_T = 1300$ Hz.

This provides a thermally limited spatial resolution $\delta z = \sqrt{k_B T/\kappa_T} \simeq 20$ nm where $\kappa_T = 2\pi\gamma f_T$ is the trap stiffness determined from f_T and the Stokes drag $\gamma = 6\pi\eta R$, with $\eta \sim 10^{-3}$ Pa$\cdot$ s^{-1} the dynamical viscosity of water at room temperature.

With a trapping position typically located at a few (ca. 3) microns from the mirror surface, such a distance for the positional fluctuation of the bead within the SWOT is important to reach in order to be able to neglect any z-dependent surface-induced Faxen-like correction to η [33].

5.2.4 *Allan variance analysis*

As emphasized already in Ch. 4, the limits of stability of the whole experimental setup in standard conditions put a lower bound on the available bandwidth. This is particularly true in our experimental configuration where the interferometric nature of the SWOT trap makes it very sensitive to all external perturbations such as flow drift and evaporation inside the fluidic cell, uncontrolled suspensions inside the cell, cultural noise, etc. Despite the fact that a single Au NP can be kept in the SWOT over a few minutes, the low frequency drift of our optofluidic system can impact the overall trap dynamics.

To measure the optimal data acquisition time, we evaluate from an Allan variance $\sigma_z^2(\tau)$ analysis, as presented in Ch. 4, the optimal measurement time t_{opt}. As seen in Fig. 5.5, this minimum falls at $t_{opt} \sim 10$ s for our system.

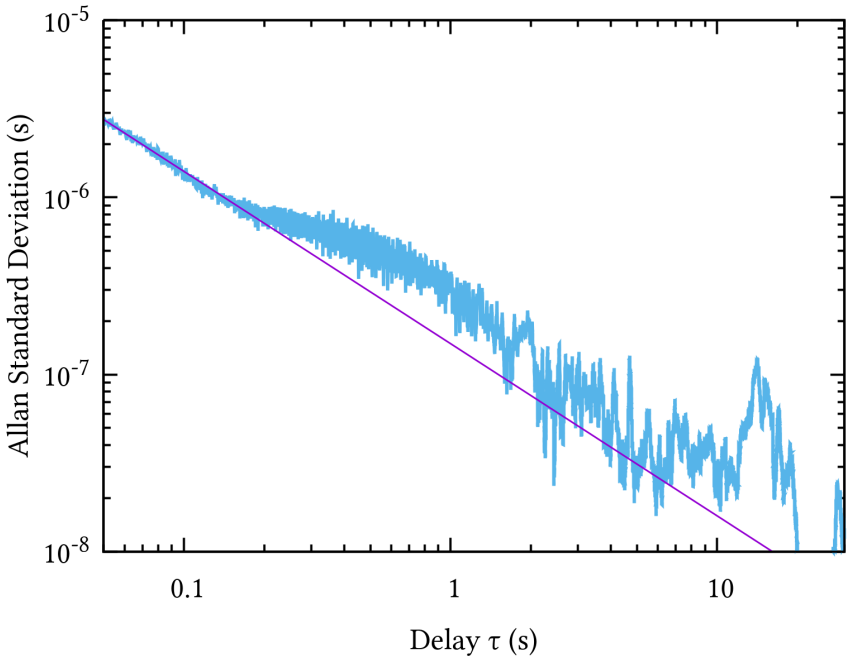

Figure 5.5: Allan variance evaluation for the trapped Au NP, following the procedure described in Ch. 4.

As a result, it is clear that the usual method for improving the experimental sensitivity by averaging a large number of measurements repeated throughout long acquisition times [99] can be counterbalanced by the drift of our system. It is therefore important here to work at the optimal acquisition time: the PSD shown in Fig. 5.6 has been recorded over t_{opt} and all our force measurements are performed with a corresponding bandwidth fixed at $\Delta f_a = 0.1$ Hz.

5.2.5 *Measuring optical forces*

In the DM operation of the SWOT, the pushing laser power is modulated at a frequency f_0 around a mean intensity value with $P_P = \langle P \rangle_t + P_{mod} \cos(2\pi f_0 t)$. We carefully isolated and verified that the modulation of the pushing laser at λ_P does not contaminate the recollected scattered signal at λ_T from which $z(t)$ is recorded. In such conditions, the overdamped

dynamics of the NP is therefore determined, in addition to the Langevin force, by a static (DC) force component F_{DC} -induced by $\langle P \rangle_t$- and a modulated (AC) force component F_{AC} related to P_{mod}. The spectral displacement then simply writes as

$$z[f] = \chi[f]\,(F_{th}[f] + F_{DC}\delta[0] + F_{AC}\delta[f - f_0])\,. \tag{5.4}$$

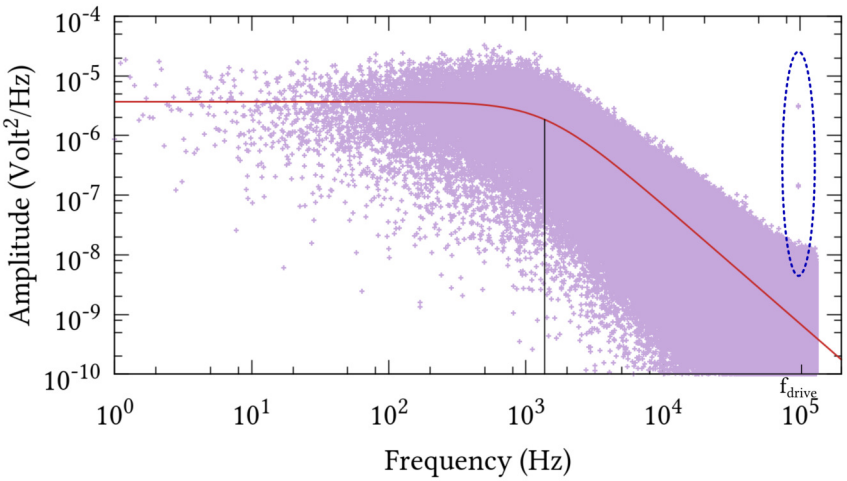

Figure 5.6: Experimental PSD acquired over τ_{opt}. The Lorentzian fit is shown in red. The external drive amplitude is associated with a modulation tension of 900 mV. It has a strong spectral signature around 97579 Hz. The height of the peak is large and well-above the signal variance. The spectral height of this contribution leads to a measure of the force via the trap calibration.

Experimentally, the output signal from the PIN photodiode is sent into our low noise preamplifier (SRS560) with a high-pass filter frequency at 0.03 Hz. This simply removes the DC component of the force from the signal. The PSD $S_z[f]$ then simply displays a resonant peak centered at the modulation frequency f_0 with

$$S_z[f] = \frac{1}{(f^2 + f_\Gamma^2)}\left(\frac{D}{2\pi^2} + \frac{F_{AC}^2}{16\pi^2\gamma^2}\delta\,(f - f_0)\right), \tag{5.5}$$

where $D = k_B T/\gamma$ is the diffusion coefficient. This approach has similar expression to experiments where an external drive is applied on the bead to calibrate the system [65].

The corresponding force resolution is limited by the PSD signal measured at the modulation frequency f_0 over a frequency bandwidth Δf that cannot be smaller than the optimal bandwidth $\Delta f_a = 0.1$ Hz determined from the Allan analysis. In a first series of experiments, we exert optical forces on the NP with sufficiently strong modulation amplitudes so that the peak amplitude associated with F_{AC} clearly emerges above the PSD noise level.

With amplitudes F_{AC} directly proportional to P_{mod}^2, we measure the power spectral intensity I of the peak in the PSD associated with the optical force. The spectral density associated with F_{AC} actually spreads over a few peaks I_i, i.e. over a slightly larger bandwidth with $\Delta f_{AC} = 0.4$ Hz. We convert each frequency contribution of the peaks I_i in $m^2 \cdot Hz^{-1}$ through a calibration factor β.

The calibration is done by fitting the experimental PSD by the Lorentzian model $|\chi[f]|^2$ which provides best-fitted values for D and f_T. From the diffusion coefficient calculated from the FDT (assuming known temperature and viscosity) $D_{FDT} = k_B T/\gamma$, the calibration factor is simply $\beta = \sqrt{D_{FDT}/D} = 1.5 \times 10^{-7}$ m $\cdot V^{-1}$. We are thus led to the force value calculated via Hooke's law $\delta F = -\kappa_T \delta z$ for each spectral contributions I_i

To properly measure forces, one has to use the onesided expression of the spectral density.

$$F_{AC} = \sum_i 2\sqrt{2}\pi(\beta\sqrt{I_i})\gamma\sqrt{f_0^2 + f_T^2}. \tag{5.6}$$

directly measured from the PSD written in Eq. (5.5).

The evolution of the measured force for different modulation amplitudes F_{AC} at the same drive frequency f_0 is given in Fig. 5.7. This force is extracted from the PSD peak at the drive frequency and shown as scattered red dots. Their distribution shows the expected linear evolution between the measured force and the modulation amplitude. Remarkably, the linear fit is consistent with the experimental force resolution determined above from the position noise measured on the PSD.

5.2.6 *Lock-in detection*

The PSD measurements already showed the advantage in measuring force signals at the modulation frequency f_0, improving through the low-pass response of the PSD itself the sensitivity level when $f_0 > f_T$. But a lock-in detection becomes particularly interesting to implement in a context where the

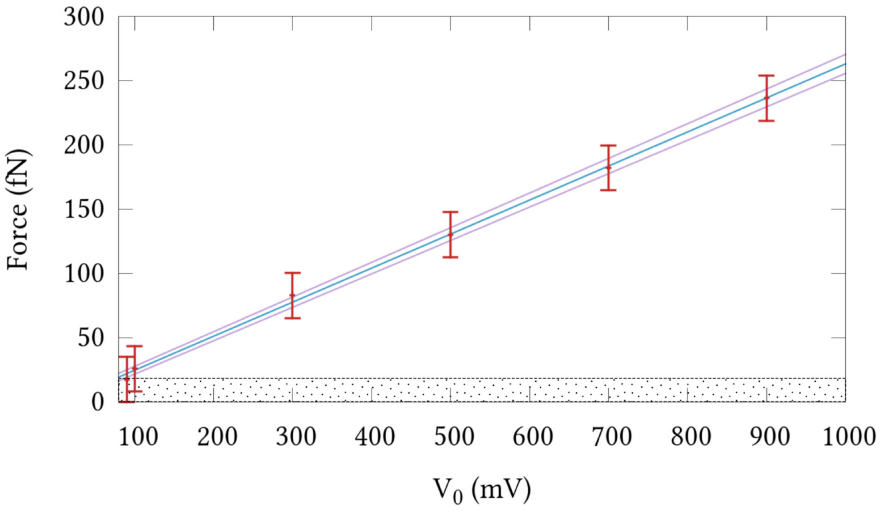

Figure 5.7: Evolution of the force measured by the intensity peak on the PSD at the modulation frequency f_0, as a function of the modulated pushing beam amplitude given by the function generator. The force is, as expected, linear with intensity variations. This method allows measuring directly the force above 50 fN. The error bars are given by the determined force resolution which gives the minimal force value that can be measured, as indicated by the long-dashed threshold line on the graph and a dotted area. The two additional lines (in pink) represent the error (at 1 standard deviation) associated with the linear fit of the points.

acquisition time is limited by the stability of the whole system. It will allow indeed detecting the modulated force signal below the noise level set by the PSD at f_0 with bandwidth limited to Δf_a.

The lock-in amplifier outputs a tension proportional to the sinusoidal amplitude measured in the input signal at a given reference frequency f_{ref}. It is basically a hardware and real time way to "select" the amplitude of the PSD peak. In practice the device performs a 0 delay temporal correlation between the input signal and a reference sinusoidal signal $S_{ref}t = \sin(2\pi f_{ref}t + \phi)$ (with frequency f_{ref} and phase ϕ). The resulting amplitude is then red out. The signal S_{ref} comes from the function generator driving the pushing laser, the phase being left to zero. The lock-in has the huge advantages that its resolution level will increase with the acquisition time, and that

the phase component in the signal allows extracting the force signal even below the PSD noise level, for the same bandwidth. This will immediately lead to improve the force resolution level.

The dynamical range of the acquisition card and the lock-in amplifier (SRS830) involved in these measurements is limited to 16 bits. In order to properly exploit them, it is important to send to the card only the signal of interest, i.e. the signature of the forces. We have implement a detection chain such that the signal at the output of the pre-amplifier is high-pass filtered (SRS, SIM965). The filter is a Butterworth 48 dB/octave high-pass filter with a cut-off at 40 kHz. The PSD below f_T is cut in order to remove from the time-dependent intensity signal all high amplitude contributions (the plateau seen on the full PSD). These high amplitude contributions are at low frequencies and they are removed from the time trace. With this filtering procedure, the position noise signal containing the force modulation signature can be spanned over the entire dynamical range of the devices.

In such conditions, we model the lock-in amplifier as a Lorentzian band-pass filter $\mathcal{L}[f]$ centered on the modulation frequency f_0 with a sufficiently narrow spectral bandwidth $\Delta f \ll f_0$ such that the position noise becomes $\delta z_{min} \sim \sqrt{\Delta f \cdot S_z[f_0]}$. Again, the position noise determines, via Hooke's law $\delta F = -\kappa_T \delta z$, the thermally limited force resolution of our DM-SWOT as

$$\delta F_{min} \sim \sqrt{\Delta f} \cdot \frac{f_T}{f_0} \sqrt{k_B T \gamma}. \tag{5.7}$$

From this relation, it becomes clear that the resolution can be improved (i) by modulating the external force at relatively high frequencies with respect the the SWOT roll-off frequency in order to minimize the f_T/f_0 ratio as much as possible, and (ii) by decreasing the Stokes drag γ -which we do by resorting to smaller objects. In typical conditions of trapping with $f_T = 1.3$ kHz and force modulation at $f_0 \simeq 97.6$ kHz (100 kHz is avoided because the laser diode becomes noisy at that precise frequency), our setup is characterized by a sensitivity as low as 2×10^{-2} fN/$\sqrt{\text{Hz}}$.

An important part of the experiment is to properly calibrate the lock-in output signal as a function of the modulation amplitude of the pushing laser. To do so, we calibrate the lock-in signal against the force values F_{AC} measured directly by the PSD approach (presented on Fig 5.7). In practice

the intensity recorded by the lock-in amplifier is measured simultaneously to the acquisition of the complete time-traces (at the same bandwidth). We verify that the lock-in response is indeed linear with the drive amplifier and from the forces measured on the PSDs, the associated lock-in scaling factor is extracted. We emphasize that the calibration performed above the PSD noise level remains operational below considering that the lock-in amplifier has linear response to the amplitude of the measured signal.

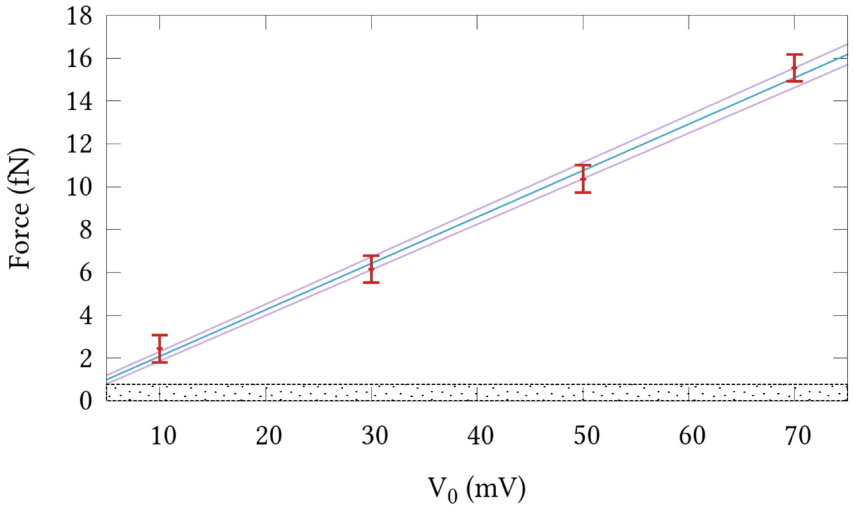

Figure 5.8: Evolution of the measured force through the lock-in amplifier as a function of the modulating amplitude of pushing beam. As expected, the force is linear with intensity variations and goes down to a measured value of 2 fN. Error bar are the recorded values from the error channels of the lock-in amplifier. The force detection threshold (computed from the error on lock-in) is shown by the dashed line. They give the standard deviation associated with the measurement done at one modulation tension. The two lines (in pink) represent the error (at 1 standard deviation) associated with the linear fit of the points.

The modulation amplitude of the pushing laser can be reduced even further while still measuring a proportional lock-in output tension. This output signal is converted, through the calibration, into a force signal. The measurements related to this experiment are presented in Fig. 5.8. In the optical configuration of the pushing laser focused on the NP, the

smallest modulation tension applied to the laser corresponds to forces below 5 fN. As seen from the graphs, the experimental resolution (smallest detectable force) is at the 2 fN level. Exploiting the error channel from the lock-in amplifier the experimental limit on the resolution of force measurement is ca. 0.6 fN. This value is consistent with the minimal value of the detected force (2 fN) here. It is associated with a displacement amplitude of 0.1 nm. Below this value, the detection noise of the lock-in dominates over the force noise, putting an experimental limit on the force resolution level below which the lock-in reaches its noise level.

The following table 5.1 summarizes for position and force, the levels of sensitivity and resolution at a $\Delta f_a = 0.1$ Hz bandwidth determined from experimental noise level measured on Fig. 5.6 or calculated from the theoretical position noise thermal limit at the driving frequency f_0 (Eq. (5.7)).

	$\sqrt{S_z[f_0]}$	$\sqrt{S_z^{exp}[f_0]}$	F_{AC}	$F_{lock-in}$
δz (nm/$\sqrt{(}$Hz))	4.3×10^{-3}	1.9×10^{-2}	8.6	0.33
δF (fN/$\sqrt{(}$Hz))	5.3×10^{-2}	2.4×10^{-1}	72	7.75
Δz_{min} (nm)	1.4×10^{-3}	6.1×10^{-3}	2.7	0.2
F_{min} (fN)	1.7×10^{-2}	7.5×10^{-2}	22.9	2.45

Table 5.1: Table summarizing the sensitivity and resolution obtained for the different methods presented. The smallest measurable force F_{min} shows an improvement of 1 order of magnitude compared to the PSD F_{AC} measurement. The object displacement Δz_{min} associated with the smallest measured force is at the ångström level.

5.2.7 *Experimental lock-in error*

The resolution of the lock-in is determined experimentally. Our lock-in amplifier has an error channel which provides the standard deviation of successive measurement performed at our set-point bandwidth. To do so, the lock-in amplifier acquisitions are 10 times longer than the bandwidth. We have seen that for times up to 10 seconds the stability of the system is good but stability at longer times is unknown. Fortunately the dispersion of successive measurements for different drive amplitudes is distributed linearly, as expected. This suggests

that it is still reasonable to perform successive measurement at the same drive amplitude, before determining the associated variance.

The standard deviation measured with this scheme is ca. 0.65 fN. An interesting observation is that the standard deviation measured at different small drive amplitudes gives a similar standard deviation. This provides an actual sub-fN resolution of the whole detection scheme. Experimentally, forces below the fN were not measured simply because it proved difficult to have a sufficiently wide modulation amplitude to successively visualize a strong force peak on the spectral density (to properly calibrate) and at the same time weak amplitude modulations for the lock-in detection scheme. The laser diode could not be modulated at lower or much higher amplitudes.

The experimental force resolution using a lock-in amplifier is one order of magnitude better than acquiring the whole PSD and handpicking the value on the spectrum.

5.3 SINGLE CHIRAL NANOPYRAMIDS: TRAPPING AND CHIRAL RECOGNITION

The capacity to trap small metallic nano-objects in our 3 lasers SWOT setup opens interesting perspectives in the context of optical chirality and polarization recognition of chiral nano-objects. We present here recent experiments that have been performed in close collaboration with the group of Prof. D.J. Norris, at ETH-Zurich. These experiments have consisted in setting up a polarization analysis strategy that allows recognizing the enantiomeric form of a single chiral Au nanopyramids (size ca. 150 nm) optically trapped in our SWOT.

5.3.1 *Trapping single chiral nanostructures*

A dispersion of chiral nano objects is prepared in water in presence of (trisodium citrate) (10% wt) to stabilize them (to avoid aggregation between them). The gold chiral nano objects, pictured by a SEM on Fig. 5.9 (image taken from [100]) are about 150 nm in size and have the shape of a thin walled open 4 sided pyramids. A clever fabrication strategy developed in the group of Prof. Norris has led to the fabrication of nanopyramids (NPys) with specific handedness that can be selected from the choice of high-index off-cut silicon wafers [100]. With all facet

edges of different sizes, the pyramids have no axis and no center of symmetry and are thus chiral.

An important circular dichroism (CD) signal around 630 nm as been reported on these objects, with a clear sign inversion of the CD spectra observed between two opposite enantiomeric forms of the NPys (see Fig. 3 in [100]). Important for the experiments, the CD response of the chiral NPys matches the second laser beam at 639 nm available in our experimental setup.

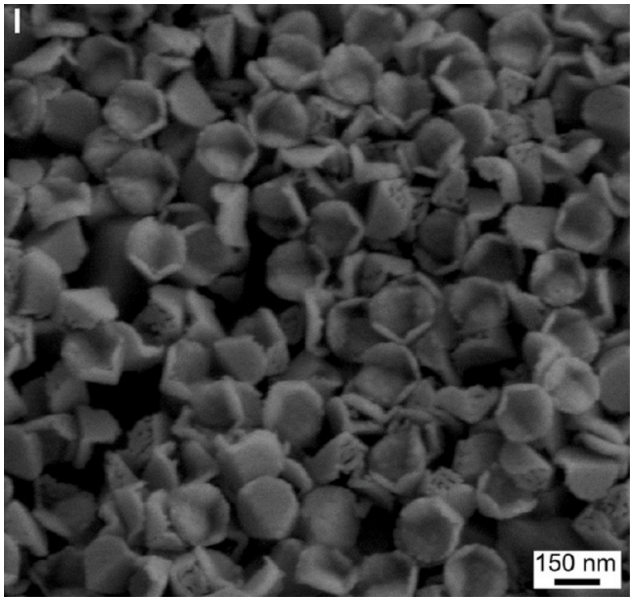

Figure 5.9: Scanning electron microscope (SEM) image of a dense film of left-handed Au nanopyramids similar to the one we use in our experiments. The image is taken from [100].

When immersed in fluids, metallic NPs are particularly keen to stick to the walls of the fluidic cell, rendering trapping difficult, if not simply impossible. The NPs become so much attracted by surface walls that the optical trap is simply not strong enough to hold them. As a consequence, the quality of the dispersion degrades rapidly in such a way that, after a few minutes, no more objects in the fluidic cell are available for trapping.

One way to reduce this effect is to charge negatively the metallic NPs. To do so, we use a citrate buffer solution at pH ca. 7.5. We also dip-coat the 0° dichroic mirror (end-wall of SWOT, that is also the fluidic cell) for 5 min in a 5% wt PSS solution (15 mL water and 5mL of PSS 30%). This allows charging negatively the surface of the dichroic mirror, so that

the electrostatic sticking mechanism is reduced by a charge repulsion component.

Under such conditions, the chiral NPys are trapped in our SWOT configuration about 3 µm away from the dichroic mirror surface. For these experiments, we use the same high 1.2 NA water immersion objective used for the force experiments. The iSCAT microscopy has been an important tool in order for characterizing the type of object trapped in the SWOT. The dispersion of chiral NPys, although mono disperse initially, displays indeed, when imaged under the iSCAT, a fairly broad population of objects of various sizes and diffusion velocities. But these NPys have a clear tendency to cluster and form pairs (more rarely trimers) in the buffer solution, aggregated forms that can not be separated with ultra-sound bathing. In our experiments, we took the highest precautions in order to be sure that the studied trapped objects are the ones corresponding to the smallest iSCAT scattering signature and with diffusive behaviors similar to those observed for single 150 nm gold nanospheres -implying that our trapped objects at least have a similar size and are not larger. Nevertheless, despite our precautions, we cannot totally warrant that the objects studied are composed of a genuine single chiral NPy. The concave shape of the chiral pyramids gives the possibility, not excluded, of a piling of 2 pyramids together.

With the mirror adjusted in a position such as to obtain the most stable trapping dynamics (that is a distribution of the fluctuations of the trap recollected intensity as Gaussian as possible when measured by the PIN photodiode -signal sent to an oscilloscope), the PSD associated with the 3 spatial directions, as well as the intensity histogram along the optical axis, are shown in Fig. 5.10.

Remarkably, we clearly observe a strong departure from the expected Lorentzian dynamics -such as the one measured for a trapped *conventional* nano object like a Au nanosphere- at low frequencies (below the trap roll-off frequency). This deviation is particularly well seen along the optical axis in panel 5.10a. The power dependence of the low frequency spectral response appears particularly clearly with $S_z[f] \propto f^{-1/2}$.

We are tempted to connect this low frequency signature, lying just between the low frequency plateau of the Lorentzian PSD and the 1/f shot noise spectral signature, to a signal stemming from the faceted-type geometry of the NPys. It is seen from panel 5.10b -displaying a Gaussian-like distribution

of positions- that the NPy is trapped and we know that in our SWOT, when considering metallic objects, the pyramid is trapped in a minimum of intensity. But every time, through Brownian diffusion, that one of the anti-node of the standing wave is hit by the NPy (the anti-node acting for the NPy as a light-wall), a sudden tumbling of the pyramid is induced. The NPy now exposes to the trapping beam a new facet with a different cross-section (we remind that each facet are different for the chiral NPy). This can lead to a modulation of the light scattered by the pyramid that could correspond to the low frequency noise signal observed.

While we still have to better understand this mechanism, it remains clear that we are able to trap a chiral NPy over sufficiently long time in order to perform real-time measurements on the trapped chiral object, in particular using the second laser beam at 639 nm.

5.3.2 *Chiral recognition by in-situ polarization experiment on trapped objects*

One such a measurement consists in performing a chiral-recognition experiment by analyzing the polarization of the 639 nm laser light scattered by the faceted NPys. To do this, we propose a very simple scheme based on monitoring the difference in left vs. right circularly polarized light on the scattered intensity signal recorded for two different enantiomers optically trapped (chiral NPy of left or right handedness). More precisely, we will probe the relation between the enantiomeric form and the third component of the Stokes vector $S_3 = \langle I_- - I_+ \rangle$ built on the difference between the averaged intensities measured on the scattered light field when analyzed in the left $-$ and in the $+$ circular polarization state.

In a sense, this strategy is to scattered light what Circularly Polarized Luminescence Spectroscopy (CPLS) is to emitted light. The technique of CPLS is widely exploited in the context of chiroptical spectroscopy in order to give information about the excited states of a chiral molecule [101]. A closely related approach has also recently been proposed by the group of Prof. D.J. Norris where the same Stokes parameter is involved at the level of the conservation law of optical chirality for lossy dispersive media and in relation with the measure of the optical chirality flux [102].

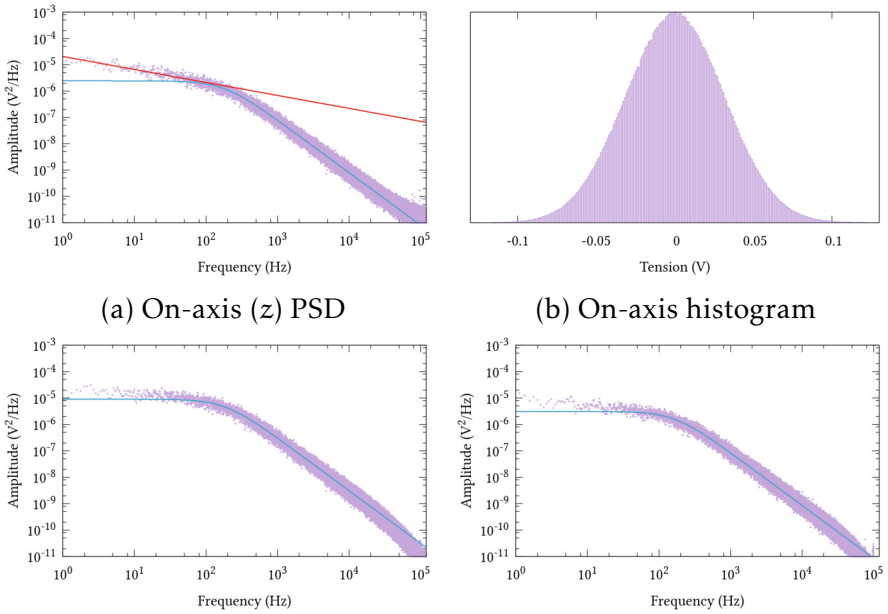

(a) On-axis (z) PSD (b) On-axis histogram

(c) Horizontal (x) PSD (d) Vertical (y) PSD

Figure 5.10: Power spectral densities along the 3 spatial axis for a trapped chiral NPy. Signals are taken from different detectors, the QPD for the transverse horizontal/vertical (x/y) components and the PIN photodiode for the axial z component. The pink curves represent the intensity PSDs averaged 8 time (for the sake of visibility). The blue curve gives the best Lorentzian fit of the data. The red line in panel (a) gives the best fit of the data on the low frequency part of the spectrum (from 1 to 200 Hz). The slope associated with the fit is -0.5. The intensity histogram along the optical axis shows a Gaussian like distribution of positions, meaning that the chiral NPy is well localized in space, and therefore well trapped.

5.3.3 *Experimental protocol*

Our experimental scheme can be described in a straightforward way. We start with a chiral NPy, optically trapped in the SWOT, which is illuminated by a second laser at 639 nm (wavelength tuned to the CD resonance of the chiral NP). This illumination laser is linearly polarized, a state of polarization that can be written in the basis of the circularly polarized states with $|\text{in}\rangle = \frac{1}{\sqrt{2}}(\sigma_+ + \sigma_-)$ where $\sigma_\pm$ correspond to the right/left

circularly polarized state. We will characterize the chiral NPy by its Jones matrix

$$J_+ = \begin{pmatrix} \alpha & 0 \\ 0 & \beta \end{pmatrix} \tag{5.8}$$

$$J_- = \begin{pmatrix} \beta & 0 \\ 0 & \alpha \end{pmatrix} \tag{5.9}$$

written for the two possible $\pm$ eniantomers in that same circular basis.

In this purely paraxial framework, the scattered polarization will simply write as $|\text{out}\rangle = \frac{1}{\sqrt{2}}(\alpha\sigma_+ + \beta\sigma_-)$ for the $+$ enantiomer and $|\text{out}\rangle = \frac{1}{\sqrt{2}}(\beta\sigma_+ + \alpha\sigma_-)$ for the $-$ enantiomer. This implies that the chiral object breaks the balance between right and left component of the input linear polarization. It is this balance that can be measured through the S_3 component of the Stokes vector of the scattered light, with $S_{3+} = |\beta|^2 - |\alpha|^2 = -S_{3-}$. The sign inversion emphasis how the recognition between the $\pm$ forms is eventually done.

A chiral NPy is trapped with our 785 nm laser beam in a quasi harmonic potential by carefully adjusting the SWOT. The second laser beam at 639 nm is turned on and linearly polarized. Its wavelength is resonant with the CD maximum of the trapped pyramid and the intensity is kept as low as the detection scheme permits. This beam is indeed simply used to probe the polarization property of the NPy. The forward scattered signal is then sent, as a direct transmission line, in the polarization analysis setup. Note that the direct transmission contains both the linearly polarized light field not intersected by the NPy, as well as the light scattered by the NPy in the forward direction. The probe 639 nm beam is focused on the trapped NPy in order to maximize the cross-section of the field with the NPy, the aim being to maximize the contribution of small polarization changes against the strong linearly polarized background.

A schematic representation of the experimental setup is given in Fig. 5.11. The incident probe is prepared linearly polarized (vertical) using a Glann-Taylor polarizer. The probe beam is inserted collinear to the trap beam with a 45° dichroic mirror. This beam, transmitted through the high NA trapping objective, is focused on the trapped NPy. The direct transmission is then collected using an imaging objective (NA 0.6, 40×). The transmitted light is sent to the analysis setup which

is composed of a quarter-wave plate (QWP) at 45°, followed by a half-wave plate (HWP) and a Wollaston prism.

The Wollaston prism is the key element of our setup. It separates the incident beam in two linear (vertical and horizontal) polarized beams by an angle of 20°. Both output channels of the Wollaston prism are then sent to a balanced photodetector which will enable substracting the two signals. This scheme is used to (i) subtract the high intensity (and irrelevant) contribution coming from the directly transmitted porbe beam, and (ii) to measure directly the S_3 component of the Stokes vector without any rotation of the different wave plates, as described in [103, 104].

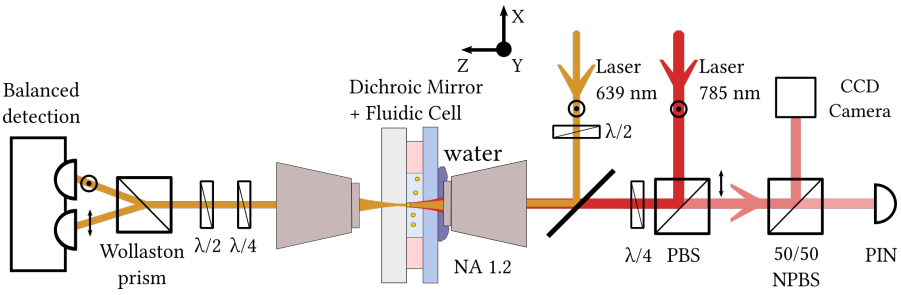

Figure 5.11: Scheme representing the experimental setup used for the chiral recognition experiment. This scheme is similar to the one presented for the trapping of chiral nano-objects but a polarization analysis part is developed behind the second (collection) objective. The iSCAT beam is still available but injected with a flipping mirror so that it can be removed once the chiral nanopyramid is trapped. The S_3 component of the Stokes vector is measured by injecting a linearly polarized beam on a trapped object. This probe beam is then decomposed on the circular polarization basis and both left and right circular polarization contributions are subtracted by the balanced photodiode detector (Newfocus 2307).

The main difficulty of the experiment stems from a measure given as a difference between two signals. This implies that any slight change in the alignment or in a polarization element can yield a signal that will give, on the balanced photodetector, a different sign despite the fact that the the sample under study has not been changed. It is therefore very important that we can provide an alignment scheme easily reproducible throughout the different experiments, providing therefore reliable results.

The alignment and preparation procedures of the polarization-optics elements go as follow:

- An object is first trapped for the sole purpose of adjusting the perfect overlap between both the trap beam and the probe beam. The trap turned off, the object is then released. Starting from now, the sample holder is fixed immobile. The trap is reopened and the iSCAT microscope is used in order to track the arrival of the trapped object and its quality (monomer, dimer, etc.) of it.

- While the trap is still empty, the incident linearly polarized beam is adjusted such that the reflection on the dichroic mirror is minimized by measuring the maximal transmitted intensity after reflection.

- The probe beam is then transmitted through the objectives. The Wollaston prism is rotated (in the absence of the HWP and the QWP) such that both the output beams are at the same altitude with respect to the horizontal plane set by the optical table. They hit thereby the two photodiodes of the balanced detection in their center.

- The HWP analyzer is inserted on the optical axis and rotated to have the input linear polarization maximized in the vertical output channel of the Wollaston. The measured (negative) intensity on the balanced detection is maximized on the oscilloscope.

- The gain of the balanced photodetector is set to its maximum and the probe beam is periodically modulated around its mean intensity at 10 kHz using a function generator. The oscilloscope trigger is synchronized with the function generator. We do this in order to have an external and robust procedure to determine the QWP angle. To do so, we rotate the QWP until the difference in amplitude between the two channels is minimized in the absence of any trapped object. The signal measured on an oscilloscope becomes completely flat. The rotation angle of the QWP is close to 45°.

- With this approach, and despite our best efforts, the amplitude at the output of the balanced detection is not exactly zero. Adjusting the output of the balanced detection to remove this offset proved difficult. For practical reasons, this offset is subtracted using a tension generator,

centering the signal on the oscilloscope to properly fill the dynamical range of the oscilloscope.

Under this scheme, two configurations of interest are taken care properly:

- A incident linear polarization becomes circular after passing through the QWP. The circularly polarized beam is then decomposed in its two orthogonal linear components by the Wollaston prism, with equal intensity that are subtracted by the balanced detection scheme.

- A circular polarized beam incident on the QWP is changed into a linearly polarized beam. The Wollaston prism will output all the intensity in one of its channel. In our experiment, the vertical polarization that goes to the left at the output of the prism is measured as negative by the balanced detection.

In this detection scheme, most of the light intensity contribution collected on the balanced detection comes from the non-scattered (linearly polarized) direct transmission of the probe beam and is directly subtracted by the balanced detection. This ensures that the signal is essentially proportional to the difference in circular polarizations.

Furthermore and importantly, this polarization analysis procedure yields, with respect to the reference intensity on the balanced detection, a lower mean value when the light beam is elliptically polarized with right handedness (a dominant right helicity) while left circularly polarized contribution will increase the mean value.

In order to perform this polarization analysis, two identical samples are prepared, at the same time, using similar dichroic mirrors, the same type of fluidic cell and cover glasses. One cell is filled with a dispersion of right-handed NPy, while the other with the opposite enantiomeric dispersion (all dispersions, again, prepared in the laboratory of Prof. Norris). This pair of sample is then probed in a sequenced way. First, a right chiral NPy is trapped and the analysis procedure is performed. Then, the sample is changed for the cell containing the left chiral NPy. The trap is opened and a NPy is trapped. Nothing is moved on the optical part, and the alignment is perfectly preserved. Combining the interference imaging with the recollected intensity from the trap beam, it was also ensured that the trapped NPys in both cases had the same scattering

intensities and imaging signature (thus same size). In addition and again, only the data corresponding to the smallest trapped object in our dispersions have been considered.

The trigger synchronization fixes the phase of the signal between the the modulated probe beam and the balance photodetector signal. This phase-locks the recorded intensities for both chiral enantiomeres. Two five-periods intensity time-traces are presented for both right and left trapped NPys in Fig. 5.12.

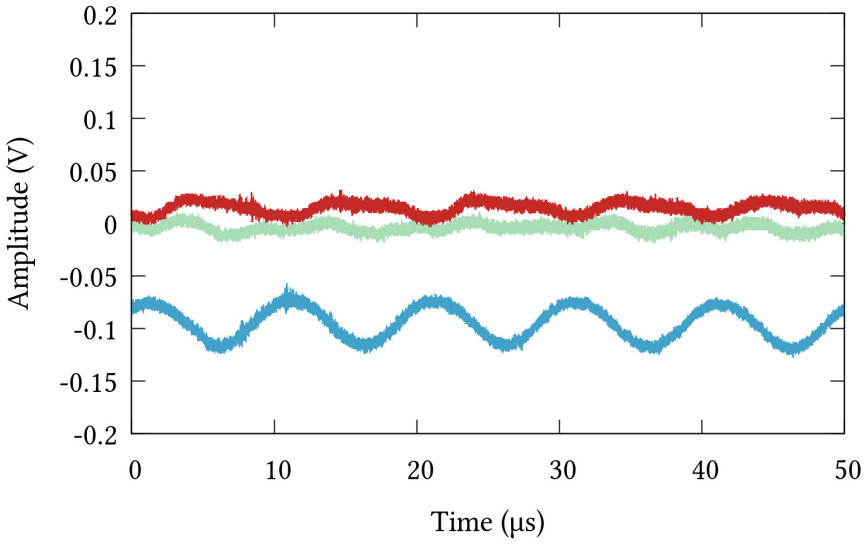

Figure 5.12: Time-traces recorded over five intensity modulation periods for two chiral NPys of opposite handedness. The signals are synchronized using the modulation trigger. The blue curve corresponds to a chiral right NPy while the red curve is the left enantiomer. The signal exhibits non overlapping intensity differences as well as phase opposition.

As observed in Fig. 5.12, the mean intensity measured for a right-handed chiral NPy is much below the one associated with a left-handed NPy. This implies that the former signal is essentially right-handed elliptically polarized, while the latter left-handed elliptically polarized. In addition, a slight inversion in the phase of the signal is observed. In theory, without our experimental limitations (intensity offset on the balanced detection), both signal should have a entirely symmetrical signature with respect to 0. The signal is indeed expected to have a negative or positive mean intensity value for respectively right- or left-handed NPys. Moreover, because the intensity is modulated, a stronger probe field induces a stronger

response on the balanced detection, leading to measure the two sinusoidal response in phase opposition.

These limitations being well-understood, it is perfectly clear that our scheme enables performing the recognition of chiral enantiomers. Central to this capacity is the fact that we have been able to immobilize in the SWOT a single chiral nano-object which handedness can therefore be determined by measuring the degree of circular polarization of the field scattered by this trapped chiral object.

5.4 CONCLUSION

The versatility of the SWOT is exploited in this Chapter in 3 directions:

- optical trapping of metallic NPs of small (but still, moderate) sizes
- high-resolution force spectroscopy
- polarization-based recognition of nano-enantiomers

Because small metallic objects (smaller than visible light wavelength) are difficult to observe, we expand our setup with an interferometric imaging microscope in the iSCAT framework. This method allows us imaging and characterizing easily our Au NPs ($R = 75$ nm) diffusing in the fluid.

We show how to measure weak optical forces in a fluid, by implementing in our SWOT a dynamic mode approach, analogous to what is routinely done in atomic force microscopy [105]:

- we measure optical forces directly from a power spectral density analysis,
- we measure optical forces involving a lock-in amplifier, improving the force resolution level. With this approach, we measure forces down to 2 fN, with a sub-fN error.

We stress that these measurements have not involved any PSD averaging throughout long acquisition times. Such long acquisition times are hardly available in our fluidic system, where low frequency drifts limit the available measurement bandwidth. Our measurements are acquired on the optimal acquisition time that is derived from the calculated Allan variance for our system.

Finally, we also trap in our setup more exotic nano-objects such as chiral metallic nanopyramids. We perform chiral recognition measurements at a single nano-enantiomer level, developing at the level of optically trapped chiral nanopyramids, a specific polarization analysis scheme adapted to our optical piston setup.

6

GENERAL CONCLUSION

In this thesis, we have developed an original optical trap, the optical piston, which versatility has been explored through different experiments.

By carefully positioning the end-mirror, we are able to tune the interfering phase between the incident and reflected beams inside the piston in order to study one-dimensional bistability. We showed how the monitoring of the metastable trajectory of an optically trapped Brownian bead leads to solve entirely the interaction potential. We emphasized in particular that such bistable optical potentials cannot be described with simple Duffing-type potentials but demonstrated how the Kramers rate equations become an appropriate tool for the determination of the potential.

We have then looked into the thermodynamics associated with a step-wise reversible compression of the piston. This has led us to study the cross-over between a region of dynamical stability (i.e. harmonic optical trapping) and a region of dynamical bistability (i.e. optical trapping in the presence of two metastable states). This analysis concluded that while the piston injects work on the bead when compressed, most of that work is consumed as potential energy, the remaining few percent being given to the bath as heat. Remarkably, the heat produced is directly determined from the optical deformation induced though the compression.

The stochastic nature of the motion of the optically trapped bead is also keen to different types of statistical approaches and analysis. In the context of stochastic resonance, where the end-mirror of the piston is modulated periodically for instance, a Mandel factor approach and a time-delay analysis on the hopping events between metastable states have proven efficient in interpreting the different results acquired in different regimes of drive. This has led us to observe and analysis regimes as

different as rectified motion, synchronization and non-adiabatic coupling.

In the last part of the thesis, we have also emphasized some of the many possibilities that an optical piston offers as far as trapping is concerned. We have shown how metallic nanoparticles can be trapped fairly easily, up to size of the order of 150 nm. On such metallic nanoparticle, we have also demonstrated the capacity of our configuration to act as a weak force measurement system.

This brought us to trap more exotic metallic objects. In a collaboration with the group of Prof. D.J. Norris, at ETH-Zurich, we have optically trapped chiral nanopyramids at the single enantiomer level. With such chiral objects, we developed a specific setup that can perform a circular polarization analysis of light signal scattered off the optically trapped nanopyramid in order to do polarization-based chiral recognition of single enantiomers.

These experiments draw a clear perspective for the near future, illustratating the potential of our setup in the growing field of chiral nano-optics [106]. In particular, one pressing objective is to combine our two approaches on high-resolution force spectroscopy and chiral optical trapping in order to study these so-called chiral optical forces, recently predicted theoretically [107–109], observed at the micron-scale [110], but still elusive at the nano-scale.

APPENDIX

A

THE DISCRETE LANGEVIN EQUATION

This appendix describes how the usual inertial Langevin equation

$$m_B \ddot{z}(t) + \gamma \dot{z}(t) = -\partial_z U(z(t)) + F_{Th}(t) \tag{A.1}$$

is numerical solved, following the scheme presented in the next section.

Technically the modern computers processors ability to run a work on multiple cores is exploited. For given simulation parameters the numerical "experiment" is run multiple times and the results form each run are averaged to give an error estimate on the measured parameters, similarly to the experimental error obtained from an experiment repeated multiple times. In fact for such experiments ergodicity is valid and one would obtain the same result from a long time trace than N different runs N times shorter then concatenated in one single long time trace.

Simulations are performed using parameters similar to experimental ones, a potential that has similar residency times and spatial separation, and the same time step as for experimental acquisitions. The interaction potential derived in the previous chapters is not used here but a simple Duffing potential is used, the only reason for this is that performing such simulations is computationally intensive and performing polynomial computations is orders of magnitude faster than complex expression with exponential, division and trigonometric terms. The precision used throughout the simulations is floating point numbers of 32 bits which is largely sufficient for the operations performed in the code.

An important aspect of such simulations is the bath simulation, in other word we require the bath to be entirely uncorrelated in time yet, because we perform a computer simulation, two runs at different times with the same parameters

must yield the exact same result. To meet this criteria a pseudo random number generator[1] is used to simulate the bath Gaussian white noise source. A seed is determined to characterize the bath initial point. This seed also uniquely characterizes the number sequence. The same seed is kept for each of the many runs performed with a given system set of parameters. It allows comparing potential or dynamical parameters on single realizations of the bead trajectory across amplitude or frequency changes of the external drive.

In our usual case 64 numerical "experiments" are realized simultaneously. Each of these realization has a distinct bath but nevertheless the general properties of the bath must be preserved, mainly that the temporal trace is Gaussianly distributed and secondly this signal is temporally uncorrelated, in other word its frequency spectrum is flat, all frequencies are equally present. All these requisites are met by the used random number generator. These properties are illustrated on Fig. A.1 which presents the power spectral density for one minute long random sequence. The number sequence has a PSD that is flat at an amplitude of 2, signature of a Gaussian white noise. (todo compute it).

Simulations study rare events with respect to the sampling time step, namely the instant the bead switches states. Therefore the simulation run time is long (we have here no issue of fluidic or thermal drift !). Modern computer can simulate hours of bistable experiment in a few minutes. Recording time traces would produce terabytes of data every minute with little value to them but a few points (less than 1 point every 100000). Moreover these time traces later need to be treated, usually by correlation techniques. For such simulations time correlation is prohibited because of its slowness, power spectral density would be suited to provide the mean residency time of the bead in a perfectly symmetrical configuration but otherwise the PSD averages two characteristic times does not offer information on the directivity of the transitions.

We want to perform the statistical analysis at the same time as the simulation is run. Another characterization of the dynamics is therefore needed, one that only depend on the knowledge of the previous positions. To characterize the bistable dynamics one first needs to determine the instant the

1 The random number generator function used is **gsl_ran_gaussian ()** from the GNU Scientific Library. [111]

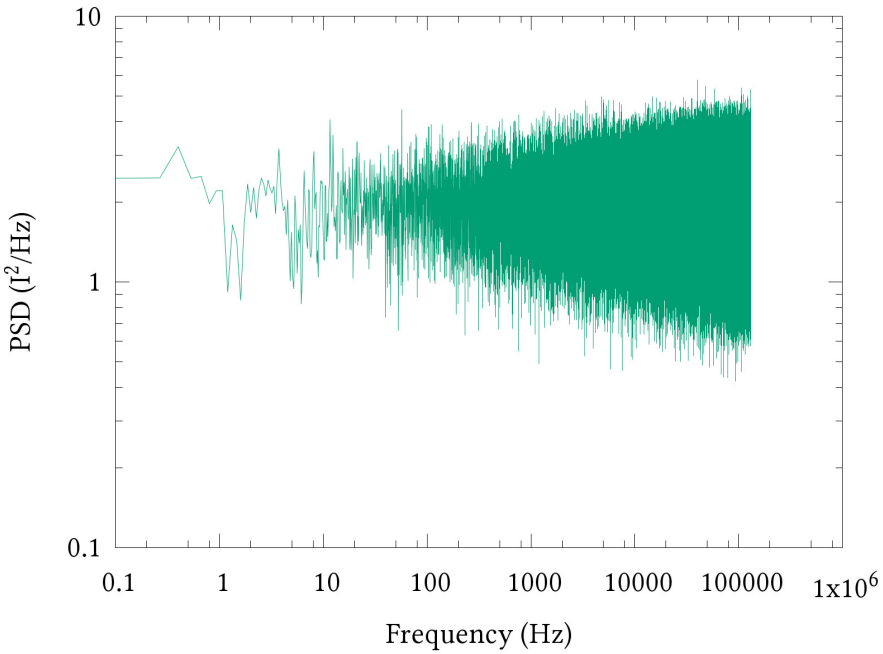

Figure A.1: Power spectral density of the generated (fixed) random sequence for a minute long signal @ 262kHz. A Gaussian white noise has a PSD amplitude of 2. The generated sequence presents a good white spectral signature.

bead changes state during its time evolution in the potential which as is discussed later is not inconsequential.

To "simulate" the metastable dynamics of a trapped bead by a numerical resolution of the Langevin equation of the bead motion. The general expression of a Langevin equation for the bead center of mass $z(t)$ is rewritten using differential operators as:

$$m_B D_{tt}(z(t)) + \gamma D_t z(t) - \nabla U(z(t)) = F_{Th}(T, z(t), t) \qquad (A.2)$$

with D_t the linear differential operator, $D_{tt} = D_t D_t$, m_B the mass of the bead, γ the viscosity of the fluid, $U(z(t))$ the potential energy exerted on the bead and $F_{Th}(T, z(t), t) = \sqrt{2 k_b T \gamma}\eta(z(t), t)$ the Gaussian white noise with $\eta(z(t), t)$ a Wiener process. Even though the inertial term has a completely negligible contribution to the bead dynamics there is no reason to remove it from the numerical simulation, making it less general.

The Wiener Process involves "stochasticity" thus "random numbers", there is no easy way to solve the equation analytically

as each bead position will (partially) change independently of the previous positions. For this reason we "solve" this equation step by step , by small time increments. We should also not be too concerned about the initial conditions of the bead, position and velocity when starting a simulation for long time series. In this case, a stationary dynamics emerges and the same mean dynamics are obtained for simulations (of identical parameters) regardless of the initial conditions, they become negligible.

Our discretization approach follows the one described in [112]. Time and space are discretized using the simplest finite difference scheme. The simulation evolves by iterations with a fixed time step. For a given time dependent variable $z(t)$ we associate a discrete counterpart z_i with i being the discrete time coordinate of the signal z such that $i \times \Delta t \simeq t$. Expressed differently, the discrete variable is the nearest sampled value of position $z(t)$ and its index is $i \simeq \frac{t}{\Delta t}$.

Using the usual differentiation definition, application of the differential operator D_t transforms a signal $z(t)$ as

$$D_t(z(t)) = \lim_{\Delta t \to 0} \left(\frac{z(t) - z(t - \Delta t)}{\Delta t} \right). \tag{A.3}$$

Note that it is the "lagged" expression of the differentiation but the "forward" expression

$$D_t(z(t)) = \lim_{\Delta t \to 0} \left(\frac{z(t + \Delta t) - z(t)}{\Delta t} \right), \tag{A.4}$$

is exactly equivalent for $z(t)$.

Following this scheme we also compute the second time derivative D_{tt} by mixing the "forward" and "lagged" expressions to obtain a symmetric relation:

$$\begin{aligned}
D_{tt}(z(t)) &= D_t(D_t(z(t))) && \text{(A.5)}\\
&= D_t \lim_{\Delta t \to 0} \left(\frac{z(t) - z(t - \Delta t)}{\Delta t} \right) && \text{(A.6)}\\
&= \lim_{\Delta t \to 0} \left(\frac{1}{\Delta t} \left(D_t(z(t)) - D_t(z(t - \Delta t)) \right) \right) && \text{(A.7)}\\
&= \lim_{\Delta t \to 0} \left(\frac{1}{\Delta t} \left(\frac{z(t + \Delta t) - z(t)}{\Delta t} - \frac{z(t) - z(t - \Delta t)}{\Delta t} \right) \right) && \text{(A.8)}\\
&= \lim_{\Delta t \to 0} \left(\frac{1}{\Delta t^2} \left(z(t + \Delta t) - 2z(t) + z(t - \Delta t) \right) \right) && \text{(A.9)}
\end{aligned}$$

These expressions, dependent on continuous variableare the transposed to their discrete counterparts considering an infinitesimal time Δt. The discrete coordinates at step i for both differential operators are,

$$D_t^i(x) = \frac{1}{\Delta t}(z_{i+1} - z_i) \tag{A.10}$$

$$D_{tt}^i(x) = \frac{1}{\Delta t^2}(z_{i+1} - 2z_i + z_{i-1}). \tag{A.11}$$

The noise function $\eta(z(t), t)$ is assumed to be independent to the position $z(t)$ and thus $\eta(z(t), t) = \eta(t)$. This noise function is written W_i in the discrete case and has a normal distribution ($N(0, 1)$) with zero as mean value and a variance of one. The list of the W_i values is uncorrelated so there is little concern to have about the initial value of the index denoting this function. Subsiding the previous derivative operators expressions in their discrete form as well as discretized time and bead positions in the Langevin equation (A.2) yields,

$$m_B\left(\frac{z_i - 2z_{i-1} + z_{i-2}}{\Delta t^2}\right) + \gamma\left(\frac{z_i - z_{i-1}}{\Delta t}\right) - \nabla U(z_{i-1}) = \sqrt{2k_b T\gamma}\, W_{i-1}. \tag{A.12}$$

We should take a bit of time to discuss in the previous relationship the index dependency. An index shift $i \to (i-1)$ is performed or in other words all relations are "lagged". It is because we wanted to derive an expression for the center of mass position at "time" i and for this only information coming from previous steps $k < i$ can be used but nothing after, it would render the scheme non-causal. This is the reason why it is critical to express the current position as a function of the potential at the previous position which indeed is equivalent and induces no changes in the continuous case when the limit is taken but is of great implication in the discrete case. The dependency of the potential on previously computed position allows us to use any form of potentials, even non continuous potentials transparently in our code. The noise function is indexed with $i - 1$ just for consistency with other variables. Reoganization of the discrete Langevin equation (A.12) and factorizing z_i the next position gives:

$$z_i = C_0\left(C_{-1} z_{i-1} - z_{i-2} + C_{pot}\nabla U(z_{i-1}) + C_{stoch} W_{i-1}\right) \tag{A.13}$$

with $C_0 = \frac{1}{1+\frac{\Delta t\gamma}{m_B}}$, $C_{-1} = 2 + \frac{\Delta t\gamma}{m_B}$, $C_{pot} = \frac{\Delta t^2}{m_B}$ and $C_{stoch} = \frac{\Delta t^2}{m_B}\sqrt{2k_bT\gamma}$. The coefficient in front of z_{i-2} being just -1 it was not worth to introduce one more coefficient.

Now that we have derived a discrete expression for the Langevin equation that is solvable by iteration it is critical to look at the quantities manipulated, at their value. We study small systems of micrometric size and the typical displacements of these objects is around the tens of nanometers. Some of variables have very small values, this is without talking about k_BT which is around 10^{-20} J/K or the mass of the bead of 10^{-16} kg.

For all these reasons and to avoid possible numerical hindrances occurring when operating with very big or small values we propose to change the unit system and use micrometers, micrograms, seconds and absolute temperature in Kelvins. This way k_B has a value of $1.3806503\,10^{-2}\,\frac{\mu g\,\mu m^2}{s^2}$ and the mass, the smallest value is around $10^{-7}\,\mu g$ such that the factor $\frac{\Delta t}{m_B}$ is not too small nor too big when Δt around the microsecond as is used here. The unit of the force associated to this system of unit is the femtoNewton which is exactly the order of magnitude of the forces studied experimentally. Similarly the energy range is at the zepto Joules, the unit of thermal fluctuation energy k_BT.

B

FORCE CALIBRATION

This appendix present the data used in Chapter 4 toimplement the force measurement method of Ch. 5 in order to determine experimentally the amplitude of the external driving force exerted on the bistable bead.

The main requisite to properly apply our force measurement scheme is that the bead is trapped in a quasi-harmonic potential. To achieve this conditions when performing the bistable measurements, before or after the experiment, the mirror is displaced such that the nearest single welled potential is reached. Once the bead is confined in this quasi-harmonic potential, acquisitions are performed and the sinusoidal force applied on the bead in the bistable configuration applied on the bead in the stable trap.The spectral density is then taken from the intensity time trace, calibrated and the value of the peak appearing at the drive frequency measured, giving the associated drive force. This drive force being a fraction of the laser diode intensity the constant pushing force contribution is also obtained by linearity of the force with the field intensity.

Figures B.1a and B.1b present the measured intensity time trace and its associated histogram for the bead trapped in a quasi-harmonic potential under an external drive of 10 kHz. The power spectral density of the intensity time trace (Fig. B.1c) follows a Lorentzian shape, the influence of the potential is considered as harmonic and the external drive is strong enough to leave a sharp contribution at the drive frequency. The choice of a higher frequency to measure the force is discussed in details in the next chapter in particular it helps that the bead is in its free brownian diffusion regime.

The measured force applied on the bead by the external is determined to be of about 700 fN while the constant contribution from the pushing beam is of 2 piconewtons. The drive amplitude justifies that the applied external force is strong.

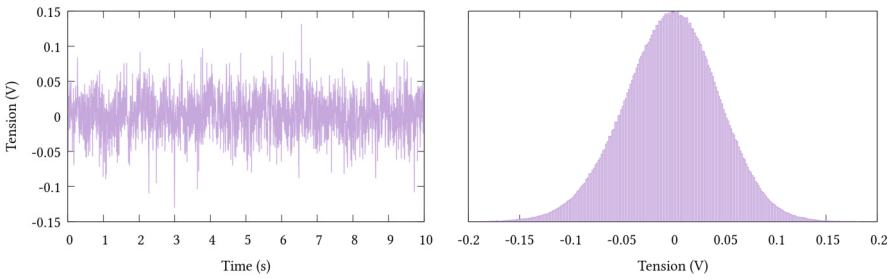

(a) Intensity time trace (b) Intensity distribution

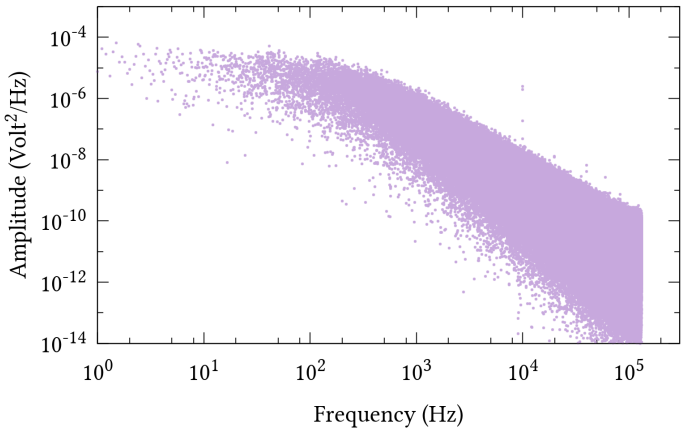

(c) PSD of the recorded intensity, a Lorentzian shape for the trapped bead followed and the external drive source visible at 10 kHz.

Figure B.1: Experiment time trace, intensity distribution histogram and PSD for a 1 µm melamine bead trapped in a quasi-harmonic potential in the presence of an external drive at 10 kHz. The time trace presents data clustered by packs of 1024 points while the PSD is not averaged.

BIBLIOGRAPHY

[1] A. Ashkin, "Acceleration and trapping of particles by radiation pressure", Phys. Rev. Lett. **24**, 156–159 (1970) (cit. on p. 2).

[2] A. Ashkin, J. M. Dziedzic, J. E. Bjorkholm, and S. Chu, "Observation of a single-beam gradient force optical trap for dielectric particles", Opt. Lett. **11**, 288–290 (1986) (cit. on pp. 2, 7).

[3] M. S. Z. Kellermayer, S. B. Smith, H. L. Granzier, and C. Bustamante, "Folding-unfolding transitions in single titin molecules characterized with laser tweezers", Science **276**, 1112–1116 (1997) (cit. on p. 2).

[4] M. D. Wang, H. Yin, R. Landick, J. Gelles, and S. M. Block, "Stretching DNA with optical tweezers.", Biophysical Journal **72**, 1335–1346 (1997) (cit. on p. 2).

[5] D. E. Smith, S. J. Tans, S. B. Smith, S. Grimes, D. L. Anderson, and C. Bustamante, "The bacteriophage [phis]29 portal motor can package DNA against a large internal force", Nature **413**, 748–752 (2001) (cit. on p. 2).

[6] U. Seifert, Rep. Prog. Phys. **75** (2012) (cit. on p. 2).

[7] A. Simon and A. Libchaber, Phys. Rev. Lett. **68** (1992) (cit. on pp. 2, 5, 19, 82, 83, 120).

[8] L. McCann, M. Dykman, and B. Golding, Nature **402** (1999) (cit. on pp. 2, 5, 18, 19, 68).

[9] Y. Hayashi, S. Ashihara, T. Shimura, and K. Kuroda, Opt. Commun. **281** (2008) (cit. on p. 2).

[10] M. Siler and P. Zemánek, New J. Phys. **12** (2010) (cit. on p. 2).

[11] G. Wang, E. Sevick, E. Mittag, D. Searles, and D. Evans, Phys. Rev. Lett. **89** (2002) (cit. on p. 2).

[12] C. Bustamante, J. Liphardt, and F. Ritort, Phys. Today **58** (2005) (cit. on pp. 2, 14).

[13] V. Blickle, T. Speck, L. Helden, U. Seifert, and C. Bechinger, Phys. Rev. Lett. **96** (2006) (cit. on p. 2).

[14] J. Gieseler, R. Quidant, C. Dellago, and L. Novotny, Nat. Nano. **9** (2014) (cit. on pp. 2, 13, 14).

[15] A. Bérut, A. Arakelyan, A. Petrosyan, S. Ciliberto, R. Dillenschneider, and E. Lutz, Nature **483** (2012) (cit. on pp. 2, 16, 17, 82).

[16] E. Roldan, I. A. Martinez, J. M. R. Parrondo, and D. Petrov, "Universal features in the energetics of symmetry breaking", Nat Phys **10**, 457–461 (2014) (cit. on pp. 2, 5, 18).

[17] Y. Jun, M. Gavrilov, and J. Bechhoefer, Phys. Rev. Lett. **113** (2014) (cit. on p. 2).

[18] M. A. Bevan and D. C. Prieve, "Direct measurement of retarded van der waals attraction", Langmuir **15**, 7925–7936 (1999) (cit. on p. 2).

[19] L. Helden, R. Eichhorn, and C. Bechinger, "Direct measurement of thermophoretic forces", Soft Matter **11**, 2379–2386 (2015) (cit. on pp. 2, 123).

[20] L. Liu, S. Kheifets, V. Ginis, and F. Capasso, "Subfemtonewton force spectroscopy at the thermal limit in liquids", Phys. Rev. Lett. **116**, 228001 (2016) (cit. on pp. 2, 123, 127).

[21] D. S. E. jr., L. B. Pires, S. Umrath, D. Martinez, Y. Ayala, B. Pontes, G. R. de S. Araújo, S. Frases, G.-L. Ingold, F. S. S. Rosa, N. B. Viana, H. M. Nussenzveig, and P. A. M. Neto, "Probing the casimir force with optical tweezers", EPL (Europhysics Letters) **112**, 44001 (2015) (cit. on pp. 2, 123).

[22] P. Jop, A. Petrosyan, and S. Ciliberto, "Work and dissipation fluctuations near the stochastic resonance of a colloidal particle", EPL (Europhysics Letters) **81**, 50005 (2008) (cit. on pp. 5, 18, 19, 21).

[23] H. Kramers, Physica A **7** (1940) (cit. on pp. 5, 41).

[24] L. Gammaitoni, P. Hänggi, P. Jung, and F. Marchesoni, "Stochastic resonance", Rev. Mod. Phys. **70**, 223–287 (1998) (cit. on pp. 5, 79–83).

[25] A. Canaguier-Durand, A. Cuche, C. Genet, and T. W. Ebbesen, "Force and torque on an electric dipole by spinning light fields", Phys. Rev. A **88**, 033831 (2013) (cit. on p. 6).

[26] A. Ashkin, "Optical trapping and manipulation of neutral particles usinglasers", Proceedings of the National Academy of Sciences **94**, 4853–4860 (1997) (cit. on pp. 7, 8).

[27] S. B. Smith, Y. Cui, and C. Bustamente, "Overstretching b-dna: the elastic response of individual double-stranded and single-stranded dna molecules", Science **271**, 795 (1996) (cit. on p. 7).

[28] A. van der Horst, A. I. Campbell, L. K. van Vugt, D. A. M. Vanmaekelbergh, M. Dogterom, and A. van Blaaderen, "Manipulating metal-oxide nanowires using counter-propagating optical line tweezers", Opt. Express **15**, 11629–11639 (2007) (cit. on p. 7).

[29] T. Li, S. Kheifets, D. Medellin, and M. G. Raizen, "Measurement of the instantaneous velocity of a brownian particle", Science **328**, 1673–1675 (2010) (cit. on p. 7).

[30] P. Zemánek, A. Jonás, L. Srámek, and M. Liska, "Optical trapping of rayleigh particles using a gaussian standing wave", Optics Communications **151**, 273–285 (1998) (cit. on p. 8).

[31] P. Zemánek, A. Jonás, L. Srámek, and M. Liska, "Optical trapping of nanoparticles and microparticles by a gaussian standing wave", Opt. Lett. **24**, 1448–1450 (1999) (cit. on p. 8).

[32] E. Schäffer, S. F. Nørrelykke, and J. Howard, "Surface forces and drag coefficients of microspheres near a plane surface measured with optical tweezers", Langmuir **23**, PMID: 17326669, 3654–3665 (2007) (cit. on p. 8).

[33] J. Leach, H. Mushfique, S. Keen, R. D. Leonardo, G. Ruocco, J. Cooper, and M. Padgett, Phys. Rev. E **79** (2009) (cit. on pp. 8, 41, 75, 131).

[34] A. Cuche, O. Mahboub, E. Devaux, C. Genet, and T. W. Ebbesen, "Plasmonic coherent drive of an optical trap", Phys. Rev. Lett. **108**, 026801 (2012) (cit. on p. 8).

[35] P. Zemánek, A. Jonás, P. Jákl, J. Jezek, M. Serý, and M. Liska, "Theoretical comparison of optical traps created by standing wave and single beam", Optics Communications **220**, 401–412 (2003) (cit. on p. 9).

[36] A. Lehmuskero, P. Johansson, H. Rubinsztein-Dunlop, L. Tong, and M. Käll, "Laser trapping of colloidal metal nanoparticles", ACS Nano **9**, 3453–3469 (2015) (cit. on p. 9).

[37] K. Svoboda and S. M. Block, "Optical trapping of metallic rayleigh particles", Opt. Lett. **19**, 930–932 (1994) (cit. on p. 9).

[38] A. Ohlinger, A. Deak, A. A. Lutich, and J. Feldmann, "Optically trapped gold nanoparticle enables listening at the microscale", Phys. Rev. Lett. **108**, 018101 (2012) (cit. on p. 9).

[39]P. M. Hansen, V. K. Bhatia, N. Harrit, and L. Oddershede, "Expanding the optical trapping range of gold nanoparticles", Nano Letters **5**, 1937–1942 (2005) (cit. on p. 9).

[40]L. Bosanac, T. Aabo, P. M. Bendix, and L. B. Oddershede, "Efficient optical trapping and visualization of silver nanoparticles", Nano Letters **8**, 1486–1491 (2008) (cit. on p. 9).

[41]F. Hajizadeh and S. S.Reihani, "Optimized optical trapping of gold nanoparticles", Opt. Express **18**, 551–559 (2010) (cit. on p. 9).

[42]O. Brzobohatý, M. iler, J. Trojek, L. Chvátal, V. Karásek, A. Paták, Z. Pokorná, F. Mika, and P. Zemánek, "Three-dimensional optical trapping of a plasmonic nanoparticle using low numerical aperture optical tweezers", Scientific Reports **5**, 8106 (2015) (cit. on pp. 9, 123).

[43]O. Brzobohatý, M. iler, J. Trojek, L. Chvátal, V. Karásek, and P. Zemánek, "Non-spherical gold nanoparticles trapped in optical tweezers: shape matters", Opt. Express **23**, 8179–8189 (2015) (cit. on p. 9).

[44]P. V. Ruijgrok, N. R. Verhart, P. Zijlstra, A. L. Tchebotareva, and M. Orrit, "Brownian fluctuations and heating of an optically aligned gold nanorod", Phys. Rev. Lett. **107**, 037401 (2011) (cit. on p. 9).

[45]A. Lehmuskero, R. Ogier, T. Gschneidtner, P. Johansson, and M. Käll, "Ultrafast spinning of gold nanoparticles in water using circularly polarized light", Nano Letters **13**, 3129–3134 (2013) (cit. on p. 10).

[46]A. Lehmuskero, Y. Li, P. Johansson, and M. Käll, "Plasmonic particles set into fast orbital motion by an optical vortex beam", Opt. Express **22**, 4349–4356 (2014) (cit. on p. 10).

[47]L. Shao, Z.-J. Yang, D. Andrén, P. Johansson, and M. Käll, "Gold nanorod rotary motors driven by resonant light scattering", ACS Nano **9**, 12542–12551 (2015) (cit. on p. 10).

[48]P. Langevin, "Sur la théorie du mouvement brownien", CR Acad. Sci. Paris **146**, 530 (1908) (cit. on p. 10).

[49]F. Reif, *Fundamentals of statistical and thermal physics* (Waveland Press, 2009) (cit. on p. 11).

[50]K. Sekimoto, *Stochastic energetics* (Springer, Heidelberg, 2010) (cit. on pp. 12, 59, 62, 69, 72).

[51]G. M. Wang, E. M. Sevick, E. Mittag, D. J. Searles, and D. J. Evans, "Experimental demonstration of violations of the second law of thermodynamics for small systems and short time scales", Phys. Rev. Lett. **89**, 050601 (2002) (cit. on p. 13).

[52]C. Jarzynski, "Nonequilibrium equality for free energy differences", Phys. Rev. Lett. **78**, 2690–2693 (1997) (cit. on pp. 13, 14, 16).

[53]D. Y. Lee, C. Kwon, and H. K. Pak, "Nonequilibrium fluctuations for a single-particle analog of gas in a soft wall", Phys. Rev. Lett. **114**, 060603 (2015) (cit. on p. 13).

[54]I. A. Martnez, É. Roldán, L. Dinis, D. Petrov, and R. A. Rica, "Adiabatic processes realized with a trapped brownian particle", Phys. Rev. Lett. **114**, 120601 (2015) (cit. on pp. 15, 16, 82).

[55]V. Blickle and C. Bechinger, "Realization of a micrometre-sized stochastic heat engine", Nat Phys **8**, 143–146 (2012) (cit. on pp. 15, 16).

[56]I. A. Martinez, E. Roldan, L. Dinis, D. Petrov, J. M. R. Parrondo, and R. A. Rica, "Brownian carnot engine", Nat Phys **12**, 67–70 (2016) (cit. on p. 15).

[57]I. A. Martnez, É. Roldán, L. Dinis, D. Petrov, and R. A. Rica, "Adiabatic processes realized with a trapped brownian particle", Phys. Rev. Lett. **114**, 120601 (2015) (cit. on p. 15).

[58]R. Landauer, "Irreversibility and heat generation in the computing process", IBM Journal of Research and Development **5**, 183–191 (1961) (cit. on p. 16).

[59]R. Almog, S. Zaitsev, O. Shtempluck, and E. Buks, "Signal amplification in a nanomechanical duffing resonator via stochastic resonance", Applied Physics Letters **90**, 013508 (2007) http://dx.doi.org/10.1063/1.2430689 (cit. on p. 20).

[60]F. Mueller, S. Heugel, and L. J. Wang, "Optomechanical stochastic resonance in a macroscopic torsion oscillator", Phys. Rev. A **79**, 031804 (2009) (cit. on pp. 21, 82).

[61]K. Berg-Sørensen and H. Flyvbjerg, Rev. Sci. Instrum. **75** (2004) (cit. on pp. 26, 41, 46).

[62]A. Pralle, M. Prummer, E.-L. Florin, E. Stelzer, and J. Hörber, "Three-dimensional high-resolution particle tracking for optical tweezers by forward scattered light", Microscopy Research and Technique **44**, 378–386 (1999) (cit. on p. 27).

[63]Y.-H. Hsu and A. Pralle, "Note: three-dimensional linearization of optical trap position detection for precise high speed diffusion measurements", Review of Scientific Instruments **85**, 076104 (2014) http://dx.doi.org/10.1063/1.4890384 (cit. on p. 27).

[64]A. Buosciolo, G. Pesce, and A. Sasso, "New calibration method for position detector for simultaneous measurements of force constants and local viscosity in optical tweezers", Optics Communications **230**, 357–368 (2004) (cit. on p. 29).

[65]S. F. Toli-Nørrelykke, E. Schäffer, J. Howard, F. S. Pavone, F. Jülicher, and H. Flyvbjerg, "Calibration of optical tweezers with positional detection in the back focal plane", Review of Scientific Instruments **77**, 103101 (2006) http://dx.doi.org/10.1063/1.2356852 (cit. on pp. 29, 133).

[66]J.-H. Baek, S.-U. Hwang, and Y.-G. Lee, "Trap stiffness in optical tweezers", Mirror **685**, 1100nm (2007) (cit. on p. 29).

[67]Y. Harada and T. Asakura, Opt. Commun. **124** (1996) (cit. on pp. 35, 40).

[68]K. J. Knox, D. R. Burnham, L. I. McCann, S. L. Murphy, D. McGloin, and J. P. Reid, "Observation of bistability of trapping position in aerosol optical tweezers", J. Opt. Soc. Am. B **27**, 582–591 (2010) (cit. on p. 36).

[69]P. Hänggi, P. Talkner, and M. Borkovec, "Reaction-rate theory: fifty years after kramers", Rev. Mod. Phys. **62**, 251–341 (1990) (cit. on pp. 37, 53).

[70]N. van Kampen, *Stochastic processes in physics and chemistry*, 3rd Ed (Elsevier, Amsterdam, 2007) (cit. on p. 41).

[71]R. S. Dutra, N. B. Viana, P. A. Maia Neto, and H. M. Nussenzveig, "Absolute calibration of forces in optical tweezers", Phys. Rev. A **90**, 013825 (2014) (cit. on p. 42).

[72]N. B. Viana, M. S. Rocha, O. N. Mesquita, A. Mazolli, P. A. Maia Neto, and H. M. Nussenzveig, "Towards absolute calibration of optical tweezers", Phys. Rev. E **75**, 021914 (2007) (cit. on p. 42).

[73]W. Denk and W. Webb, Appl. Opt. **29** (1990) (cit. on p. 46).

[74]C. W. Skingle, K. Heron, and D. R. Gaukroger, *The application of the hilbert transform to system response analysis* (HM Stationery Office, 1977) (cit. on p. 52).

[75]M. Rosenblum and J. Kurths, "Analysing synchronization phenomena from bivariate data by means of the hilbert transform", in *Nonlinear analysis of physiological data* (Springer, 1998), pp. 91–99 (cit. on p. 52).

[76]E. Guyon, J. Hulin, and L. Petit, *Hydrodynamique physique*, Savoirs actuels (EDP Sciences, 2001) (cit. on p. 58).

[77]D. S. Grebenkov, "First exit times of harmonically trapped particles: a didactic review", Journal of Physics A: Mathematical and Theoretical **48**, 013001 (2015) (cit. on pp. 61, 63, 91).

[78]M. Brunner, J. Dobnikar, H.-H. von Grünberg, and C. Bechinger, "Direct measurement of three-body interactions amongst charged colloids", Phys. Rev. Lett. **92**, 078301 (2004) (cit. on p. 68).

[79]K. Sekimoto, Prog. Theor. Phys. Suppl. **130** (1998) (cit. on p. 73).

[80]V. Blickle and C. Bechinger, Nat. Phys. **8** (2012) (cit. on p. 73).

[81]J. Taylor, *An introduction to error analysis* (University Science Books, 1996) (cit. on pp. 75, 114).

[82]Reynaud, S., "Introduction à la réduction du bruit quantique", Ann. Phys. Fr. **15**, 63–162 (1990) (cit. on p. 91).

[83]D. W. Allan, "Statistics of atomic frequency standards", Proceedings of the IEEE **54**, 221–230 (1966) (cit. on p. 109).

[84]F. Czerwinski, A. C. Richardson, and L. B. Oddershede, "Quantifying noise in optical tweezers by allan variance", Opt. Express **17**, 13255–13269 (2009) (cit. on p. 109).

[85]L. Jauffred, S. M.-R. Taheri, R. Schmitt, H. Linke, and L. B. Oddershede, "Optical trapping of gold nanoparticles in air", Nano Letters **15**, 4713–4719 (2015) (cit. on p. 109).

[86]Y. Seol, D. L. Stein, and K. Visscher, "Phase measurements of barrier crossings in a periodically modulated double-well potential", Phys. Rev. Lett. **103**, 050601 (2009) (cit. on p. 118).

[87]K. Sasaki, M. Tsukima, and H. Masuhara, "Three-dimensional potential analysis of radiation pressure exerted on a single microparticle", Applied Physics Letters **71**, 37–39 (1997) (cit. on p. 123).

[88]M. Gu, P. C. Ke, and X. S. Gan, "Trapping force by a high numerical-aperture microscope objective obeying the sine condition", Review of Scientific Instruments **68**, 3666–3668 (1997) (cit. on p. 123).

[89]P. Wu, R. Huang, C. Tischer, A. Jonas, and E.-L. Florin, "Direct measurement of the nonconservative force field generated by optical tweezers", Phys. Rev. Lett. **103**, 108101 (2009) (cit. on p. 123).

[90]K. Lindfors, T. Kalkbrenner, P. Stoller, and V. Sandoghdar, "Detection and spectroscopy of gold nanoparticles using supercontinuum white light confocal microscopy", Phys. Rev. Lett. **93**, 037401 (2004) (cit. on pp. 124, 126).

[91]S. Spindler, J. Ehrig, K. König, T. Nowak, M. Piliarik, H. E. Stein, R. W. Taylor, E. Garanger, S. Lecommandoux, I. D. Alves, and V. Sandoghdar, "Visualization of lipids and proteins at high spatial and temporal resolution via interferometric scattering (iscat) microscopy", Journal of Physics D: Applied Physics **49**, 274002 (2016) (cit. on p. 124).

[92]J. Ortega-Arroyo and P. Kukura, "Interferometric scattering microscopy (iscat): new frontiers in ultrafast and ultrasensitive optical microscopy", Phys. Chem. Chem. Phys. **14**, 15625–15636 (2012) (cit. on p. 124).

[93]G. Jourdan, A. Lambrecht, F. Comin, and J. Chevrier, "Quantitative non-contact dynamic casimir force measurements", EPL (Europhysics Letters) **85**, 31001 (2009) (cit. on p. 127).

[94]K. Metwally, S. Mensah, and G. Baffou, "Fluence threshold for photothermal bubble generation using plasmonic nanoparticles", The Journal of Physical Chemistry C **119**, 28586–28596 (2015) (cit. on p. 128).

[95]W. M. Irvine, "Light scattering by spherical particles: radiation pressure, asymmetry factor, and extinction cross section", J. Opt. Soc. Am. **55**, 16–21 (1965) (cit. on p. 128).

[96]C. F. Bohren and D. Huffman, *Absorption and scattering of light by small particles*, Wiley science paperback series (Wiley, 1983) (cit. on p. 128).

[97]H. Hulst and H. van de Hulst, *Light scattering by small particles*, Dover Books on Physics (Dover Publications, 1957) (cit. on p. 128).

[98]L. Landau and E. Lifshitz, "Statistical physics, vol. 5", Course of theoretical physics **30** (1980) (cit. on p. 131).

[99]P. Welch, "The use of fast fourier transform for the estimation of power spectra: a method based on time averaging over short, modified periodograms", IEEE Transactions on Audio and Electroacoustics **15**, 70–73 (1967) (cit. on p. 132).

[100]K. M. McPeak, C. D. van Engers, M. Blome, J. H. Park, S. Burger, M. A. Gosálvez, A. Faridi, Y. R. Ries, A. Sahu, and D. J. Norris, "Complex chiral colloids and surfaces via high-index off-cut silicon", Nano Letters **14**, PMID: 24746023, 2934–2940 (2014) (cit. on pp. 139, 140).

[101]J. P. Riehl and F. S. Richardson, "Circularly polarized luminescence spectroscopy", Chemical Reviews **86**, 1–16 (1986) (cit. on p. 142).

[102]L. V. Poulikakos, P. Gutsche, K. M. McPeak, S. Burger, J. Niegemann, C. Hafner, and D. J. Norris, "The Optical Chirality Flux as a Useful Far-Field Probe of Chiral Near Fields", ArXiv e-prints (2016) (cit. on p. 142).

[103]R. Azzam, "Division-of-amplitude photopolarimeter (doap) for the simultaneous measurement of all four stokes parameters of light", Journal of Modern Optics **29**, 685–689 (1982) (cit. on p. 145).

[104]A. D. Martino, E. Garcia-Caurel, B. Laude, and B. Drévillon, "General methods for optimized design and calibration of mueller polarimeters", Thin Solid Films **455456**, The 3rd International Conference on Spectroscopic Ellipsometry, 112–119 (2004) (cit. on p. 145).

[105]P. Samori, *Scanning probe microscopies beyond imaging: manipulation of molecules and nanostructures* (Wiley-VCH, 2006) (cit. on p. 149).

[106]S. Boriskina and N. I. Zheludev, *Singular and chiral nanoplasmonics* (CRC Press, 2014) (cit. on p. 152).

[107]A. Canaguier-Durand, J. A. Hutchison, C. Genet, and T. W. Ebbesen, "Mechanical separation of chiral dipoles by chiral light", New Journal of Physics **15**, 123037 (2013) (cit. on p. 152).

[108]R. P. Cameron, S. M. Barnett, and A. M. Yao, "Discriminatory optical force for chiral molecules", New Journal of Physics **16**, 013020 (2014) (cit. on p. 152).

[109]K. Ding, J. Ng, L. Zhou, and C. T. Chan, "Realization of optical pulling forces using chirality", Phys. Rev. A **89**, 063825 (2014) (cit. on p. 152).

[110]G. Tkachenko and E. Brasselet, "Optofluidic sorting of material chirality by chiral light", Nat Commun **5** (2014) (cit. on p. 152).

[111] M. Galassi et al., *Gnu scientific library reference manual*, 3rd ed., Free Software Foundation () (cit. on p. 155).

[112] G. Volpe and G. Volpe, "Numerical simulation of brownian particles in optical force fields", in Spie nanoscience+ engineering (International Society for Optics and Photonics, 2013), 88102R–88102R (cit. on p. 157).

Gabriel SCHNOERING

On the Brownian dynamics of a particle in a bistable optical trap

Résumé

Cette thèse présente la réalisation d'un piège optique dans une configuration originale, le piston optique, où le contrôle sur la phase de l'interférence d'un faisceau incident avec sa réflexion sur un miroir permet de réaliser différents types d'expériences. Nous avons d'abord étudié les propriétés thermodynamiques d'une compression progressive du piston qui fait passer la dynamique de la particule piégée d'une région de stabilité vers une région de bistabilité mécanique. Dans le contexte de la résonance stochastique où une force extérieure périodique est appliquée sur cette dynamique bistable, une approche exploitant le facteur de Mandel ainsi qu'une analyse des délais entre les transitions d'états métastables se révèle efficace pour interpréter nos mesures dans différents régimes de forçage. Nous montrons également comment des nanoparticules métalliques peuvent être piégées aisément dans un tel piston optique et nous exploitons notre configuration pour mesurer de faibles effets de forces optiques. Enfin, nous piégeons des nano-objets chiraux uniques et nous montrons comment la configuration de notre piston permet de réaliser des expériences de reconnaissance chirale par polarimétrie différentielle.

Mots clés: bistabilité, pince optique, thermodynamique, résonance stochastique, synchronisation stochastique, mesure de forces faibles, chiralité.

Résumé en anglais

This thesis describes the experimental realization of an original optical trap, the optical piston, where controlling the phase of the interference of an incident beam with its reflection on a mirror allows achieving various experiments. We have first looked into the thermodynamics associated with a progressive compression of the piston leading the dynamics of a trapped particle from a region of stability to a region of mechanical bistability. In the context of stochastic resonance where a periodic external force is applied on this bistable dynamics, an approach exploiting the Mandel factor and a time-delay analysis on the hopping events between metastable states have proven efficient in interpreting the different results acquired in different regimes of drive. We have also shown how metallic nanoparticles can be trapped fairly easily in this kind of optical piston and we exploit our configuration to measure weak optical forces. Finally, we trap unique chiral nano-objects and we show how the configuration of our piston allows the realization of chiral recognition experiments by differential polarimetry.

Keywords: bistability, optical tweezer, thermodynamics, stochastic resonance, stochastic synchronization, high-resolution optical force measurments, chirality.